

Method Development for Coating of Nanosemiconductors with Graphitized Carbon using Flame Spray Pyrolysis Technology



Orestis Nikas

Masters in “Physics”

Supervisor: Professor Yiannis Deligiannakis

University of Ioannina

Department of Physics

June 2021

Ανάπτυξη Μεθοδολογίας για την Επικάλυψη Νανοημιαγωγών με Γραφιτικό Άνθρακα με Χρήση Τεχνολογίας Ψεκασμού Πυρόλυση



Ορέστης Νίκας

Δ.Μ.Σ Φυσικής με Ειδίκευση στην Πειραματική Φυσική
Επιβλέπων: Καθηγητής Ιωάννης Δεληγιαννάκης

Πανεπιστήμιο Ιωαννίνων
Σχολή Θετικών Επιστημών
Τμήμα Φυσικής
Ιούνιος 2021

Abstract

In the present Master Thesis, we have developed a method for the encapsulation of nanostructured semiconductors such as TiO_2 with graphitized carbon in one step process using Flame Spray Pyrolysis (FSP) technology. Carbon coating on the surface of TiO_2 has attracted attention due to the versatility and the properties of the core-shell material in photocatalysis and electron transfer.

Typically, coatings are achieved in multi-step wet phase procedures. Herein we have focused our effort on the development of *in situ* an one step procedure where the coating thickness and graphitization can be controlled by the FSP parameters set-up. Shell thickness and composition have to be carefully manipulated as defective or thick carbon shells can trammel the core particles efficiency in applications. The coating set-up enabled the production of carbon-coated suboxides and in some cases we detected clusters of novel TiO_2 phases known as Magnéli phases close to the surface. Post FSP carbothermal treatment under carbon-rich CH_4 atmospheres was performed to improve graphitization.

Crystal phase composition and nanoparticles size of the produced materials were evaluated by powder X-ray Diffraction (pXRD). Uv-Vis Diffuse Reflectance spectroscopy was used to determine the bandgap values and investigate the optical properties of the particles. The carbon morphology, the degree of graphitization as well as verification of the cluster formation was determined by Raman spectroscopy. Surface structure and pore analysis of the nanoparticles were examined by nitrogen adsorption analysis (BET). Finally, the electronic properties of the materials were investigated by means of Electron Paramagnetic Resonance Spectroscopy (EPR).

Among the key results are: [1] Development of one step carbon-coating method for TiO_2 and TiO_{2-x} with controllable shell thickness and phase composition, using FSP. [2] Controlled graphitization of the carbon shell with post FSP treatment. [3] Identification of Magnéli phase clusters as part of the reductive particle formation process. [4] Preliminary evaluation of photocatalytic activity showed that the thin-coated materials are able to form stable electron-hole pairs and that the Magnéli phase clusters enhance charge transfer to the surface.

Περίληψη

Στο παρών Μεταπτυχιακό Δίπλωμα Ειδίκευσης, έγινε ανάπτυξη μεθόδου για την ενθυλάκωση νανοδομημένων ημιαγωγών όπως το TiO_2 με γραφίτοποιημένο άνθρακα σε διαδικασία ενός βήματος με την τεχνολογία Πυρόλυσης Ψεκασμού Φλόγας (FSP). Η εναπόθεση άνθρακα στην επιφάνεια του TiO_2 έχει προσελκύσει το ενδιαφέρον της επιστημονικής κοινότητας λόγω της ευελιξίας και των ιδιοτήτων των επικαλυμμένων σωματιδίων σε φωτοκαταλυτικές διεργασίες και σε διεργασίες μεταφοράς ηλεκτρονίων.

Ο συνήθης τρόπος για την ενθυλάκωση σωματιδίων περιλαμβάνει υγρές διεργασίες πολλών βημάτων. Επικεντρωθήκαμε στην ανάπτυξη μιας διεργασίας ενός βήματος στην οποία η επί τόπου ενθυλάκωση μπορεί να ελεγχθεί μέσω των παραμέτρων του FSP όσον αφορά το πάχος του κελύφους και της γραφίτοποίησης. Το πάχος του κελύφους αλλά και η σύσταση του πρέπει να ελέγχονται σχολαστικά καθώς είδη άνθρακα με ατέλειες ή παχιά κελύφη επηρεάζουν αρνητικά την απόδοση του βασικού σωματιδίου σε εφαρμογές. Η διάταξη για την ενθυλάκωση επιτρέπει την παρασκευή υποξειδίων επικαλυμμένα με άνθρακα καθώς και σε μερικές περιπτώσεις ανιχνεύσαμε πλειάδες από συγκεκριμένες υποξειδικές φάσεις των οξειδίων του TiO_2 γνωστές και ως φάσεις Magnéli κοντά στην επιφάνεια. Θερμικές κατεργασίες μετά το FSP κάτω από ατμόσφαιρες πλούσιες σε άνθρακα (CH_4) πραγματοποιήθηκαν για την βελτιστοποίηση της γραφίτοποίησης.

Η σύσταση των κρυσταλλικών φάσεων καθώς και το μέγεθος των νανοσωματιδίων υπολογίστηκαν μέσω της Περίθλασης Ακτίνων Χ σκόνης (pXRD). Η φασματοσκοπία Διάχυσης Ανάκλασης (UV-Vis DRS) χρησιμοποιήθηκε για τον υπολογισμό της ενέργειας χάσματος και την διερεύνηση των οπτικών ιδιοτήτων των σωματιδίων. Η μορφολογία του άνθρακα, ο βαθμός γραφίτοποίησης καθώς και η επιβεβαίωση της δημιουργίας των πλειάδων πραγματοποιήθηκαν μέσω της φασματοσκοπίας Raman. Η επιφανειακή δομή καθώς και η ανάλυση των πόρων πραγματοποιήθηκε μέσω της ανάλυσης προσρόφησης αζώτου (BET). Τέλος, οι ηλεκτρονικές ιδιότητες των σωματιδίων μελετήθηκαν μέσω της φασματοσκοπίας Ηλεκτρονικού Παραμαγνητικού Συντονισμού (EPR).

Τα πιο σημαντικά είναι: [1] Ανάπτυξη μεθόδου ενός βήματος ενθυλάκωσης με άνθρακα οξειδίων και υποξειδίων του TiO_2 με ελεγχόμενο πάχος κελύφους και φάσεων, μέσω FSP. [2] Ελεγχόμενη γραφίτοποίηση του ανθρακικού κελύφους μέσω μετα FSP θερμικής κατεργασίας. [3] Προκαταρκτική αξιολόγηση της φωτοκαταλυτικής ενεργότητας έδειξε ότι τα σωματίδια με λεπτό κέλυφος μπορούν να παράγουν φωτοεπαγόμενα ζεύγη οπών-ηλεκτρονίων, και ότι τα εμπεριέχοντα τις πλειάδες των φάσεων Magnéli ενισχύουν την μεταφορά των φορτίων στην επιφάνεια.

Acknowledgments

This Master Thesis become a reality with the kind support and help of many individuals. I would like to express my sincere appreciation to all of them.

First and foremost, I would like to express my sincere gratitude to my supervisor, Professor Yiannis Deligiannakis, Head of the Lab of Physical Chemistry of Materials and Environment for his trust, deep knowledge, meaningful assistance. His constant guidance and advice helped me to complete the present thesis.

Besides my supervisor, I would like to especially thank PhD candidate Constantinos Moularas for his contribution in this thesis for imparting the knowledge about the FSP process, for the endless conversations, keen interest and support throughout the course of this thesis.

I am extremely thankful to all the members of our lab group starting from Dr. Panagiota Stathi for her helpful advice, Dr. Maria Solakidou for creating a friendly working environment, PhD candidate Pavlos Psathas for the cooperation and sharing his expertise and especially PhD candidate Areti-Konstantina Zindou for having the patience to teach me everything about EPR spectroscopy and support and postgraduate colleague Loukas Belles for his help and understanding.

I would also like to thank my ex-postgraduate colleagues now PhD candidates Christos Dimitriou and Asterios Mantzanis for creating a friendly working environment, the support, and the useful conversations we had throughout the course of this thesis.

I would also like to thank Dr. Yiannis Georgiou for his deep knowledge and suggestions at the early steps of this thesis and PhD candidate Panagiotis Ziogas for his tireless motivation.

Many thanks to the members of the Lab of Biomimetic Catalysis and Hybrid Materials and especially PhD candidate Marinos Theodorakopoulos for the disambiguation of chemistry topics.

I profusely thank the two members of my M.Sc. committee, Associate Professor Athanasios Bourlinos for the discussions and the cooperation and Associate Professor Alexios Douvalis for his warm welcoming in his laboratory.

I am extremely thankful to all my friends for their deep understanding, support and friendship all the time.

Last but not least, I would like to thank my family for all the support and faith they had put on me. My father Vyronas, for his constant encouragement, my mother Theodora for always showing me the right path and my sister Nefeli who is always there for me.

Table of Contents

Chapter 1 - Introduction.....	1
1.1 - Nanomaterials.....	1
1.2 - Titanium Dioxide (TiO ₂) As a Nanomaterial.....	2
1.3 - Properties of TiO ₂ Nanomaterials	4
1.3.1 - Crystal Structure of TiO ₂	4
1.3.2 - Electronic and Optical Properties of TiO ₂	7
1.4 - Modifications of TiO ₂ Nanomaterials	10
1.4.1 - Carbon-Coated TiO _{2-x} Nanomaterials.....	11
1.4.2 - Magnéli-Phase Ti _n O _{2n-1} Nanomaterials	15
1.5 - TiO ₂ As a Photocatalyst	19
1.6 – Nanomaterial Synthesis.....	23
1.6.1 – Wet Chemical Synthesis.....	23
1.6.2 – Flame Spray Pyrolysis (FSP).....	24
1.7 – M.Sc. Thesis Scope.....	27
Chapter 2 – Experimental Methods	28
2.1 - X-Ray Diffraction.....	28
2.1.1 - XRD Basic Principles.....	28
2.1.2 Calculation of Nanocrystal Size – Scherrer Equation	30
2.1.3 - XRD Experimental Set-Up (Dept. of Physics UOI)	31
2.2 - Raman Spectroscopy	32
2.2.1 - Raman Spectroscopy Basic Principles	32
2.2.2 - Raman Measurement Set-Up	34
2.2.3 - Raman Experimental Set-Up (Dept. of Physics UOI).....	36
2.3 - Uv-Vis Diffuse Reflectance Spectroscopy (DRS)	37
2.3.1 - DRS Basic Principles.....	37
2.3.2 - Tauc Plot – Determination of Band Gap	39
2.3.3 - DRS Experimental Set Up (Dept. of Physics UOI)	42
2.4 - Electron Paramagnetic Resonance Spectroscopy (EPR).....	43

2.4.1 - EPR Basic Principles.....	43
2.4.2 - Spin Trapping in EPR.....	47
2.4.3 - EPR Experimental Set-Up (Dept. of Physics UOI).....	48
2.5 - Furnace for Calcination (Dept. of Physics UOI).....	50
2.6 – X-Ray Photoelectron Spectroscopy (XPS)	51
2.6.1 – XPS Basic Principles.....	51
2.6.2 – XPS Experimental Set – Up (Dept. of Physics UOI).....	53
2.7 – Brunauer – Emmett – Teller (BET) Analysis	54
2.7.1 – BET Basic Principles	54
2.7.2 – BET Experimental Set – Up (Dept. of Physics UOI)	56
2.8 Flame Spray Pyrolysis (FSP)	57
2.8.1 Basic Principles of FSP.....	57
2.8.2 Particle Formation Process.....	58
2.8.3 Oxygen-lean (Anoxic) Flame Spray Pyrolysis.....	59
2.8.4 Coating in Flame Spray Pyrolysis.....	61
2.8.5 FSP Experimental Set-Up (Dept. Of Physics UOI).....	62
Chapter 3 – Results - Discussion.....	66
3.1 – Nanoparticle Synthesis.....	66
3.2 – Crystal Structure	71
3.2.1 – XRD Pattern and Crystal Size.....	71
3.2.2 – Surface Structure and Pore Analysis	75
3.3 – Uv-Vis Diffuse Reflectance Spectroscopy (DRS) Results.....	77
3.4 – Raman Spectroscopy Results.....	83
3.5 – Comparison of XRD, DRS and Raman Results	90
3.6 – Electron Paramagnetic Resonance (EPR) Results.....	92
3.6.1 – EPR Analysis of Pristine and Calcined Materials.....	92
3.6.2 – Photoinduced Radical Monitoring.....	102
Chapter 4 - Conclusions.....	112
References.....	114

Chapter 1

Introduction

1.1 - Nanomaterials

The term “nanomaterials” is employed to describe the creation and exploitation of materials with at least one dimension in the size range of 1-100 nm¹. Since Richard Feynman’s infamous prophetic lecture “There’s Plenty of Room at the Bottom” in 1959, it took more than two decades for the beginning of the new era of nanotechnology. Bulk materials have been discovered since antiquity and have been thoroughly investigated and as a result their properties have been adequately understood. Nanomaterials are of interest because at this scale, unique optical, mechanical, thermal, structural, electronic and magnetic properties emerge. These emergent properties are the result of two main factors. The first would be quantum confinement. The physical and chemical properties of a material are determined by the type of motion its electrons are allowed to execute². Since the latter is determined by the space in which the electrons are confined, it is obvious that reduction of the material’s dimensions to the nanoscale range, results in lesser space for the charge carriers to move and thus altering quantities like density of states and bandgap. The spatial constraint is directly connected with energy levels of a material. In semiconductors, the energy of the lowest excited state is inversely proportional to the size; the smaller the size the higher the energy. The second factor would be the surface-to-volume ratio. As we downsize, the atoms at the surface begin to become quantitatively comparable to those in the bulk material, increasing the surface area. This means that in the nanoscale regime, surface plays a much more active role in both physical and chemical processes. Consequently, quantum confinement and surface-to-volume ratio are responsible for the new properties not possessed either by macroscopic material or by the individual entity of each bulk material.

1.1 – Nanomaterials

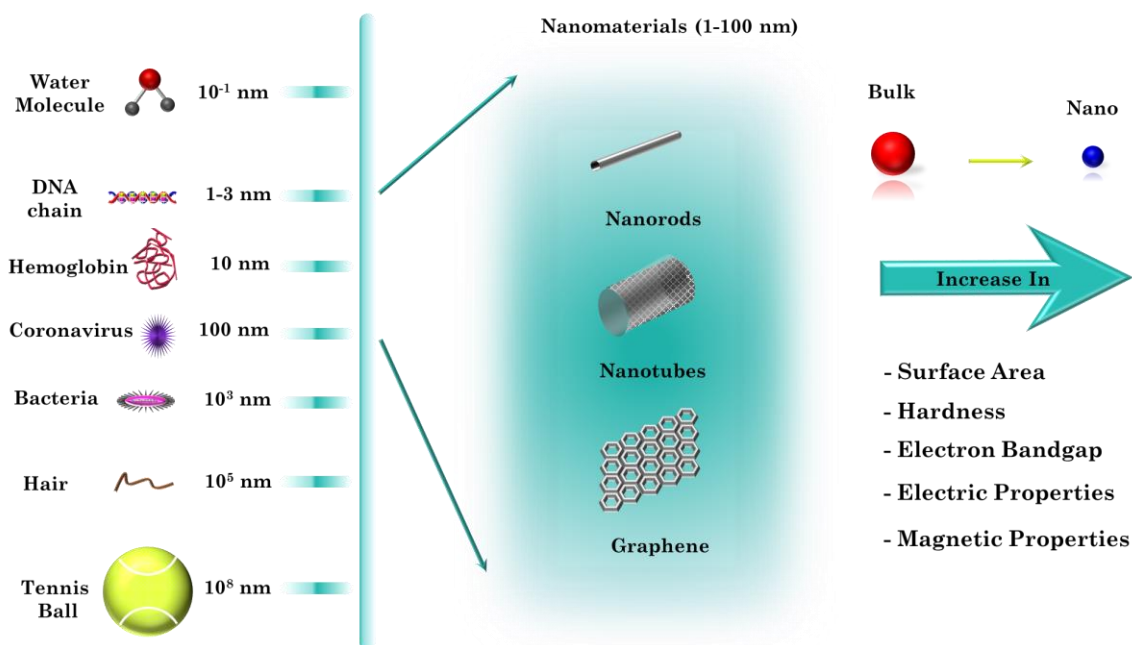


Figure 1.1. Comparison between bulk and nano materials.

The transition from bulk to the nano-scale regime is particularly impressive in the case of semiconductors. The reduction of size in semiconductors gives rise to dramatic improvements especially in optical and electronic properties. It has been shown that³ nanocrystal optical properties are size dependent, since there is a systematic blue shift of the band gap with reducing size⁴. Due to the different characteristics nano-semiconductors exhibit compared to their bulk counterparts, most of the research work is being concentrated towards nano-semiconductors in the recent decades.

1.2 - Titanium Dioxide (TiO_2) As a Nanomaterial

Nanoscale titanium dioxide (TiO_2) is one of the most investigated nano-semiconductors in the last decades. Known for its ultra-white color, non-toxicity, high refractive index and UV resistant properties (it can both scatter and absorb UV rays), it serves as the best candidate in many areas of research. From industrial pigments since the 1940s and later as ultraviolet (UV) absorber in sunscreens, TiO_2 nanoparticles are used today in plethora of applications ranging from solar cells⁵, photocatalysis^{6,7}, gas sensors⁸ to superhydrophilic surfaces⁹. These applications can be roughly divided into “energy” and “environmental” categories.

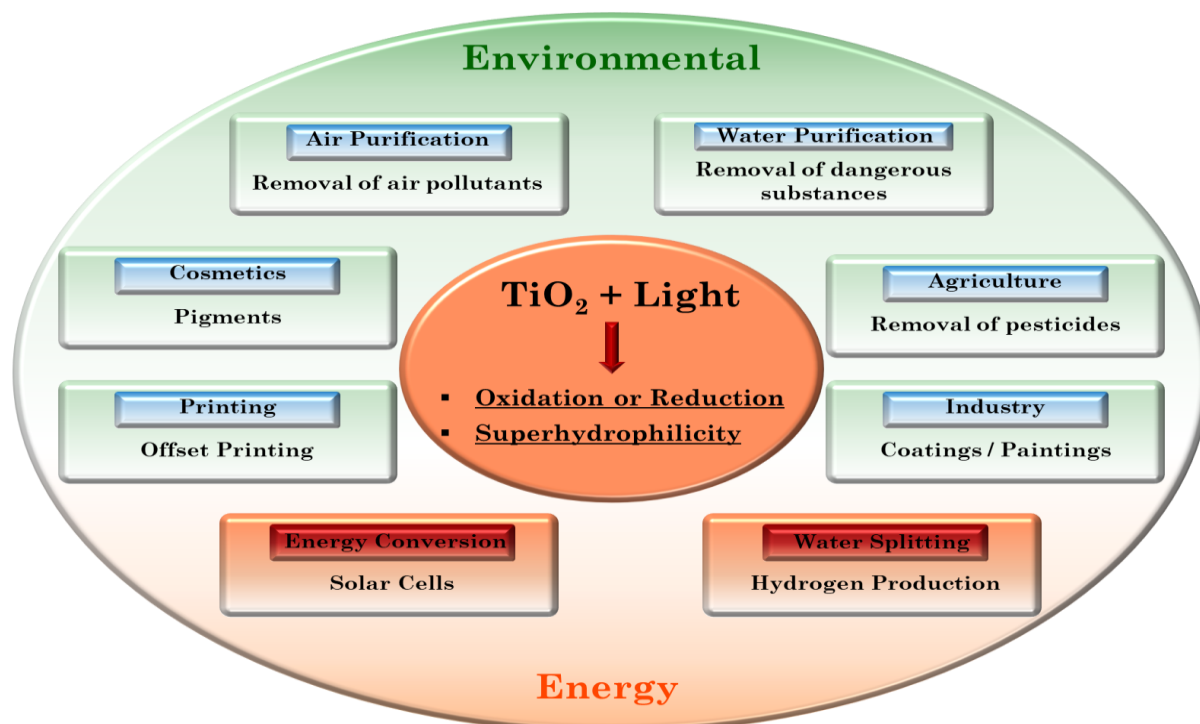


Figure 1.2. Applications of TiO₂ in industrial scale

The annual nano titanium dioxide market is valued at over 15 billion \$ per year with increasing rates over the next few years. Except from the big market share, the new properties with great perspectives in applications of TiO₂ lead to a rise of related publications in scientific journals, as shown in Fig. 1.4. It is common sense that TiO₂ as a material excels both scientifically and industrially.

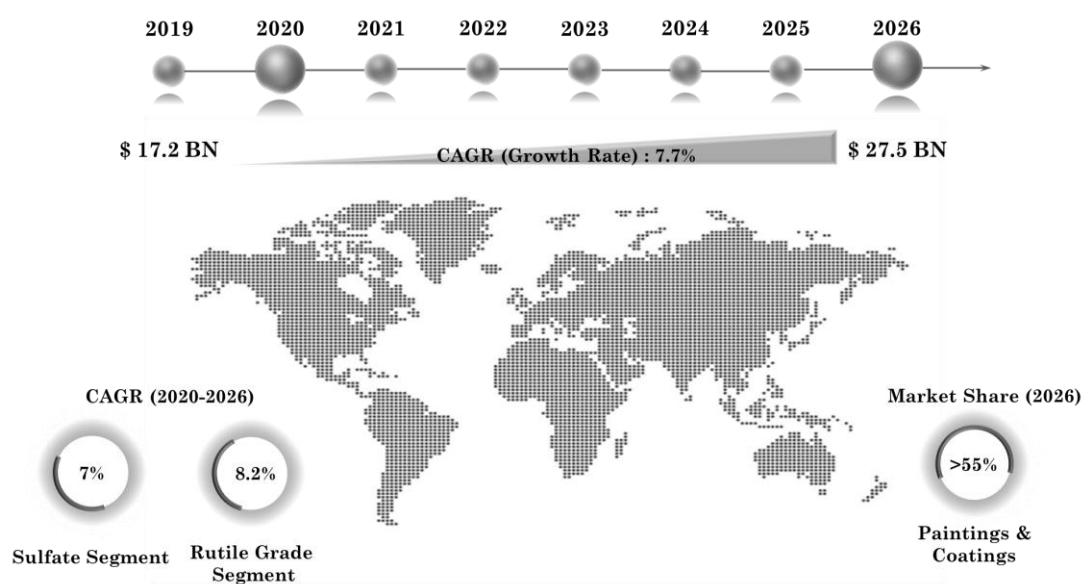


Figure 1.3. Growth of global nano TiO₂ market over the years © Global Market Insights.

1.3 - Properties of TiO₂ Nanomaterials

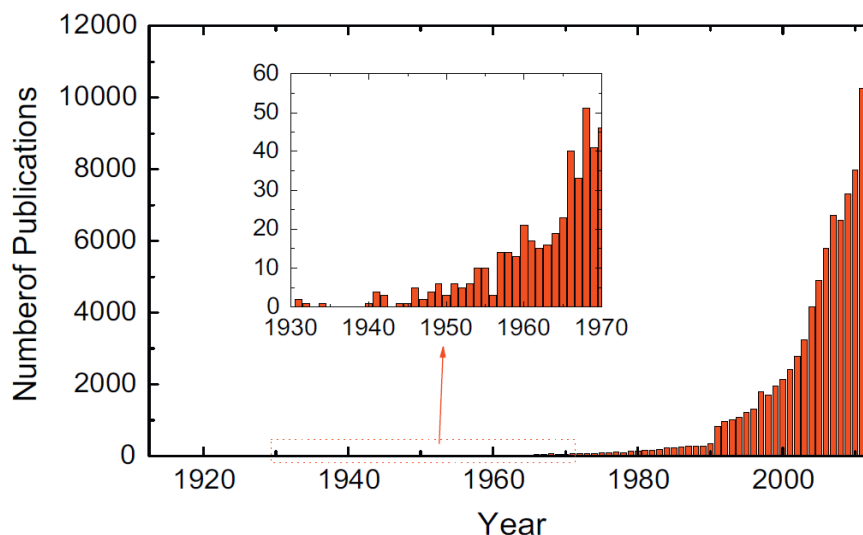


Figure 1.4. Number of research articles published from 1913 to 2013 using “TiO₂” as a keyword¹⁰.

The performance of TiO₂ in the aforementioned applications is greatly influenced by the size and crystal structure of the nanoparticles. The different polymorphic structures of TiO₂ exhibit unique physicochemical and electronic properties which will be analyzed below.

1.3 - Properties of TiO₂ Nanomaterials

1.3.1 - Crystal Structure of TiO₂

Titanium dioxide comes in three crystal phases: anatase, rutile and brookite. The most commonly encountered crystal phases are rutile and anatase. The basic geometric configuration in those structures is the octahedron. Both anatase and rutile structures are made of chains of TiO₆ octahedra where every titanium (Ti⁴⁺) ion is surrounded by an octahedron of six oxygen (O²⁻) ions.

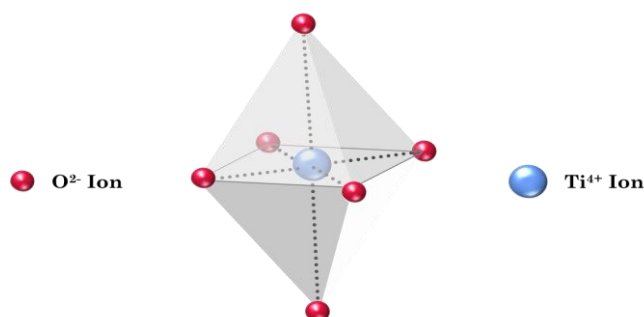


Figure 1.5. Schematic representation of TiO₆ octahedron

1.3.1 – Crystal Structure of TiO₂

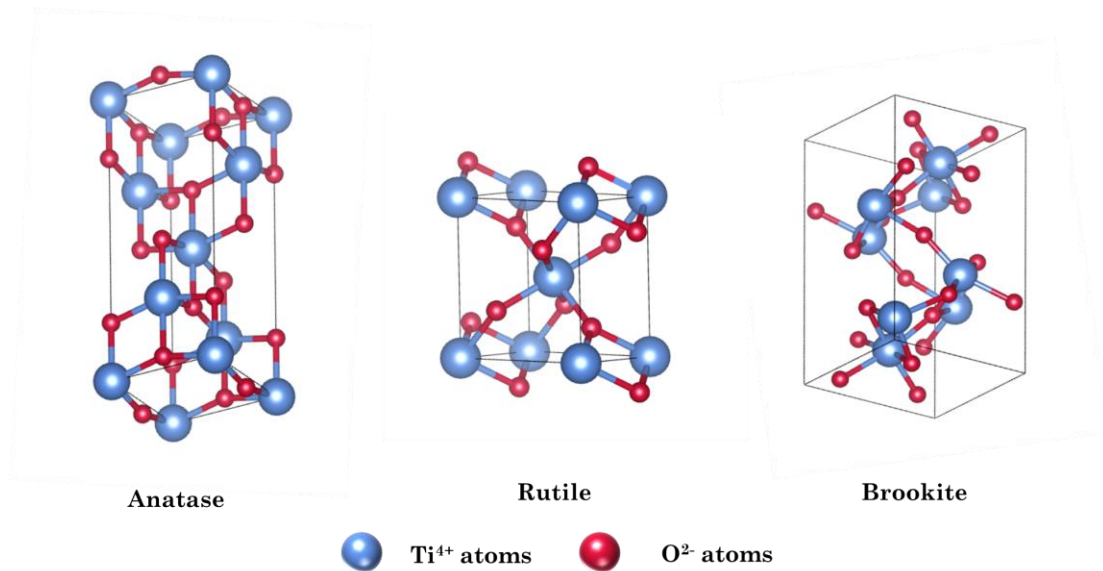


Figure 1.6. Anatase, Rutile and Brookite TiO₂ unit cells. Blue and red spheres represent Ti and O atoms respectively.

The structures are constructed based on the octahedron configuration. In order to construct the lattice, the octahedra are connected with different orientations along their atoms¹¹. The three orientations two octahedra can be connected are as follows: edge sharing, corner sharing and face sharing as shown in Fig. 1.7.

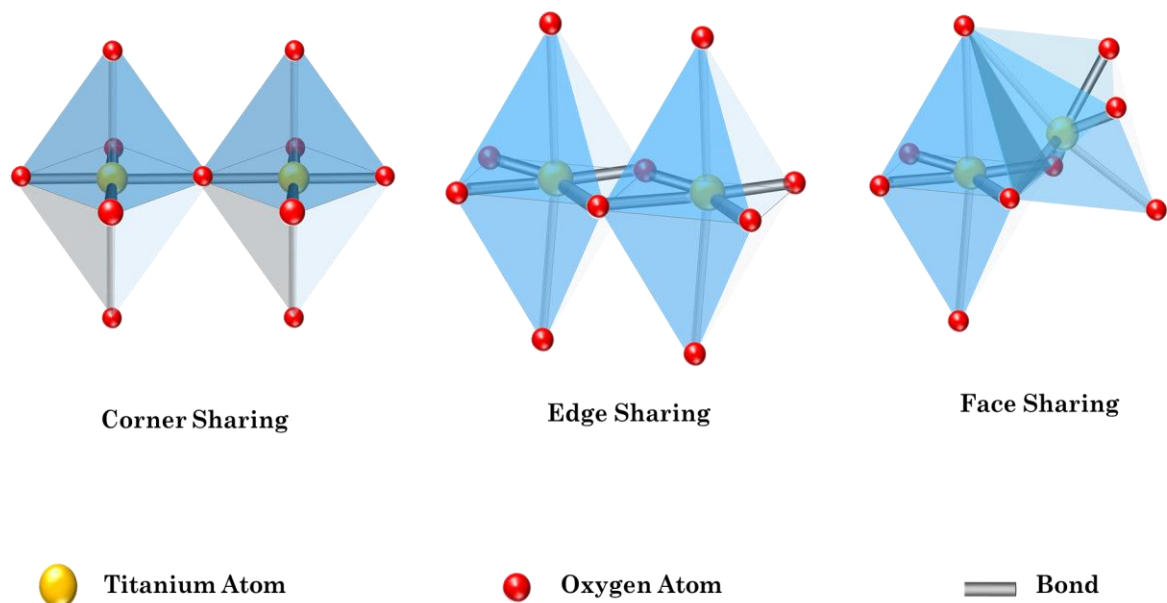


Figure 1.7. Corner sharing, Edge sharing and Face sharing octahedron configuration. The titanium and oxygen atoms are noted with yellow and red color respectively.

1.3.1– Crystal Structure of TiO₂

In the rutile structure, each octahedron is in contact with ten neighbors (two edge sharing oxygen pairs, and eight corner sharing oxygen atoms), while in the anatase structure, each octahedron is in contact with eight neighbors (four edge sharing and four corner sharing). The Ti-Ti distances in the anatase structure are larger whereas Ti-O distance is shorter than those of rutile¹². A more detailed look on the parameters is shown in Table 1.1.

Structure	Cell Parameters				Atom	Atom Position			Space Group
	a(Å)	b(Å)	c(Å)	β		X	Y	Z	
Anatase	3.784	3.784	9.1543	90°	Ti	0	0	0	I4 ₁ /amd
					O	0	0	0.2081	
Rutile	4.5922	4.5922	2.9574	90°	Ti	0	0	0	P4 ₂ /mnm
					O	0.3049	0.3049	0	

Table 1.1. Crystallographic and structural parameters of anatase and rutile¹³.

From a structural perspective, the difference between the two phases originates from the order of the TiO₆ octahedral units. In rutile the packing is linear whereas in anatase the packing comes in zig-zag. Linear packing has closest TiO₆ octahedral units together and that is the reason for the anatase less density by 9% compared to that of rutile. This also leads to a slightly different surface to volume ratio which can have a detrimental role in the nanomaterial's applications.

When it comes nano-TiO₂ synthesis, control over the different phases when simultaneous control over size is desirable, can be quite challenging. Thermodynamically, the relative stability of anatase and rutile is primary governed by the Gibbs free energy ($\Delta G = \Delta H - T\Delta S$) and more specifically by the competing contributions of bulk and surface energies. Rutile is the most thermodynamically stable phase for bulk TiO₂. However, below a certain particle size, surface energy dominates, leading to anatase particles being energetically more stable. The “crossover” size has been supported by experimental observations¹⁴ to be in the range of 7-22 nm. However, the precise critical size where each phase is thermodynamically more stable remains ambiguous.

The most important factor affecting the anatase-to-rutile transformation is widely perceived to be the amount and presence of oxygen vacancies. The anatase to rutile transformation is reconstructive, meaning that the transformation involves the breaking and reforming of bonds¹⁵. Oxygen vacancies therefore ease the rearrangement of titanium atoms. Furthermore, rutile is known to better accommodate a high concentration of oxygen defects compared to anatase¹⁶.

1.3.2 – Electronic and Optical Properties of TiO₂

Another thing to mention is the irreversible anatase to rutile transformation as a function of temperature. Despite the fact that a wide variation in rutilation temperature is reported ranging from 390°C¹⁷ to 900°C¹⁸, the general conclusion is that fine powders of high purity exhibit phase transformation at temperatures from ~600°C to 700°C.

1.3.2 - Electronic and Optical Properties of TiO₂

In order to gain an insight into the nature of TiO₂ nanomaterials, we need to examine TiO₂ from the electronic perspective. Theoretical calculations concerning the electronic structure are directly associated with the Density of States (DOS). DOS provides information about the material's band structure. A typical band structure diagram for the two polymorphs of anatase and rutile is shown in Fig. 1.8.

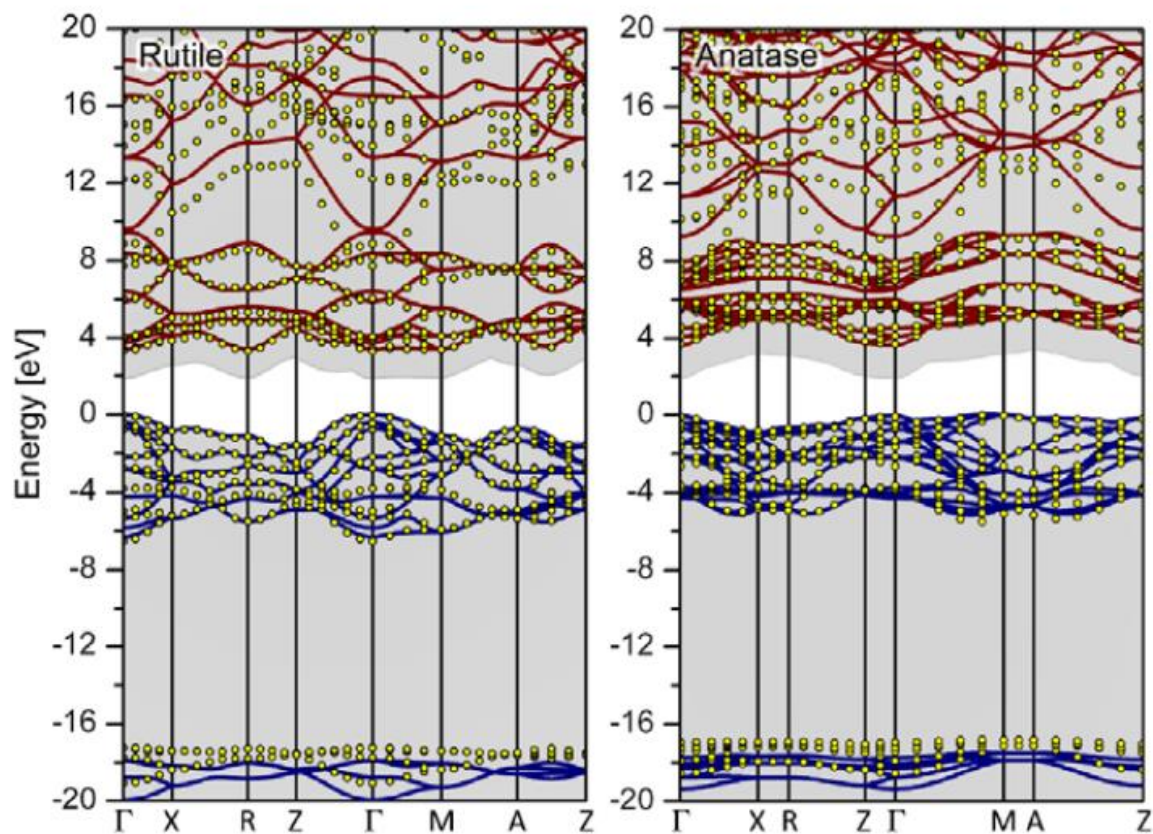


Figure 1.8. TiO₂ band structures for the rutile (left) and anatase (right) polymorphs. High symmetry points are noted on the horizontal axis. The gray shaded areas correspond to energies below the highest valence band and above the lowest conduction band¹⁹.

Band diagrams contain information regarding band transitions which are essential for the determination of the band gap value. Different methods can be used for the theoretical calculation of the band gap value. A few of them are summarized in Table 1.2.

1.3.2 – Electronic and Optical Properties of TiO₂

Method	Fundamental Bandgaps (eV)	
	Rutile	Anatase
DFT-PBE	1.88 ($\Gamma \rightarrow \Gamma$)	1.94 (0.88 $\Sigma \rightarrow \Gamma$)
DFT-HSE06	3.39 ($\Gamma \rightarrow \Gamma$)	3.60 (0.89 $\Sigma \rightarrow \Gamma$)
PBE-G ₀ W ₀	3.46 ($\Gamma \rightarrow \Gamma$)	3.73 ($\Sigma \rightarrow \Gamma$)
HSE06-G ₀ W ₀	3.73 ($\Gamma \rightarrow \Gamma$)	4.05 ($\Sigma \rightarrow \Gamma$)

Table 1.2. Calculated fundamental bandgaps (given in eV) of the TiO₂ polymorphs¹⁹.

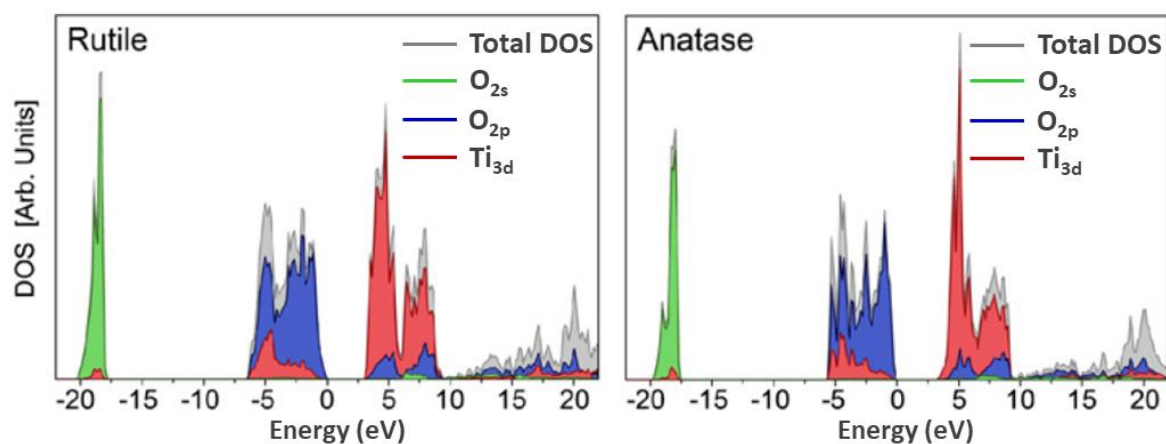


Figure 1.9. Total Density of States (DOS) for the two TiO₂ polymorphs rutile (left) and anatase (right). Shown are the Ti-3d, O-2s and O-2p contributions to the local density of states¹⁹.

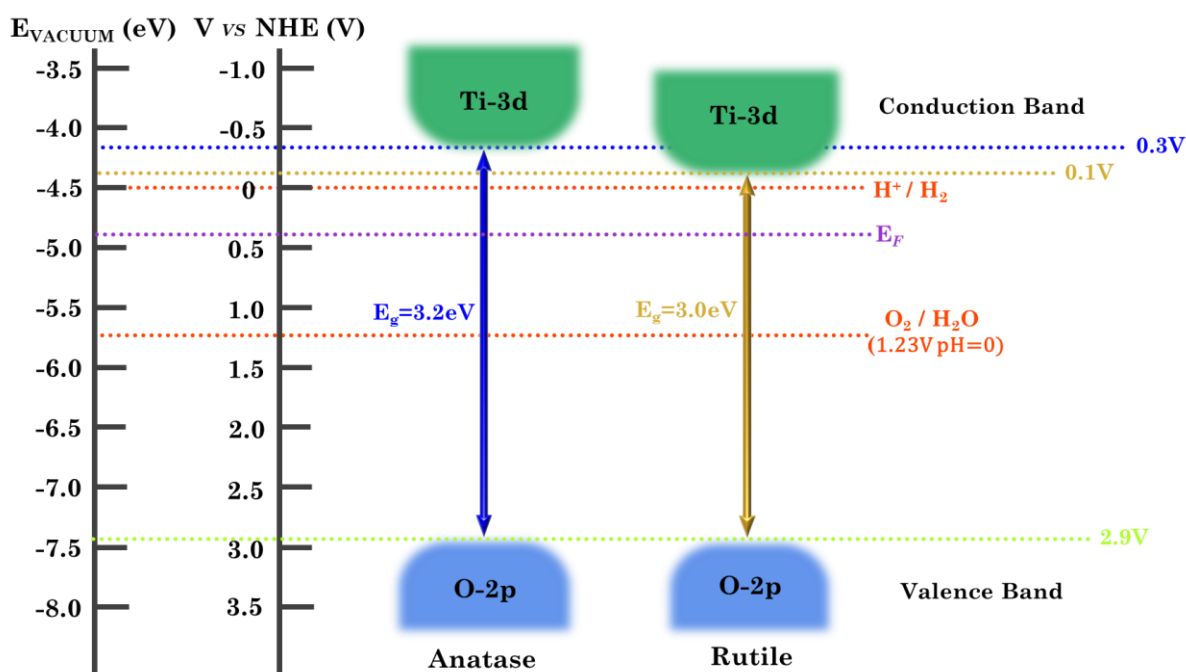


Figure 1.10. Energy scale diagram vs. Vacuum and vs. NHE of the two polymorphs.

1.3.2 – Electronic and Optical Properties of TiO₂

An analysis of the Density of States (DOS) depicted in Fig. 1.9 entails that the valance band is predominantly determined by the O-2p wave functions whereas the conduction band is determined by the Ti-3d wave functions for both crystal phases. If we take into consideration the energy level positioning vs. the Normal Hydrogen Electrode (NHE) we can have a better estimate about the positions of the valance and conduction band relatively to potentials for various photocatalytic applications. As shown in Fig. 1.10 both the polymorphs are within the range for the reduction of H⁺ to H₂ as well as the oxidation of H₂O to O₂²⁰.

It is apparent that from the DOS analysis as well as the energy scale diagram vs. the Vacuum and NHE, one can extract the band positioning as well as the bandgap value. Experimentally, the bandgap value is calculated using Diffuse Reflectance Spectroscopy. The main mechanism of light absorption in semiconductors like TiO₂ is interband electron transitions. From Fig. 1.8 one can see possible transitions between conduction and valance bands.

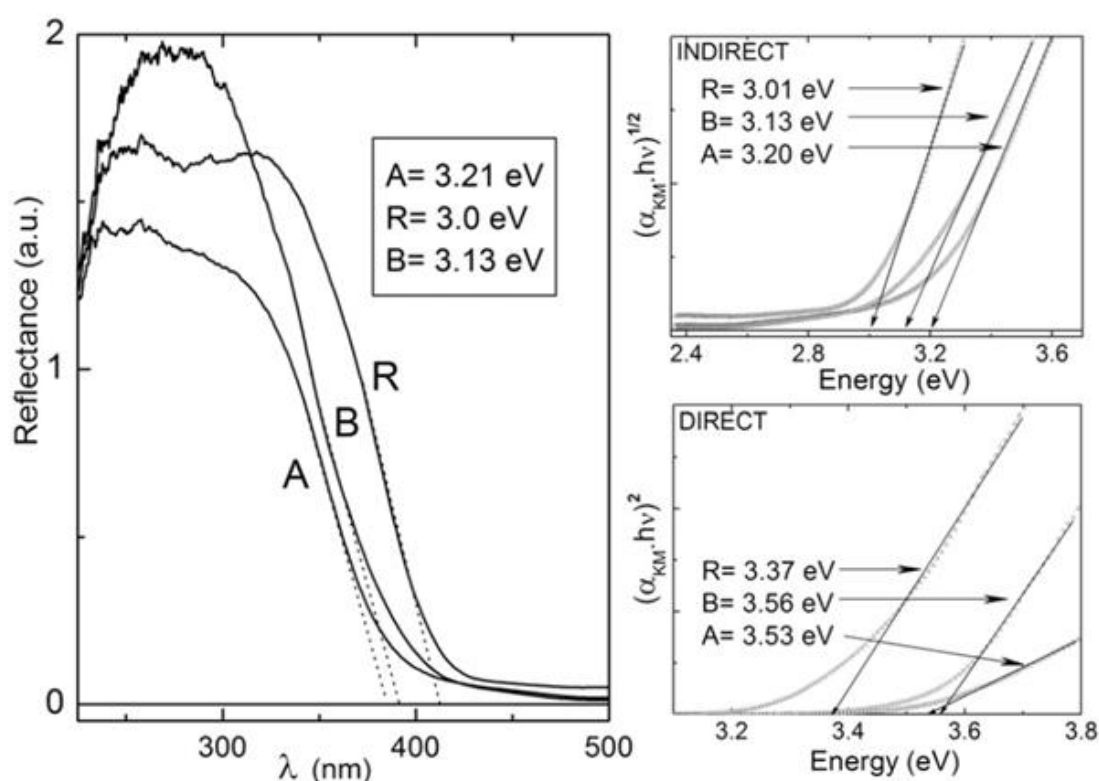


Figure 1.11. (Left) UV-Vis Diffuse Reflectance Spectrum of the 3 polymorphs anatase (A), rutile (R) and brookite (B) respectively. Tauc Plot with the Kubelka-Munk equivalent absorption coefficient for indirect (upper) and direct (lower) transitions²¹.

As we can see in Fig. 1.11 for the direct transition, the bandgap value for anatase and rutile are in good agreement with the theoretical values obtained from Density Functional Theory (DFT) calculations. For the indirect transition case, anatase possesses an energy

bandgap of 3.2 eV with an absorption edge at 386 nm which lies in the near UV range. Rutile has a narrower energy band gap of 3.01 eV with an absorption edge at 416 nm in the visible range. Both forms are photocatalytic which can be validated from Fig. 1.10 by comparing the band placement in relation with pertinent potentials in photocatalysis.

1.4 - Modifications of TiO₂ Nanomaterials

Many applications of TiO₂ nanomaterials are closely related to its optical properties. However, the highly efficient use of TiO₂ nanomaterials is sometimes tramméed by its wide band gap. Therefore, the desideratum is increasing their optical activity. The process of shifting the onset of the response from the UV to the visible region is usually done through band gap engineering. Band gap engineering can be done by tailoring the Density of States (DOS) of a material²². Two different strategies can be followed:

- ↪ **Doping:** metal (Al, Fe) or non-metal (C, N) atoms are introduced to the pristine crystal structure.
- ↪ **Oxygen Stoichiometry Engineering:** presence or absence of oxygen atoms, ranging from defects (oxygen vacancies) to novel phases (stoichiometric removal of oxygen) like Magnéli Phases in metal suboxides.

Another approach to achieve optimal efficiency in TiO₂ applications is through surface functionalization. As discussed earlier, at the nanoscale regime, surface plays an essential role in chemical and physical processes. Surface functionalization consists of two parts:

- ↪ **Attachment of ligands / functional groups at the surface:** Attachment of small molecules, compounds or functional groups to aid / support redox reactions.
- ↪ **Coating:** encapsulation of a core particle with an outer shell, serving as an active site for surface reactions, protection against oxidation or leaching of the core material.

Our interest is focused on both approaches and more specifically towards oxygen stoichiometry engineering for the formation of Magnéli Phases in TiO₂ suboxides (TiO_{2-x}) as well as surface functionalization via coating with the production of carbon-coated TiO₂ suboxides (TiO_{2-x}@C) in a core-shell formation. More details about each of the two approaches will be presented afterwards.

1.4.1 - Carbon-Coated TiO_{2-x} Nanomaterials

As one of the most abundant elements, carbon is one of the most studied materials in the scientific community. Its several different forms, such as graphite, diamond, fullerenes, carbon nanotubes (CNT) and graphene have attracted immense research interests owing to their excellent thermal, mechanical, optical and electrical properties and their great potential in various applications²³⁻²⁵. Since metal oxides are widely used in catalysis the joining of carbon and metal oxides could offer significant advantages in terms of their physical and chemical properties.

At the nanoscale regime, new properties originating from the nanoscale “effect” will make the joining of carbon and metal oxides much more interesting. Carbon-coating metal oxide nanoparticles could make for this efficient joining in a core-shell configuration²⁶. Given the diversity in surface modification of carbon nanomaterials, carbon-coated nanomaterials offer flexibility and versatility towards applications.

The fundamental building block of a graphite crystal is the graphene layer. Ideal graphene can be considered as a single-atom-thick sheet made of carbon atoms arranged in a hexagonal honeycomb lattice. Such an atomic structure is characterized by two types of C-C bonds (σ, π) constructed from the four valence orbitals ($2s, 2p_x, 2p_y, 2p_z$). Three σ -bonds join a C atom with its three neighbors. The C-C bonding is enhanced by the presence of a fourth bond associated with the overlap of p_z (π bond) orbitals²⁷. This unique structure endows graphene an extraordinary combination of physical and chemical properties such as its incomparable high electron mobility, mechanical strength and thermal conductivity²⁸.

Another important feature of graphene is its optical transparency. Due to its thinness a single graphene sheet is almost completely transparent with optical absorbance measured at just 2.3%. Graphene’s superior efficiency in the field of chemistry relies on its large surface area. Theoretical values of over 2500 m²/g have been reported²⁹, rendering graphene as one of the best candidates for surface reactions to take place.

Graphite consists of tridimensional (3D) stacking of graphene sheets with an interlayer spacing around 3.35 Å. Different kinds of graphite can be obtained depending on the stacking sequence of the carbon planes. As shown in Fig. 1.12, stacking leads to simple hexagonal graphite with a stacking sequence of AAA, Bernal graphite with an ABAB sequence and rhombohedral graphite with ABC ABC stacking sequence. It has been shown that³⁰ these graphene-based 3D crystals exhibit specific semi-metallic properties that depends directly on the geometry of the stacking between layers.

1.4.1 – Carbon-Coated TiO_{2-x} Nanomaterials

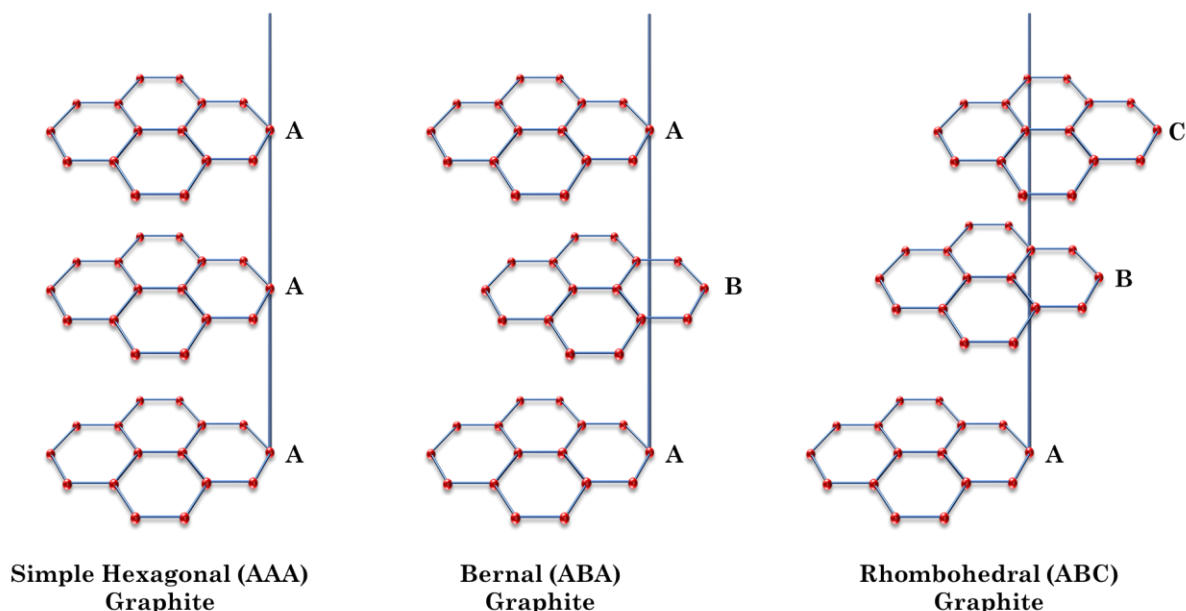


Figure 1.12. Atomic arrangement in Hexagonal (AAA), Bernal (ABA) and Rhombohedral (ABC) stacking of graphite. The vertical lines serve as visual lines to highlight the relative in-plane shifts between the layers.

The in-plane bonding in a single graphitic layer is covalent (σ -bonds) and therefore is strong. On the contrary, the interlayer bonding is done by a weak interlayer Van der Waals force. This allows the layers to slide across each other, making graphite a soft and malleable material. Since graphite has a planar structure, its electronic and thermal properties are highly anisotropic. The stronger in-plane atom bonding than that between neighboring layers, allows us to treat the behavior of the electrons in graphite as two dimensional, including the interaction between layers as a perturbation.

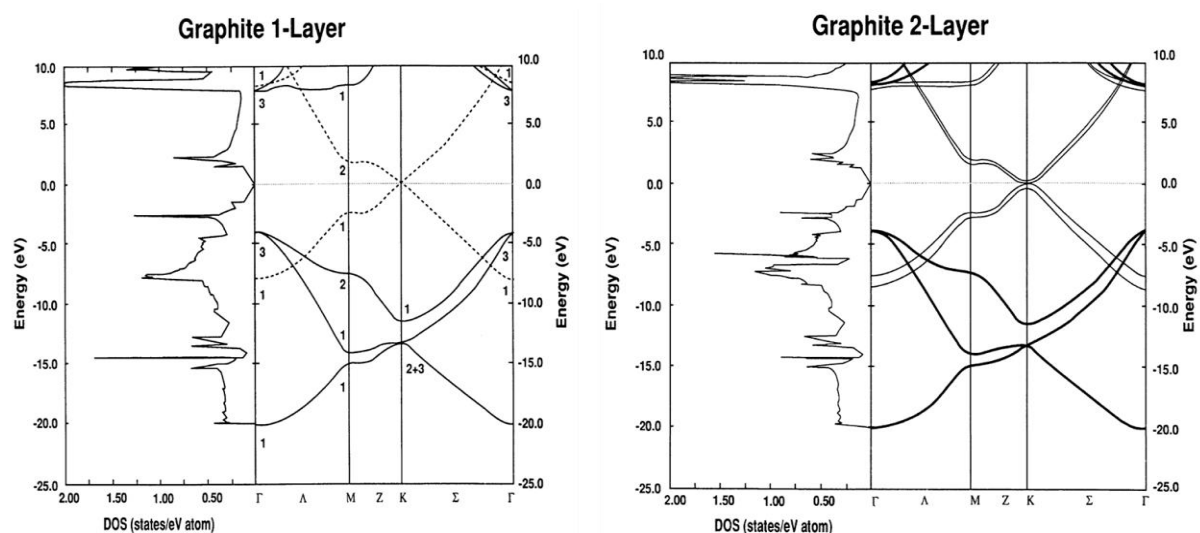


Figure 1.13. Kohn-Sham energy Bands and Density of States (DOS) for the graphite 1-layer (left) and 2-layer (right) respectively. Both are referred to E_F as zero of energy³¹.

1.4.1 – Carbon-Coated TiO_{2-x} Nanomaterials

Graphite exhibits unique electronic properties that have a strong correlation with multilayer stacking of graphene³². Fig. 1.13 refers to the band structure and Density of States (DOS) of one and two graphene layers respectively. One might notice that in the graphene case, the curve is linear around the *K* point where the bands touch each other rendering graphene as a zero-gap semiconductor. This is markedly changed when just one extra layer is bonded to the first one. In the two graphitic-layer case, the curve around the *K* point becomes parabolic. A more detailed investigation shows that there is a small overlap between valence and conduction bands as a result of interacting interlayer carbon atoms. Thus, graphite exhibits semi-metallic electronic properties. The band structure becomes increasingly complicated for 3 or more graphitic layers. The absence of interactions between interlayer atoms is the main reason that graphene has significantly different transport properties than systems consisting of more than two graphene layers. A reasonable question to answer would be the number of layers of graphene needed before the structure is regarded as 3D bulk graphite. It has been shown that 10 layers of graphene approach the 3D limit of graphite.

Core-shell nanomaterials constitute a special class of highly functional nanocomposite materials with tailored properties, which can be quite different than their single component counterparts either of the core or of the shell material. In the case of carbon coating TiO_{2-x} nanoparticles, one of the parameters that must be carefully manipulated is shell thickness.

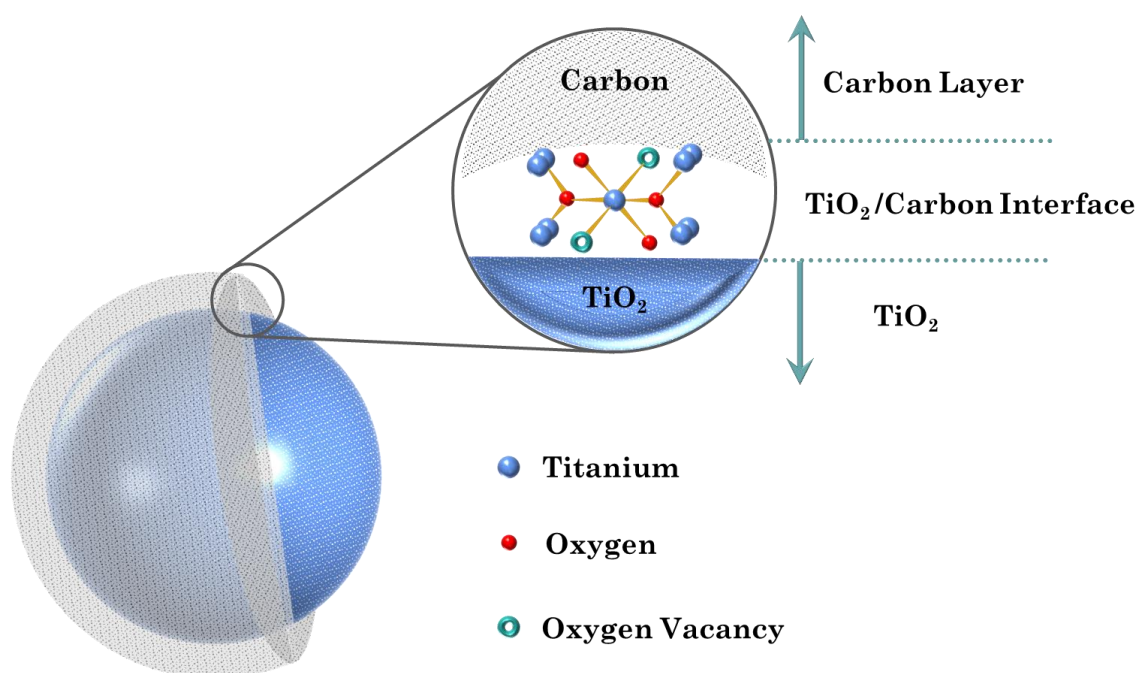


Figure 1.14. Schematic representation of carbon-coated TiO_{2-x} nanoparticles. An intermediate area of TiO₂-carbon interface is also noted.

1.4.1 – Carbon-Coated TiO_{2-x} Nanomaterials

Exploitation of both the core and the shell's photocatalytic properties requires the incident radiation being able to achieve charge separation in the core material without being absorbed earlier by the shell material. Optical absorbance of 2.3% per graphene sheet implies that up to 43 layers of graphene can be stacked for the minimum amount of radiation to reach the core particle and induce charge separation. With interlayer spacing measured at 3.35Å, this automatically translates to shell thickness no more than 14 nm. Core-shell nanocomposites with shell thickness more than 14 nm shield the absorption of light suppressing TiO₂ superb photocatalytic properties and therefore have limited photocatalytic applications.

Another thing to mention is the role of the carbon shell in relevance to the photocatalyst-carbon composite opto-electronic properties. Bandgap narrowing has been reported on C/TiO₂ composites³³ which can be attributed to carbon doping. Substantial carbon content tends to form a coating layer on the surface rather than migrating to the internal TiO₂ lattice. Nonetheless, it inevitably enters the surface lattice of TiO₂ occupying interstitial sites in the TiO₂ matrix, considering the smaller size of carbon. Carbon atoms entering the surface lattice leads to the introduction of mid-gap states thus narrowing the bandgap. This accounts for the visible response in photocatalytic applications of C/TiO₂ composites.

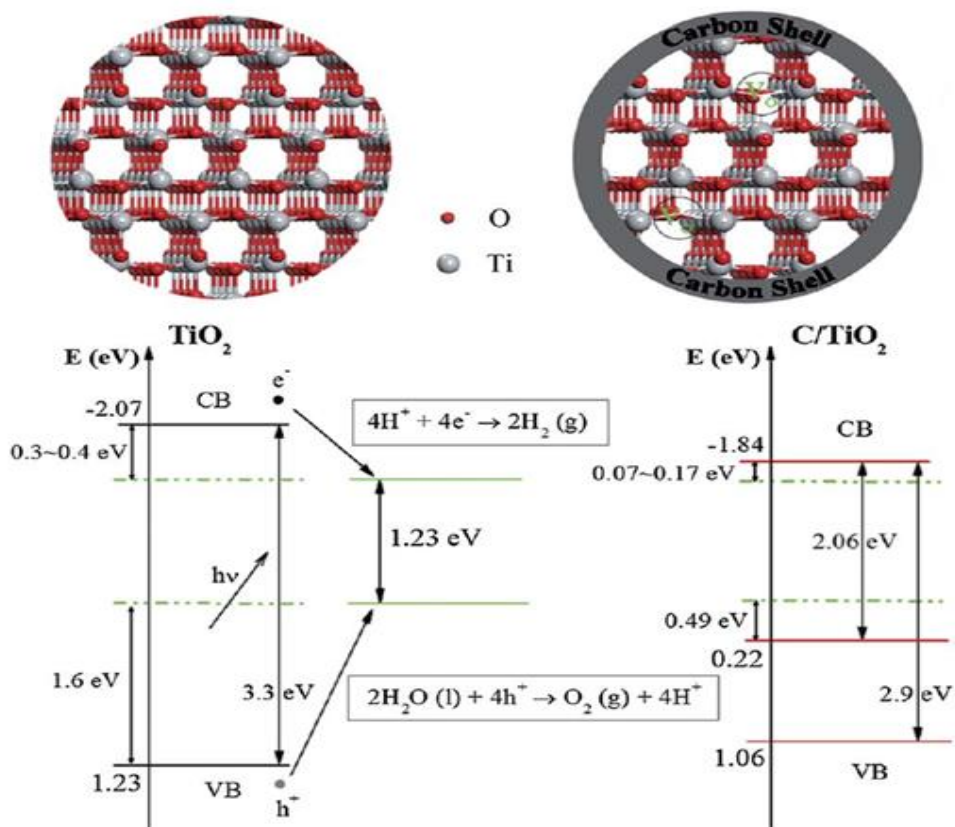


Figure 1.15. Schematic illustration of the nanocomposites and the calculated band positions for reference TiO₂ and C/TiO₂ respectively. Introduction of mid-gap states is accompanied by bandgap narrowing leading to visible response in photocatalysis³³.

Zhang *et al* studied the effect of carbon shell thickness on the photocatalytic degradation of various organic compounds, using a novel preparation method of $TiO_2@C$ nanocomposites³⁴. Liu *et al* examined the surface carbon species in carbon-coated $TiO_2@C$ photocatalysts and their different photocatalytic activity³⁵. Inagaki *et al* reported suppression of phase transformation to rutile and maintaining of photocatalytic activity for carbon-coated anatase particles³⁶.

1.4.2 - Magnéli-Phase $Ti_n O_{2n-1}$ Nanomaterials

All crystal structures ideally are characterized by a perfect periodicity of atomic arrays. Nonetheless, the absence or extra presence of atoms/ions from the lattice structure is very common in all types of crystalline materials. These imperfections are classified as defects. Among all the defects identified in crystalline materials, oxygen vacancies constitute the prevalent defect in many metal oxides³⁷.

Oxygen vacancies in metal oxides generate oxygen deficient metal oxides termed metal suboxides. Titanium suboxides have attracted considerable attention due their remarkable electronic and optical properties. In terms of their oxygen content, titanium suboxides can be classified in two families:

- ➔ **Oxygen Deficient Titanium suboxides TiO_{2-x}** : Stoichiometric point defects are present in the form of oxygen vacancies or titanium interstitials³⁸ ($0 < x < 0.001$).
- ➔ **Magnéli Phase Titanium suboxides TiO_{2-x}** : Presence of extended planar defects in the form of ordered oxygen deficient planes accompanied with changes in the crystal structure ($0.001 < x < 0.25$).

Since their discovery in the 1950s, Magnéli phase titanium suboxides, also noted as Ti_nO_{2n-1} (where n varies from 4 to 37), have several applications³⁹ in the fields of photocatalysis⁴⁰, fuel cells⁴¹, batteries⁴², charge storage⁴³ and environment⁴⁴.

Magnéli *et al*⁴⁵ studied oxides of transition metals by means of x-ray diffraction (XRD). They confirmed the existence of homologous compounds expressed by Ti_nO_{2n-1} and predicted that these structures could be all derived from the rutile structure as the mother structure. Wadsley proposed the structure principles termed as crystallographic shear structure describing how these compounds are derived from the mother structure⁴⁶. The new structure is introduced as follows:

- ⇒ The rutile structure is divided into blocks periodically parallel to a crystallographic plane called shear plane.
- ⇒ Blocks are translated relatively each other by a certain vector called shear vector.
- ⇒ The overlapping parts if generated, are removed.

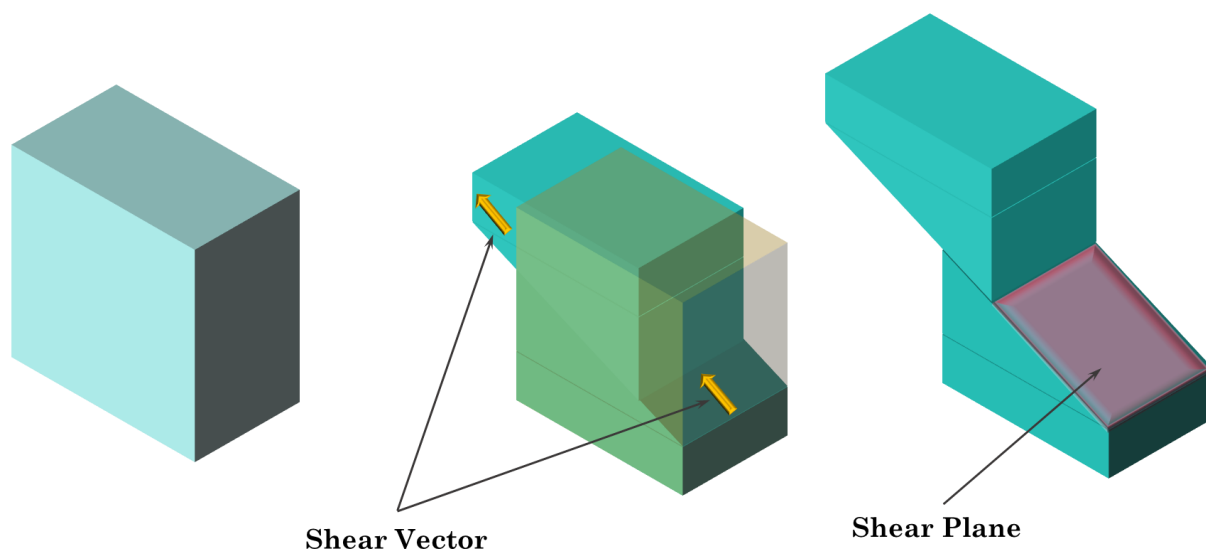


Figure 1.16. Schematic representation of the crystallographic shear operation. The shear plane and the shear vector are noted.

The crystallographic shear plane and shear vector for titanium oxides $\text{Ti}_n\text{O}_{2n-1}$ ($n=2, 3, \dots, 10$) were confirmed to be $(121)_{\text{rutile}}$ and $\frac{1}{2} [0\bar{1}1]_{\text{rutile}}$ respectively. The higher the n , the larger is the block of perfect rutile between two shear planes. The shear operation results in disturbance of the titanium arrangement, since the shear vector moves titanium ions in the octahedral configuration into the interstitial octahedral positions as shown in Fig. 1.17.

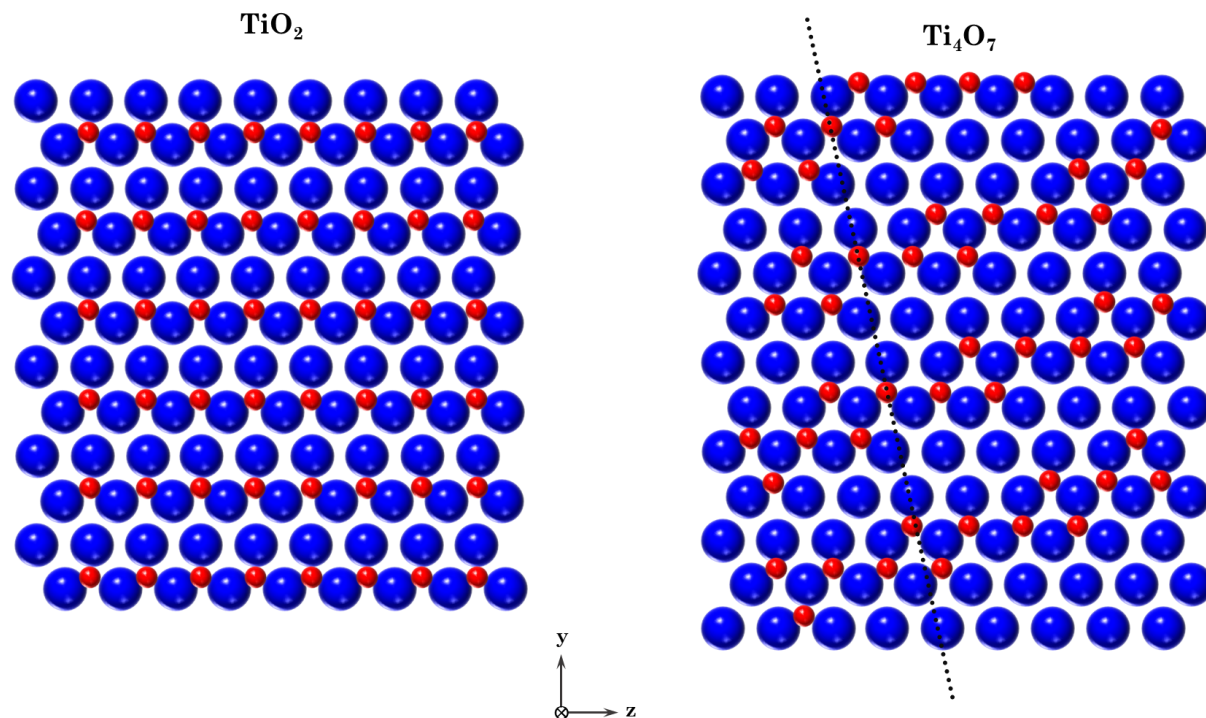


Figure 1.17. Left: A $[100]$ projection of an idealized titanium rutile structure. Right: A $[100]$ projection of the Ti_4O_7 Magnéli phase. Red circles are titanium and blue are oxygen atoms respectively. The dashed line indicates where the $(121)_{\text{rutile}}$ plane intersects this plane of atoms.

1.4.2 – Magnéli-Phase Ti_nO_{2n-1} Nanomaterials

The rutile structure is disrupted at regular finite intervals by discontinuities where octahedra share faces, and not just edges and corners as in the mother rutile structure. These rutile-like chains of n TiO_6 octahedra units are bounded by a corundum structure like Ti_2O_3 composed of face sharing octahedra. The oxygen deficiency occurs on the shear plane and homologous series of Magnéli phase titanium suboxides with various Ti/O ratios are formed depending on the spacing of the crystallographic shear plane. We therefore have infinite extension in two directions and a characteristic finite width (four TiO_6 octahedra for Ti_4O_7 , five for Ti_5O_9 and so on). Note that in contrast to Magnéli phases, Ti_3O_5 polymorphs whilst they satisfy the formula Ti_nO_{2n-1} , are rather a “neighboring” composition since they do not have crystallographic shear planes⁴⁷. Shear planes are intrinsic chemical defects in the sense that their presence changes the chemical composition and as such are only related indirectly to the purely physical dislocations present in practically all crystalline substances.

Crystallographic Structure	x-value in TiO_{2-x} formula	Defect Type
$TiO_{2-x} - TiO_2$	~ 0	Point defects Concentration of oxygen vacancies $x < 0.001$
$TiO_{1.999} - TiO_{2-x}$	0.001-0.0001 0.001- stoichiometric limit	Wadsley defects with different orientation and at different distances
$Ti_{37}O_{73} - TiO_{1.999}$ Magnéli phase	0.027 – 0.001	Shear planes oriented in [132] direction
$Ti_{16}O_{31} - Ti_{37}O_{73}$ Magnéli phase	0.0625 – 0.027	Shear planes oriented in [132] direction and additionally grouped in bands
$Ti_{10}O_{19} - Ti_{16}O_{31}$ Magnéli phase	0.1 – 0.0625	Orientation of shear planes changes from [132] direction to [121]
$Ti_4O_7 - Ti_{10}O_{19}$ Magnéli phase	0.25 – 0.1	Equidistance of distributed shear planes oriented in [121] direction
$Ti_3O_5 - Ti_4O_7$	0.33 – 0.25	Ti_2O_3 has corundum structure and Ti_3O_5 has no crystallographic shear planes, thus whilst they satisfy the Ti_nO_{2n-1} , they are not Magnéli phases.
$Ti_2O_3 - Ti_3O_5$	0.5 – 0.33	

Table 1.3. Structural transformation with increasing oxygen non-stoichiometry in TiO_{2-x} ⁴⁸.

1.4.2 – Magnéli-Phase $\text{Ti}_n\text{O}_{2n-1}$ Nanomaterials

The alteration in the description of the Magnéli phases as compared to regular oxygen deficient oxides is highlighted in Table 1.3. As we can see, the stoichiometric limit x within metal suboxides TiO_{2-x} can be described in terms of point defects cannot be higher than 0.001. Surpassing of this critical value leads to a new crystal structure described by extended planar oxygen defects.

The defective nature of the oxide has profound consequences on the properties Magnéli phase titanium suboxides demonstrate. It has been shown that the increase in oxygen content resulted in the decrease in electron conductivity⁴⁹. Therefore, Magnéli phase titanium suboxides have a high electrical conductivity that is comparable to carbon⁵⁰.

A subsequent question that arises is how the presence of extended-defect structures is related to the increase of electrical conductivity. For that reason, a systematic study on the electronic structure of $\text{Ti}_n\text{O}_{2n-1}$ is required. As can be seen from the total density of states (TDOS) plot for anatase TiO_2 in Fig. 1.18, the Fermi level is located just above its valence band maximum (VBM), showing a typical semiconductor character. For the Magnéli phase $\text{Ti}_n\text{O}_{2n-1}$ ($4 \leq n \leq 9$), the Fermi level moves to the conduction band, indicating that there are free electrons in the bottom of the conduction band as seen in Fig. 1.18.

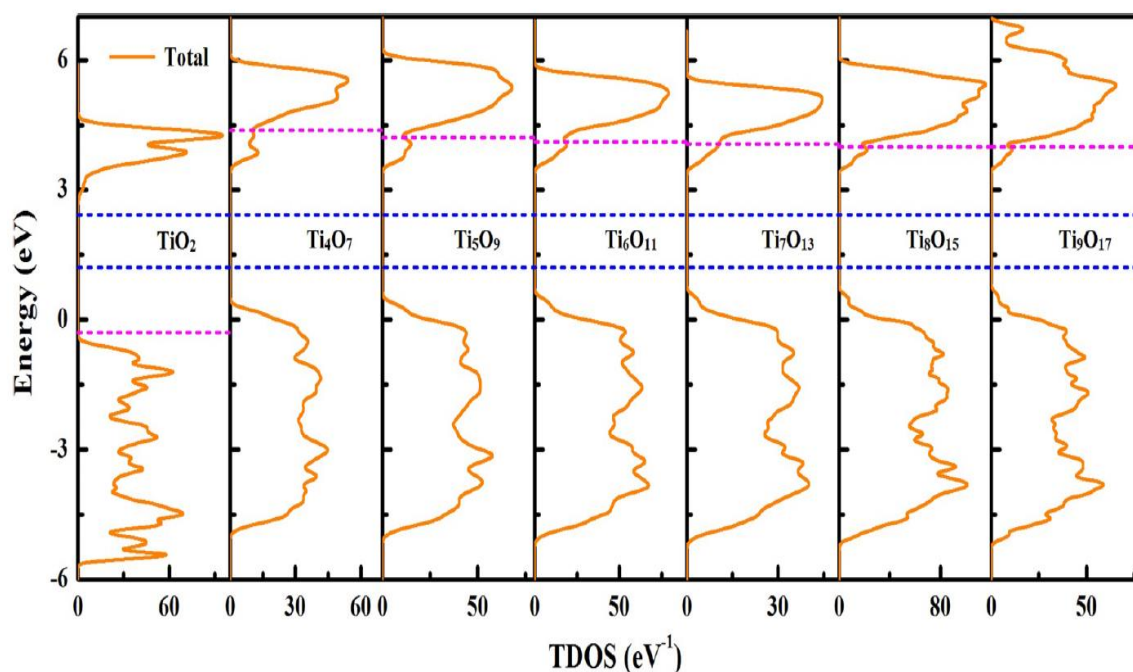


Figure 1.18. The HSE06 calculated TDOS of pure anatase TiO_2 and Magnéli phase $\text{Ti}_n\text{O}_{2n-1}$ ($4 \leq n \leq 9$). The highest occupied state is the Fermi level displayed with a magenta dashed line. The blue dashed lines represent the energy positions of the hydrogen production level (upper) and the water oxidation level (lower), respectively⁵¹.

A typical signature of the presence of defects in the bulk or at the surface of a material is the appearance of new states in the gap. Therefore, the positioning of $\text{Ti}_n\text{O}_{2n-1}$ defect levels is the key for understanding the enhanced transport properties these polymorphs

exhibit. Planar defects, just like regular point defects on rutile TiO₂ are introduced mainly due to oxygen vacancies present in the structure. These defects position localized mid gap states closer to the conduction band minimum (CBM), essentially playing the role of intrinsic dopants in these systems. Furthermore, titanium interstitials are also known to introduce mid gap states close to the conduction band minimum³⁸. Calculations showed⁵² a metallic behavior for Ti₄O₇ and semiconductor for the other polymorphs⁴⁹ at room temperature .

These localized mid gap states have an effect on the bandgap of the material, resulting in bandgap narrowing. Pure Magnéli phase Ti_nO_{2n-1} have 0.5 eV smaller than that of anatase TiO₂ rated at approximately 2.5 eV, whereas nitrogen doped Magnéli phase Ti_nO_{2n-1} has an optical response with a bandgap value of approximately 2 eV⁵¹.

Arif *et al* reported the synthesis of highly conductive sub-30 nm Magnéli phase TiO_x with remarkable electrochemical stability in strongly oxidizing environments⁵³. Liborio *et al* performed first-principle thermodynamic study of oxygen defective Magnéli phase titanium suboxides discussing the proposed mechanism for the formation of the crystallographic shear planes in rutile⁵⁴. Toyoda *et al* reported the production of carbon-coated Magnéli phase Ti_nO_{2n-1} with enhanced visible-driven photocatalytic performance on the degradation of pollutants in which the carbon shell increased the concentration of the pollutant around the particle⁵⁵.

1.5 - TiO₂ As a Photocatalyst

The word photocatalysis, as the name suggests is a procedure which combines catalysis with light. A photocatalyst is a material that helps to accelerate and enhance a light-induced reaction without being consumed in the process. Research in the field of photocatalysis has seen significant progress in the last decades due to its potential to use solar energy for environmental and energy-related applications.

Since the pioneering work of Fujishima and Honda in 1972⁵⁶, there have been major improvements of photocatalytic materials, closely correlated with advances in nanotechnology. Among the various materials that have been studied for photocatalysis, TiO₂ has been the most widely employed photocatalyst due to its high photocatalytic activity, non-toxicity, low cost, and its chemical stability.

The nano-semiconductor driven photocatalysis offers a lot of advantages mainly due to the surface-to-volume ratio nanomaterials exhibit. Taking into account TiO₂ crystal parameters and assuming spherical nanoparticles, with an early estimate we can say that less of 20% of the constituent atoms are at the surface of 30 nm nanoparticles, whereas 35-40% of the atoms are localized at the surface of 10 nm nanoparticles. Hence, properties

which are usually determined by the molecular structure of the bulk lattice now become increasingly dominated by the defect structure of the surface.

The basic photocatalytic reaction initiates from the generation of electron-hole pairs upon light irradiation, a process also known as charge separation. The incident photons must have an energy equal or greater than the photocatalyst's bandgap energy so that the electrons be excited from the conduction band (CB) to the valence band (VB), leaving the holes in the VB.

These photogenerated electron-hole pairs may further be involved in the following processes.

- Successfully migrate to the surface of the semiconductor.
- Be captured by the defect sites in bulk and / or on the surface region of the semiconductor.
- Recombine and release the energy in the form of heat (lattice vibration) or light (photon generation).

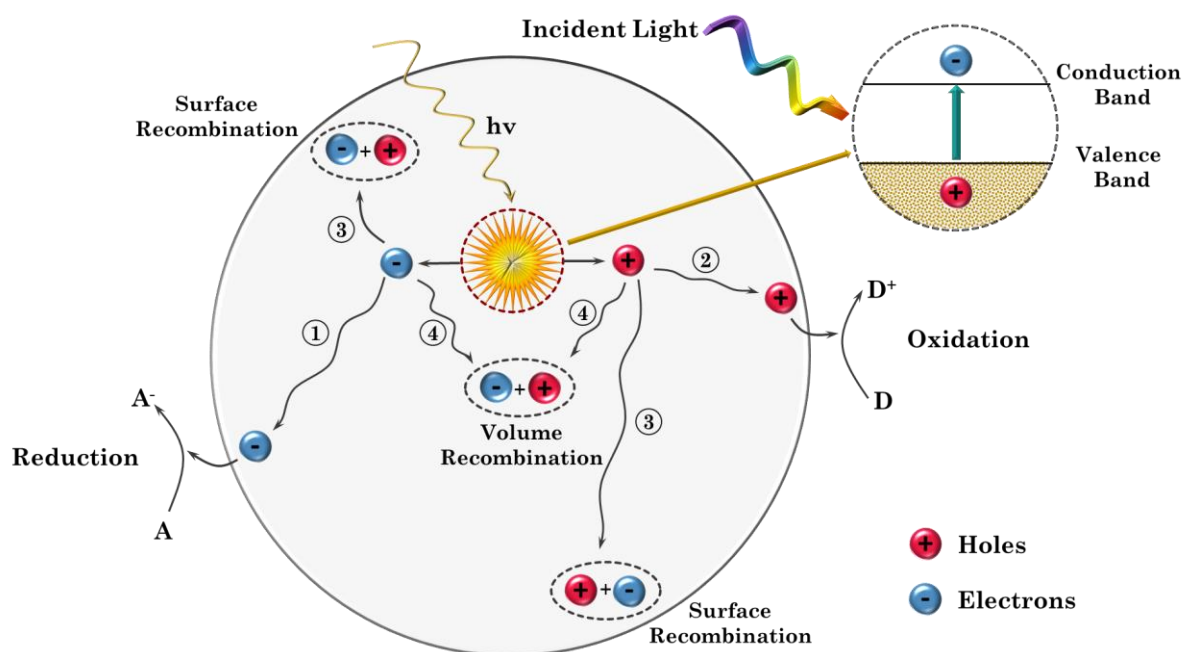


Figure 1.19. Schematic demonstration of the photocatalytic mechanism of a semiconductor. A is electron acceptor, D is electron donor.

The last two processes are viewed as deactivation processes since the photogenerated electrons and holes do not contribute to the photocatalytic reaction. The defect sites in the bulk and on the surface may serve as recombination centers for the charge carriers, degrading the photocatalytic yield.

In principle, a photocatalytic reaction consists of two “half” reactions, oxidation and reduction. The reduction reaction is governed by the electrons in the conduction band (CB) whereas the oxidation reaction is governed by the holes in the valence band (VB). The basic factor controlling the photo-induced electron excitation is the position of the redox potentials. For the water splitting reaction, the position of the CB should be more negative than the redox potential of H⁺/H₂, while the position of the VB should be more positive than the redox potential of O₂/H₂O. As shown in Fig. 1.10, both TiO₂ polymorphs are capable of photocatalytic water splitting. The mixed ratios of anatase and rutile like the commercially available mixed-phase anatase rutile P25 TiO₂ nanoparticles, show enhanced photocatalytic activity compared to their single counterparts⁵⁷.

Two primary factors must be taken into account when designing the systems for conducting photocatalytic reactions. The first would be the efficiency of e⁻/h⁺ pair generation upon radiation. The second is the efficiency of the e⁻/h⁺ pair separation before they lose their redox ability due to recombination. The photocatalytic efficiency could be enhanced significantly by addressing the following primary issues. The first has to do with the light absorption. The light absorption process determines the amount of excited charges, which means that more charge carriers are likely to be accumulated on the surface if more light can be absorbed by the photocatalyst. TiO₂ is a relatively wide bandgap semiconductor photocatalyst (3.2 eV for anatase, 3.0 eV for rutile) and requires ultraviolet (UV) light for photoactivation resulting in very low efficiency when utilizing solar light. UV radiation accounts only for about 4% of the solar spectrum compared to visible light which is 45%⁵⁸. Therefore, shifting the onset of the response from the UV to the visible region can result in a higher rate of charge separation and enhancement of their overall activity. This is usually done with bandgap engineering. The second has to do with electron-hole recombination. The photogenerated electrons and holes should be transported and separated efficiently in the photocatalyst because fast recombination of charge carriers will otherwise result in low reactivity. TiO₂ suffers from fast charge recombination which deteriorates the photocatalytic activity⁵⁹. Suppression of the electron-hole recombination is vital for high photocatalytic efficiency. Defect sites are known to act as recombination centers, howbeit the lifetime of photogenerated charge carriers in defect-rich materials has been found to be longer than in defect-less single crystals. The trapping of charge carriers reduces the reactivity to some extent, but it decelerates recombination and hence enhances the overall photocatalytic efficiency⁶⁰. Therefore, defect formation in the form of oxygen vacancies in TiO₂ particles can reduce charge recombination and significantly boost the photocatalytic yield. The last part has to do with surface chemistry. As discussed earlier, photocatalytic reactions occur at the surface of the photocatalyst. Therefore, factors like porosity, specific surface area and affinity strongly influence the photocatalytic efficiency. TiO₂ exhibits low porosity and has

1.5 – TiO₂ As a Photocatalyst

a polar surface both of which trammel the photocatalytic process⁶¹. This setback can be circumvented via surface functionalization. Coating TiO₂ particles with a porous shell with high surface area can have a positive effect on the photocatalytic procedure.

Defects in the form of oxygen vacancies in TiO_{2-x} suboxides can result in high photocatalytic efficiency since defects are shown to retard charge recombination. Furthermore, defect states position new energy levels in the bandgap which lead to bandgap narrowing and consequently to visible-driven photocatalysis. Magnéli phase titanium suboxides exhibit metallic (Ti₄O₇) and semiconductive behavior in room temperature accompanied with high conductivity. This ensures high carrier mobility which further facilitates the charge separation in the photocatalytic process and the migration of the charge carriers to the surface. Carbon-coating can protect suboxides from oxidation and can efficiently reduce the recombination of photogenerated carriers by accelerating surface electron transfer. In Table 1.4, we report the photocatalytic yield of modified titania photocatalyst, in the basis of the modifications discussed earlier.

Photocatalyst	Co Catalyst	Illumination	Application	Yield	Ref.
Mixed Phase Magnéli Ti _n O _{2n-1}	No	Solar Light	H ₂ Evolution	145 $\mu\text{mol h}^{-1} \text{g}^{-1}$	62
Mixed Phase Magnéli Ti _n O _{2n-1}	Pt	UV	H ₂ Evolution	5432 $\mu\text{mol h}^{-1} \text{g}^{-1}$	40
Carbon-coated Magneli phase Ti _n O _{2n-1} @C	No	Visible Light	Decomposition of Iminoctadine Triacetate (IT)	40% in 280 min	55
Acid washed carbon-coated C / TiO _{2-x}	No	Visible Light	Photodegradation of Rhodamine B (RhB)	100% in 30 min	35
	Pt	Solar Light	H ₂ Evolution	8.6 $\text{mmol h}^{-1} \text{g}^{-1}$	35
Carbon-coated TiO ₂ @C	No	300W lamp 400nm filter	Degradation of 4-chlorophenol	90% in 60min	63
	No	Solar Light	Degradation of Methylene Blue (MB)	90% in 60min	63

Table 1.4. Photocatalytic efficiencies of various modified TiO₂ polymorphs.

1.6 – Nanomaterial Synthesis

1.6.1 – Wet Chemical Synthesis

Along with their early applications in the 1980s, efforts have been made to invent synthetic methods for nanoparticles with desired properties. Two approaches have been developed describing the different possibilities for the synthesis of nanostructures. These manufacturing approaches fall under two categories: top-down and bottom-up, which differ in degrees of quality, speed and cost.

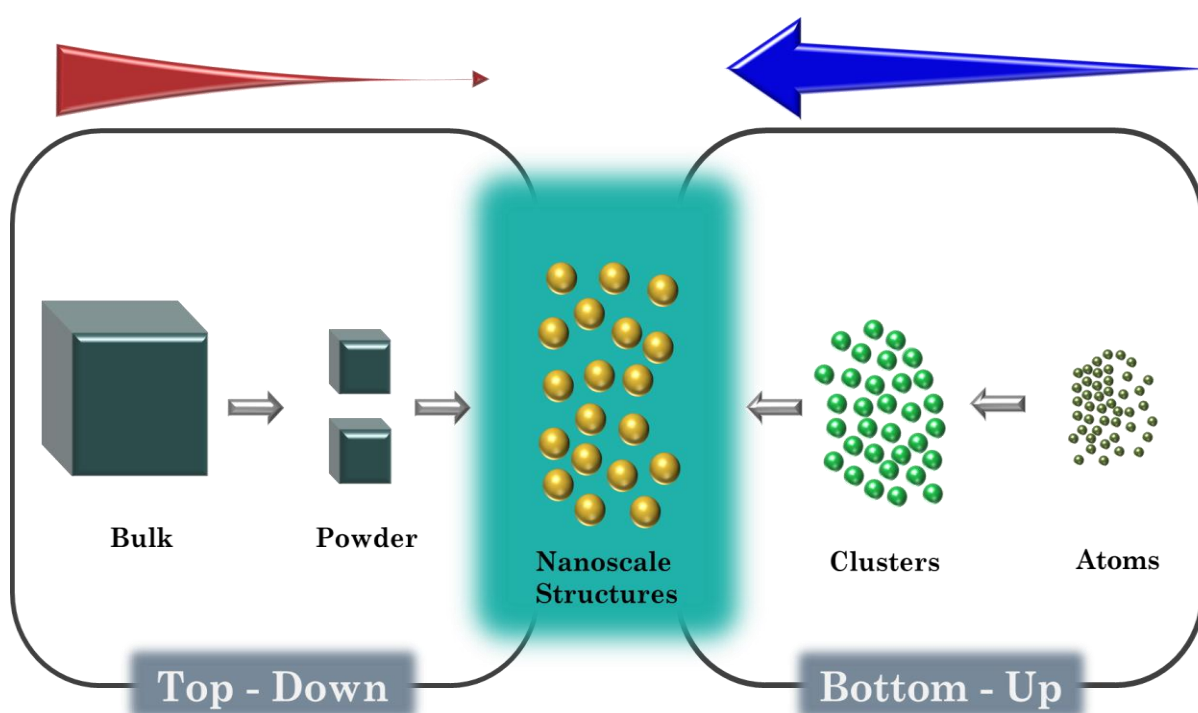


Figure 1.20. The concept of top-down and bottom-up technology: different methods for nanoparticle synthesis.

The top-down approach is essentially the breaking down of the bulk material into nanosized powders. Control of the size of the resulted nanomaterials can be quite tricky. Furthermore, most of the nanomaterials contain a wide range of size distribution and have non-uniform shapes which hinders applicability. In the bottom-up approach on the contrary atomic or molecular species are integrated to form nanostructures. Nanomaterials are constructed by physical or chemical methods using controlled manipulation of self-assembly of atoms and molecules.

1.6.2 – Flame Spray Pyrolysis (FSP)

The bottom-up approach is largely based on wet chemical synthesis, which is relatively simple, modular and low in cost. Wet chemical synthesis includes various methods like sol-gel, precipitation, solvothermal which enables the design of nanomaterials with tailored properties⁶⁴.

The efficiency of wet chemical synthesis is sometimes afflicted by certain limiting factors. Among them are the presence of wastes, the limited quantity of the final product, low crystallinity of the particles, presence of impurities as well as being multi step processes.

1.6.2 – Flame Spray Pyrolysis (FSP)

Particle production from a flame process has a history that dates to the ancient times. The first flame-made particles, soot can be traced back to the prehistoric times, where the flame spray technique had been practiced in a non-intentional manner. The principles of the process back then could not be understood, but it was not until 1971 and the pioneering work of G.D. Ulrich⁶⁵ that the principles of particle formation in a flame process were addressed for the first time. Since then, the field of aerosol technology has rapidly evolved in the past years and has resulted in the development of functional nanomaterials⁶⁶.

Flame Spray Pyrolysis (FSP) is a one-step flame-assisted liquid-fed particle formation process⁶⁷. This technology involving the flame spraying of a precursor solution is based on the formation of nanoparticles from the gas or vapor phase in a flame. In FSP, the precursor is in liquid form and dissolved in high combustion enthalpy organic solvents. The combustion of the precursor solution leads to the controlled synthesis of high purity agglomerated nanoparticles⁶⁸.

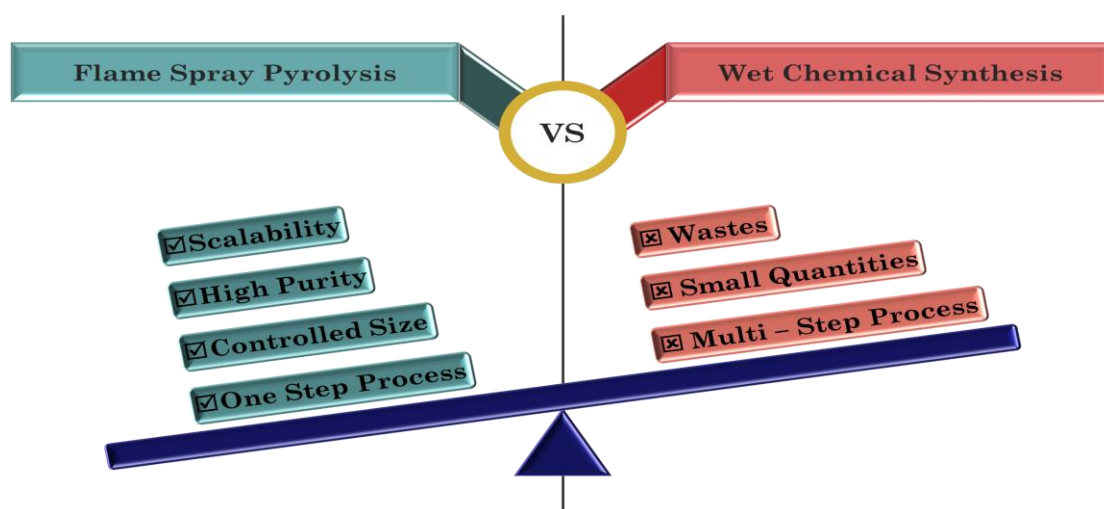


Figure 1.21. Comparison of Flame Spray Pyrolysis synthesis and conventional wet chemical synthesis.

1.6.2 – Flame Spray Pyrolysis (FSP)

The broad use of the FSP process stems from the distinct advantages over wet-chemistry synthesis methods. The following key reasons make FSP process attractive for the manufacturing of nanoscale structures⁶⁹:

- FSP process does not generate liquid byproducts.
- Easier collection of particles.
- High purity nano powders.
- Non-equilibrium metastable phases can be captured.

The apparent benefits this technique exhibits do not come without some disadvantages that must be dealt with. Among them are:

- High temperatures lead to aggregates (hard agglomerates).
- Cost of impurity-free precursors.
- Different particle morphologies (hollow, porous, inhomogeneous).
- Polydisperse particle size distribution.

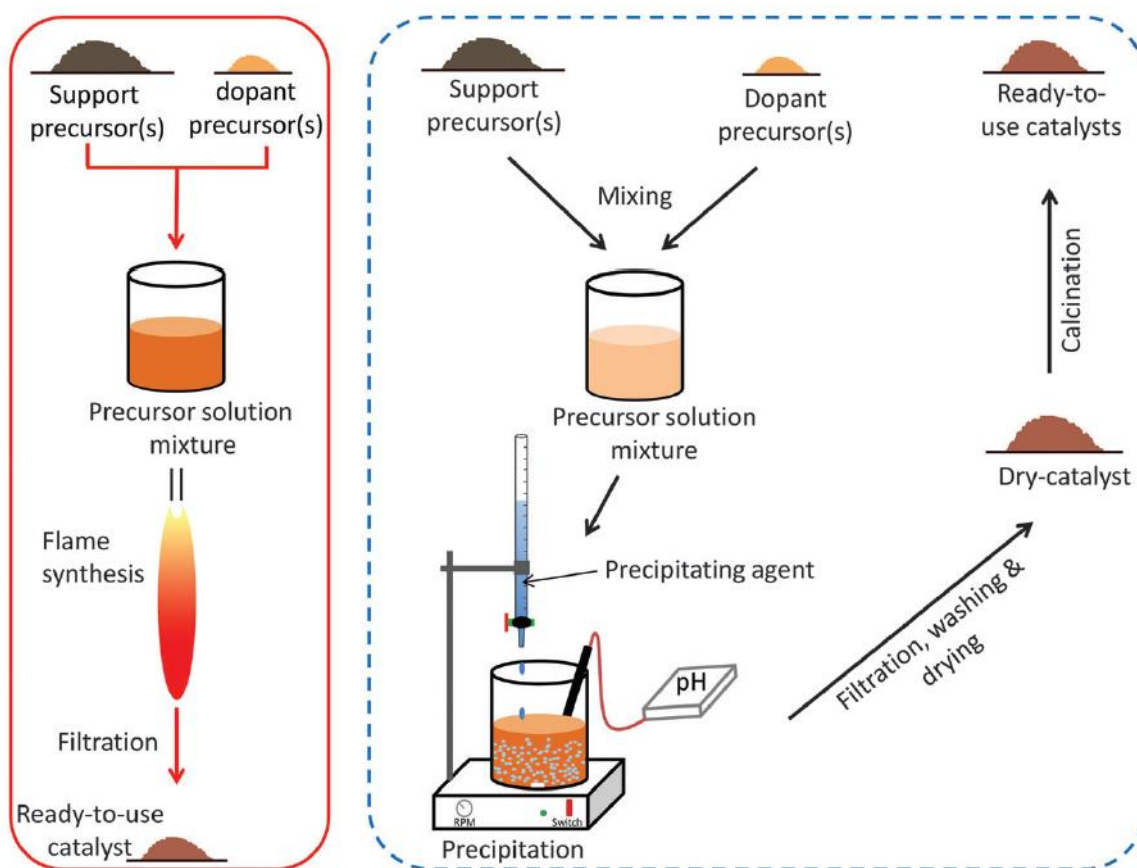


Figure 1.22. Comparison of flame synthesis with classical wet-preparation method of catalysts⁷⁰.

1.6.2 – Flame Spray Pyrolysis (FSP)

It is quite common to coat the surface of particles to enhance their performance in applications or in the case of metal suboxides to protect the core particle from oxidation. The synthesis and coating of such particles are two distinct and usually multistep processes, forming first the core and subsequently the coating shell. The development of a process that can combine flame particle synthesis and particle coating in a single gas phase processes could make up for the burdensome multi-step wet-phase treatment. Furthermore, particle collection from gases is easier than from liquid streams, would not involve hard-to-clean liquid by products and the fewer step process would result in high purity products. FSP scalability allows the *in situ* coating of metal oxides and metal suboxides with metal oxide or non-metal shells in a core-shell configuration^{71,72}.

In this thesis, we developed a method for coating metal oxides and reduced metal oxides *in situ* with carbon. Our method was implemented in TiO₂ oxide and TiO_{2-x} suboxide nanoparticles. The role of the carbon shell is important as:

- Protects the inner TiO_{2-x} core from oxidation.
- Serves as an active site for chemical reactions to take place.
- Eases surface electron transfer.
- Functionalization of the shell is versatile.

FSP made TiO₂ oxide and TiO_{2-x} suboxide nanoparticles were calcined under reducing atmospheres (CH₄) and at different temperatures and duration to study the possible creation of titanium novel phases like Magnéli phases.

1.7 – M.Sc. Thesis Scope

The scope of the present thesis is:

- (i) Development of methodology for the *in situ* carbon coating of metal oxides and suboxides and in our case titanium oxides $\text{TiO}_2@\text{C}$ and suboxides $\text{TiO}_{2-x}@\text{C}$.
- (ii) Control of the carbon shell in terms of thickness and graphitization.
- (iii) The effect of calcination under carbon rich-atmospheres in TiO_2 oxides and TiO_{2-x} suboxides.
- (iv) The presence of novel phases like Magnéli phase titanium suboxides has been extensively addressed.
- (v) The nature of defects and their correlation with the atmosphere in the burner chamber during the FSP particle synthesis process.
- (vi) Preliminary evaluation of the photocatalytic efficiency of the carbon-coated and carbothermal-treated titanium oxides and suboxides by *in situ* monitoring of the OH^\cdot radical concentration using Electron Paramagnetic Resonance (EPR) spectroscopy.

Chapter 2

Experimental Methods

2.1 - X-Ray Diffraction

X-Ray Diffraction (XRD) is a technique used for studying the crystal structure of materials. The basis of this technique is the constructive interference of monochromatic X-Rays and a crystalline sample, when certain geometrical conditions are met. The resulting diffraction pattern is specific for each material and can be used for structural characterization of materials.

2.1.1 - XRD Basic Principles

The interaction of the incident rays with the sample produces constructive interference (and a diffracted ray) when conditions satisfy Bragg's Law⁷³:

$$2d \sin \theta = n\lambda \quad (2.1)$$

where n is an integer number, θ is the diffraction angle, d is the interplanar spacing generating the diffraction and λ is the wavelength of the incident X-Rays.

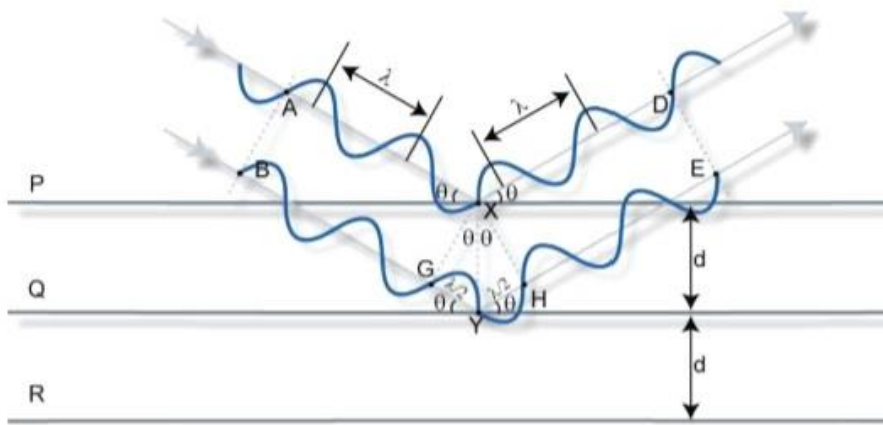


Figure 2.1. Fulfillment of the Bragg Equation.

2.1.1 – XRD Basic Principles

The main difference between powder (pXRD) and crystal diffraction is the degree of texturing in the sample. If a single crystal were used, there would be a small chance a particular set of planes to be in the correct position to satisfy Bragg's Law. In contrast, powdering a crystalline material produces many smaller crystals covering every possible crystalline orientation. Therefore, a significantly larger number of planes would be in the proper orientation to satisfy Bragg's Law. The diffraction pattern is obtained by scanning the sample through a range of 2θ angles.

There are 3 basic components that an X-Ray diffractometer consists of: an X-Ray source, a sample holder and an X-Ray detector.

The source used in diffractometers is usually X-Rays since their wavelength is up to a few nanometers which is comparable with inter atomic spacing. X-Rays are generated in a cathode tube by heating a filament to produce electrons, and then accelerating the electrons towards a target by applying a voltage. When these electrons have energy enough to dislodge inner shell electrons of the target material, X-Ray spectra are produced with the most common component being K_{α} radiation. The most widely used X-Ray source is $\text{Cu } K_{\alpha}$ with $\lambda=1.5418\text{\AA}$. Filtering the radiation with monochromators produces the monochromatic X-Rays needed for diffraction.

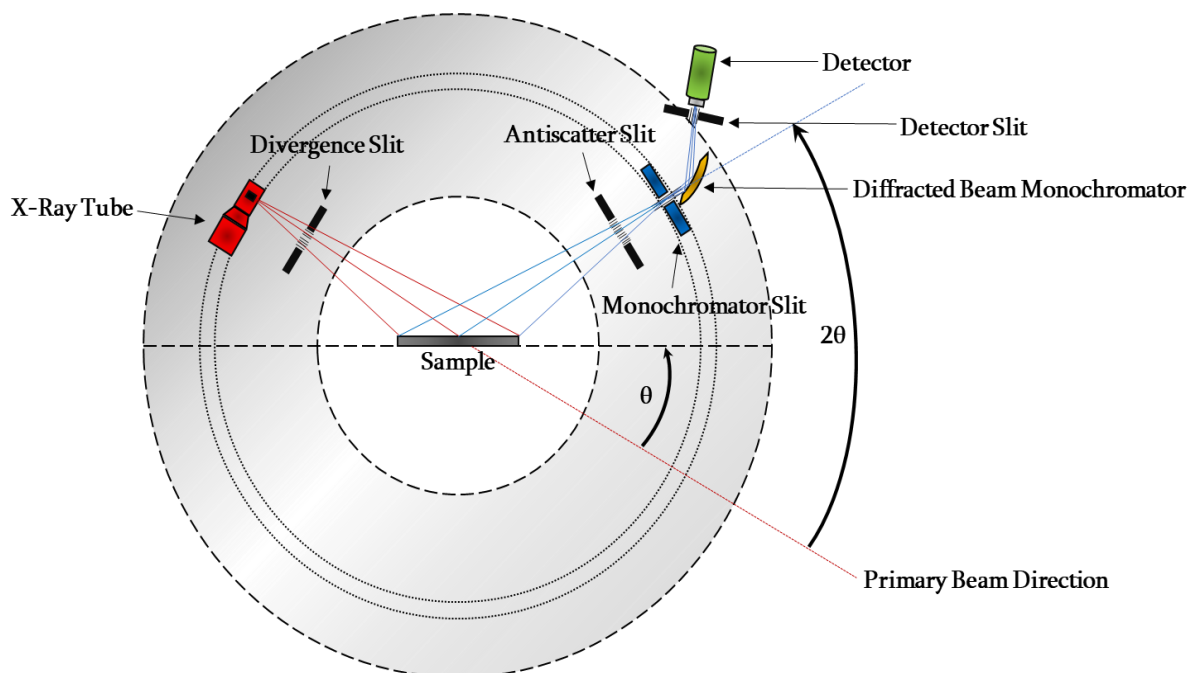


Figure 2.2. Bragg-Brentano geometry and beam path of the diffractometer.

2.1.2 – Calculation of Nanocrystal Size – Scherrer Equation

As soon as the X-Rays are produced, they are collimated and directed onto the sample. As mentioned above, every time Eq. 2.1 is fulfilled, constructive interference occurs and a peak in intensity appears, since the detector measures the intensity of the reflected radiation. As shown in Fig. 2.2, the X-Ray source rotates around at an angle θ , the detector is mounted to collect the reflected X-Rays and rotates at an angle 2θ . This geometry is usually found in most diffractometers and is called Bragg-Brentano geometry.

Typical X-Ray powder diffraction patterns are usually between 5° to 80° and are recorded as a function of 2θ angle versus the peak intensity.

2.1.2 Calculation of Nanocrystal Size – Scherrer Equation

XRD peaks contain information concerning the material's phase composition and crystal structure. We can also relate the broadening of the Bragg peaks with the nanocrystallite's size with a formula known as Scherrer equation⁷⁴ and is expressed as

$$d_{XRD} = \frac{K\lambda}{\beta \cos \theta} \quad (2.2)$$

where d_{XRD} is the mean crystal size, K is a dimensionless constant (0.9), λ is the wavelength of the X-Rays and β is the width of the Bragg peak at half maximum intensity (FWHM), measured in radians.

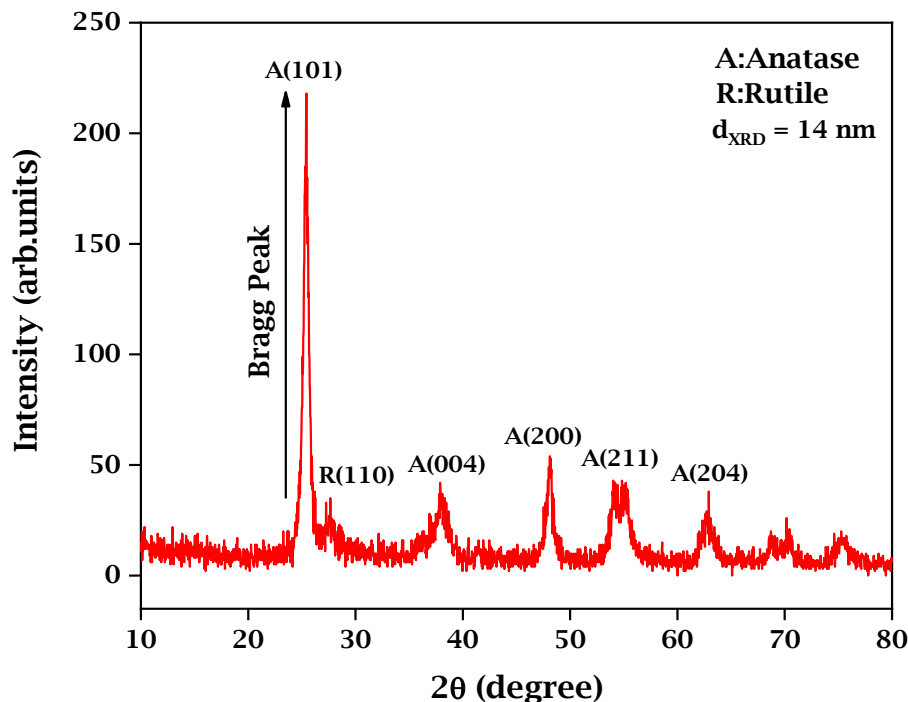


Figure 2.3. Typical XRD pattern of TiO₂ NPs, including Miller indices and the particle mean size d_{XRD} .

2.1.3 – XRD Experimental Set-Up

The Scherrer equation can only be used on nanoscale particles ranging from 1 nm up to 0.2 μm . Fig. 2.3 shows a typical XRD pattern of TiO_2 nanoparticles (NPs) with the Bragg peaks shown for the two phases: anatase at 25°, 38°, 48°, 55° and 63° and rutile at 27°.

2.1.3 - XRD Experimental Set-Up (Dept. of Physics UOI)

XRD Diffraction Patterns of the nanoparticles were obtained with a D8 Advance Bruker Diffractometer (Fig. 2.4) using (40kV, 40mA) $\lambda = 0.154 \text{ nm}$ Cu K_{α} radiation with a Lynxeye detector. The sample is placed in a silicon holder. All the parameters including angles wide, angle step, residence time, rotation of sample holder are defined by a Bruker software.

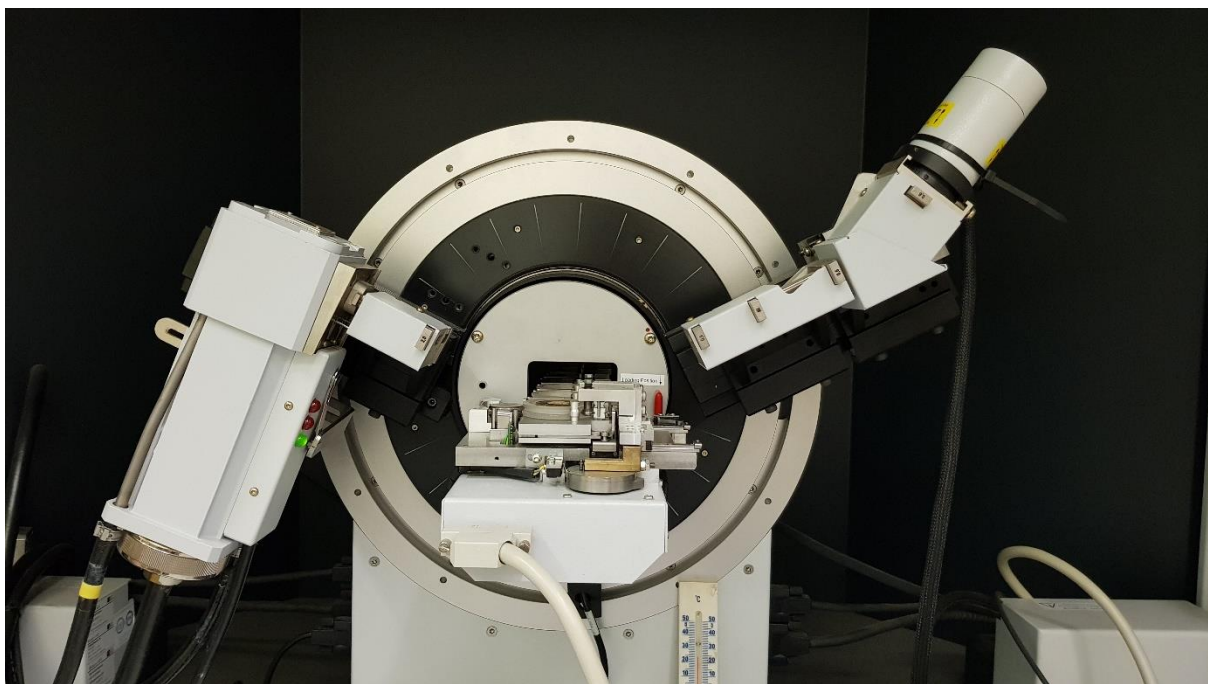


Figure 2.4. Bruker D8 Advance Diffractometer.

2.2 - Raman Spectroscopy

Raman Spectroscopy is a non-destructive technique that provides information concerning molecular interactions, chemical structure, crystallinity and phases. The basis of this technique is the inelastic light scattering due to the interaction of the incident light with the material's chemical bonds. A sample is irradiated with a single frequency radiation (usually a laser) and the energy difference between the incident beam and the scattered beam is recorded. It was first observed by Raman⁷⁵ in 1928. Each material or molecule has a distinct Raman spectrum thus enabling us to identify them.

2.2.1 - Raman Spectroscopy Basic Principles

When light interacts with matter, the photons may be absorbed, scattered or may not interact with the material and pass straight through it. Raman scattering involves the inelastic scattering of light upon interaction with the molecule. In Raman scattering, photons interact with the molecule and cause distortion (polarization) of the electronic cloud around the nuclei and a short-lived state is formed called 'virtual state'. This 'virtual state' is formed by the electrons and the photons in the molecule in which time nuclear motion is not induced. This state is unstable, so the photons are emitted as scattered radiation.

We can discern two cases: if only electron cloud distortion is involved in scattering with no nuclear motion, the photons are scattered with minor frequency changes and hence the process is regarded as elastic scattering. This process is called Rayleigh scattering and it is the most dominant process. However, if nuclear motion is induced during the scattering process, energy transfer will occur either from the incident photon to the molecule or from the molecule to the scattered photon. This process is inelastic scattering and there is an energy difference of one vibrational unit between the incident and the scattered photon. This is Raman scattering⁷⁶.

Since the virtual states are not real states and are created only when the photons interact with the electrons, their energy depends on the frequency of the light source. Depending on which vibrational energy state the process starts we have Rayleigh scattering where there is no energy change and the photons return to the original energy state, Stokes Raman scattering where the process starts with a molecule in the ground vibrational state and Anti-Stokes Raman scattering where the process starts with a molecule in an excited vibrational state as shown in Fig. 2.5. It should be noted that at room temperature, most molecules are in the lowest vibrational energy state, so Stokes Raman scattering is the most favorable one.

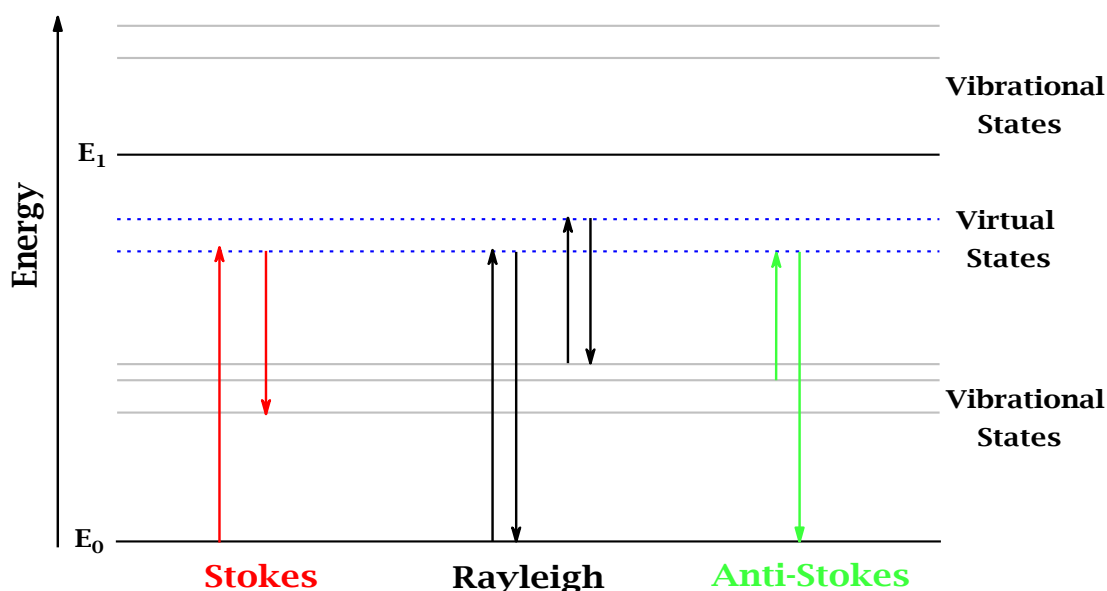


Figure 2.5. Diagram of Rayleigh and Raman Scattering process. In Stokes scattering the incident photon has greater energy than the scattered photon whereas in Anti-Stokes scattering the incident photon is of lower energy than the scattered one.

As discussed above, interaction between the photons and the molecule lead to distortion (polarization) of the electron cloud. Distortion depends on the ability of the electrons to polarize. The parameter used to describe this ability is called polarizability a . The effect on the electron cloud is on all directions so in order to take into consideration all interactions we can assume that dipoles are created and thus:

$$\vec{P} = a\vec{E} \quad (2.3)$$

The polarizability a is a tensor whose dependence to molecular vibrations can be expressed as a function of normal coordinates using a Taylor approximation⁷⁷:

$$a_{ij} = a_{ij}^0 + \left(\frac{\partial a_{ij}}{\partial Q} \right) \Big|_{Q=Q_0} \times Q, \text{ with } Q = Q_0 \cos(2\pi\nu_{vib}t) \quad (2.4)$$

Raman scattering as discussed above occurs only when vibrations change polarizability. Mathematically this can be written as $(\partial a_{ij}/\partial Q \neq 0)$. The signal intensity is predicted with the following formula:

$$I_{\text{Raman}} \propto I_{\text{laser}} \bar{v}^4 |e_0 a e_s|^2 d\Omega \quad (2.5)$$

2.2.2 – Raman Measurement Set-Up

where I_{Raman} is the Raman signal intensity, I_{laser} is the incident laser intensity, e_0 and e_s are unit vectors representing laser polarization and direction of observation, v the wave number, $d\Omega$ is the solid angle of light collection and a is the polarizability.

From Eq. 2.5 it is obvious that two of variable parameters are under the control of the analyst. That would be the laser power and the frequency of the incident light.

2.2.2 - Raman Measurement Set-Up

A Raman spectrometer basic configuration consists of 3 different parts: a source of radiation which is in general a laser with a specific wavelength, a spectrometer that disperses the scattered light and a detector that detects the scattered light.

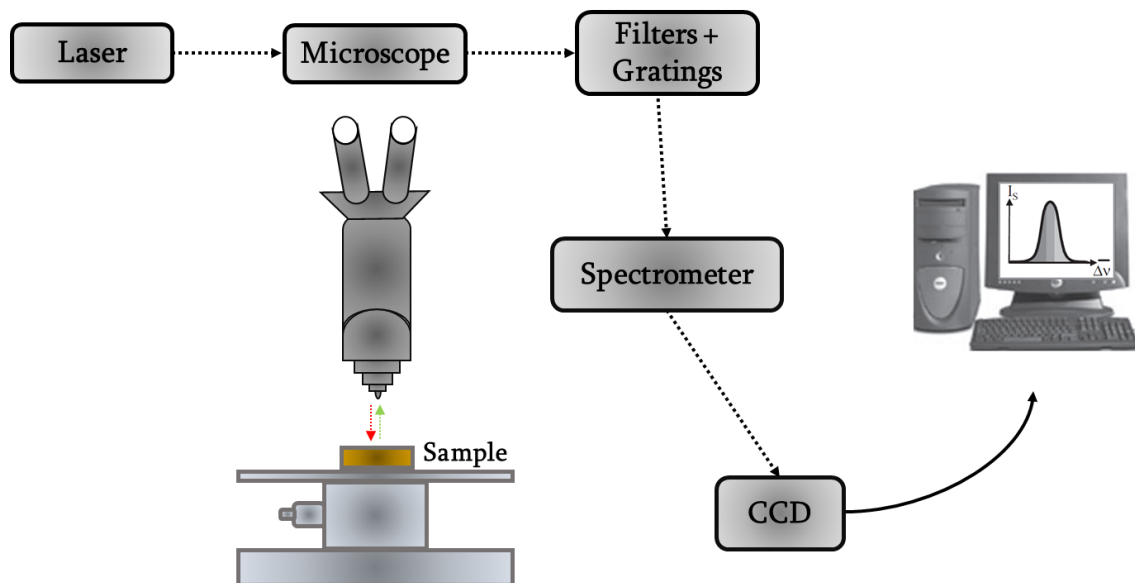


Figure 2.6. Overview and principle of a Raman microscope spectrometer

The light source of a Raman spectrometer is usually a laser with a specific wavelength. The laser's wavelength can vary from UV to the visible and near infrared depending on the application. The most common used lasers are the 514.5 nm Ar⁺ ion laser, the 532 nm Nd:Yag laser and the 785 nm. The 785 nm laser offers the best balance between scattering efficiency, influence of fluorescence and detector efficiency. Taking into consideration Eq. 2.5 and since the wave number is inversely proportional to the wavelength, lasers with greater wavelength allow greater laser intensity to be used. Fig. 2.6 depicts the overview and principle of a Raman microscope spectrometer. The laser beam is directed to the sample and upon interaction, the scattered beam passes through a filter which only allows radiation with different wavelength to pass through i.e. Raman scattering light.

2.2.2 – Raman Measurement Set-Up

The scattered light is directed to a monochromator which disperses the light with the aid of a grating. A CCD captures the dispersed light and converts photo current to electric current at which point the spectrum is generated.

A Raman spectrum contains much information depending on the parameters that each time are assessed. There are two parameters that will influence the spectrum. Parameters governing vibration-induced charge transfers will set Raman scattering intensity whereas parameters governing the bond “dynamics” will set the peak positions.

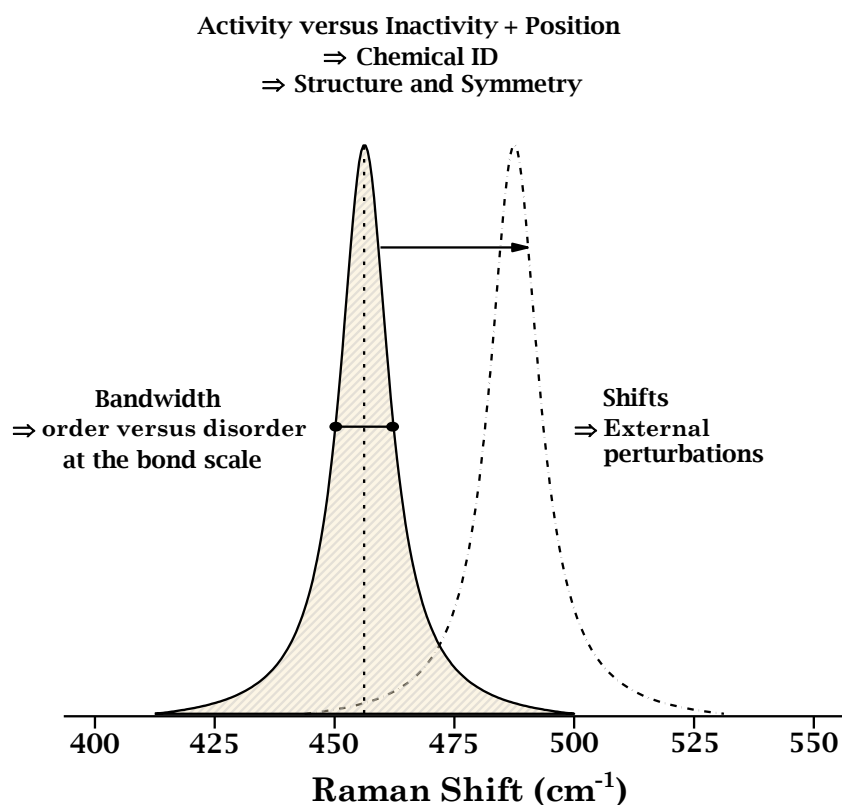


Figure 2.7. Raman parameters and their influence in the spectrum

In Fig. 2.7 we can see the parameters that influence the spectrum. The main variable is peak position which is the “fingerprint” for each molecule or material. Bandwidth determines the order of the bonds whereas shifts to peak positions are attributed to external perturbations. Fig. 2.8 shows a typical Raman spectrum of TiO₂ nanoparticles along with peak position for the two phases.

2.2.3 – Raman Experimental Set-Up

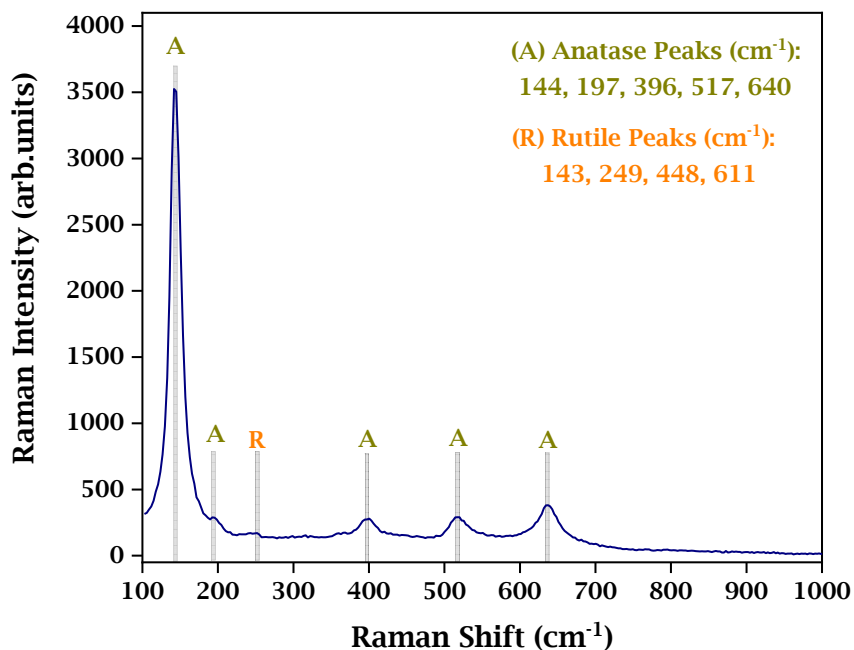


Figure 2.8. Typical Raman spectrum of TiO₂ nanoparticles along with peak positions

2.2.3 - Raman Experimental Set-Up (Dept. of Physics UOI)

Raman spectroscopy measurements were taken using a Horiba XploRA Plus Raman microscope coupled to an Olympus BX41 microscope and using a 785 nm laser as an excitation source. The microscope is coupled to a CCD which helped using low laser intensities of 1% or 10% in samples that were experiencing phase changes due to heating. Spectrum were recorded and processed with Lab Spec software.

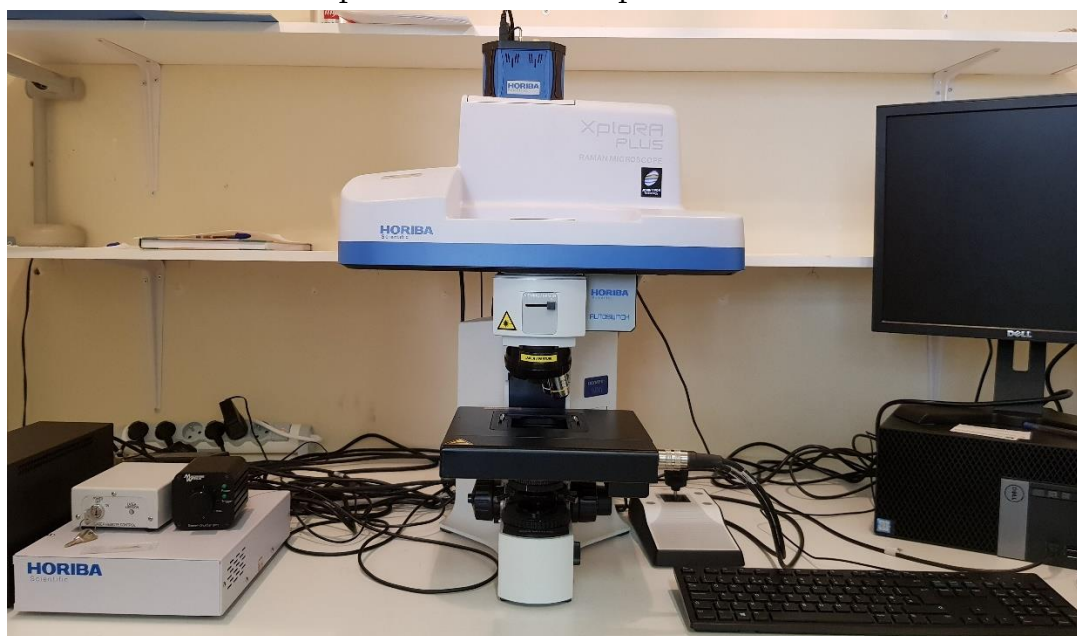


Figure 2.9. Horiba XploRA PLUS Raman microscope

2.3 - Uv-Vis Diffuse Reflectance Spectroscopy (DRS)

Ultraviolet-Visible Diffuse Reflectance Spectroscopy (Uv-Vis DRS) is a non-destructive technique used for the determination of parameters associated with the material's optical properties such as refractive index, reflectivity, absorption. The scattered intensity of an incident light beam is scanned as a function of the wavelength and is analyzed with respect to its macroscopic optical characteristics, such as reflectance or absorbance.

2.3.1 - DRS Basic Principles

When light interacts with a medium, two different types of reflection can occur⁷⁸: regular or specular reflection which is associated with reflection from smooth surfaces like mirrors and diffuse reflection which is associated with reflection from dull surfaces like powders.

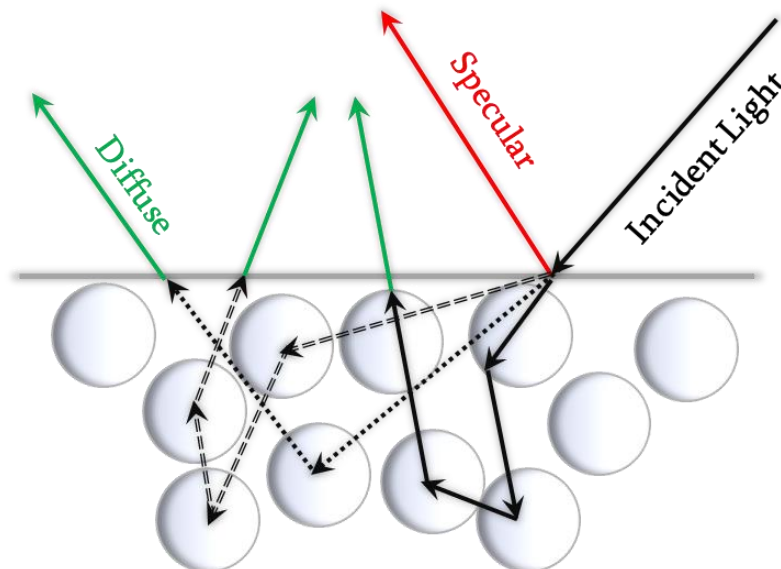


Figure 2.10. Schematic illustration of light trajectories in a scattering sample

As we can see in Fig. 2.10, whereas specular reflection can be treated with theoretically using Fresnel equations, diffuse reflection is the result of many complex mechanisms. When light interacts with a dull surface like a densely packed powdered sample, the sample will experience a combination of reflection, refraction and diffraction (i.e. scattering) of the incident light. Furthermore, in certain materials, light would be also absorbed. Therefore, samples of interest are samples that exhibit simultaneously absorption and scattering of electromagnetic radiation. As a result, these phenomena are treated by the so called two-constant theories referring to the two parameters that must be taken into account which are scattering and absorbance.

2.3.1 – DRS Basic Principles

Since the description of the propagation of light through inhomogeneous materials is the result of different mechanisms only approximate descriptions exist. The most often used theory to describe and analyze diffuse reflectance spectra is the Kubelka-Munk theory. Kubelka-Munk theory allows the calculation of reflectance from a layer that both scatters and absorbs light.

In transmission spectroscopy, transmittance is defined as the fraction of the transmitted to the incident light intensity

$$T = \frac{I}{I_0} \quad (2.6)$$

In an analogous way, the remittance of a diffusively reflecting sample is the ratio between reflected to incident light intensity.

$$R_\infty = \frac{J}{I_0} \quad (2.7)$$

where R_∞ is the absolute remittance, J is the intensity of the reflected radiation and I_0 the intensity of the incident beam as above. In experiment, we don't measure the absolute remittance but the relative remittance defined as the fraction between the sample's remittance to that of a standard sample ($R_{\infty \text{ sample}}/R_{\infty \text{ standard}}$).

As discussed above, Kubelka-Munk is a two-constant theory, meaning that we must relate the results with two constants. In our case, those two constants would be the absorption coefficient K and the scattering coefficient S . Taking approximations Eq. 2.7 becomes:

$$R_\infty = 1 + \frac{K}{S} + \sqrt{\frac{K}{S} \left(2 + \frac{K}{S} \right)} \quad (2.8)$$

This model holds only when the particle's size is comparable or smaller than the wavelength of the incident light, and the diffuse reflection no longer allows to separate the contributions of the reflection, refraction and diffraction. In the case of an infinitely thick sample (meaning that none of the light irradiating the sample penetrates to the bottom of the sample holder) and by solving Eq. 2.8 for K/S , we take the Kubelka-Munk function $F(R_\infty)$:

$$F(R_\infty) = \frac{(1-R_\infty)^2}{2R_\infty} = \frac{K}{S} \quad (2.9)$$

The scattering coefficient S is dominated by the particle size and the refractive index of the sample. It is not a strong function of the wavelength or the absorption coefficient K and thus is considered a constant. In reality, the scattering coefficient varies slowly with wavelength. It does though change significantly with packing density, so powdered samples should be packed carefully.

2.3.2 – Tauc Plot – Determination of Band Gap

Summarizing the above, Kubelka-Munk function is valid under the following conditions: 1) diffuse monochromatic radiation of the powdered sample, 2) an infinite layer thickness, 3) uniform distribution of powders.

2.3.2 - Tauc Plot – Determination of Band Gap

The theory of bands in solids states that the separation between the lowest conduction band and the highest valence band creates the bandgap (E_g) which is an energy range where no electron state exists. Depending on the value of E_g we have insulators, semiconductors and conductors. There are two types of band-to-band transitions:

1. Direct transitions where the momentum is conserved without the participation of a phonon. The two points have the same value in the k-space.
2. Indirect transitions where at least one phonon is required for the conservation of momentum. The two points have different values in the k-space.

There is also another classification between intra-band transitions. Allowed transitions are those occurring as a result of a selection rule whereas forbidden transitions occur in a lower rate only when the approximation associated with the selection rule is not made. Mathematically speaking, allowed transitions have a non-zero matrix element, whereas forbidden transitions have a matrix element equal to zero. In all transitions that occur, there is always a change in energy.

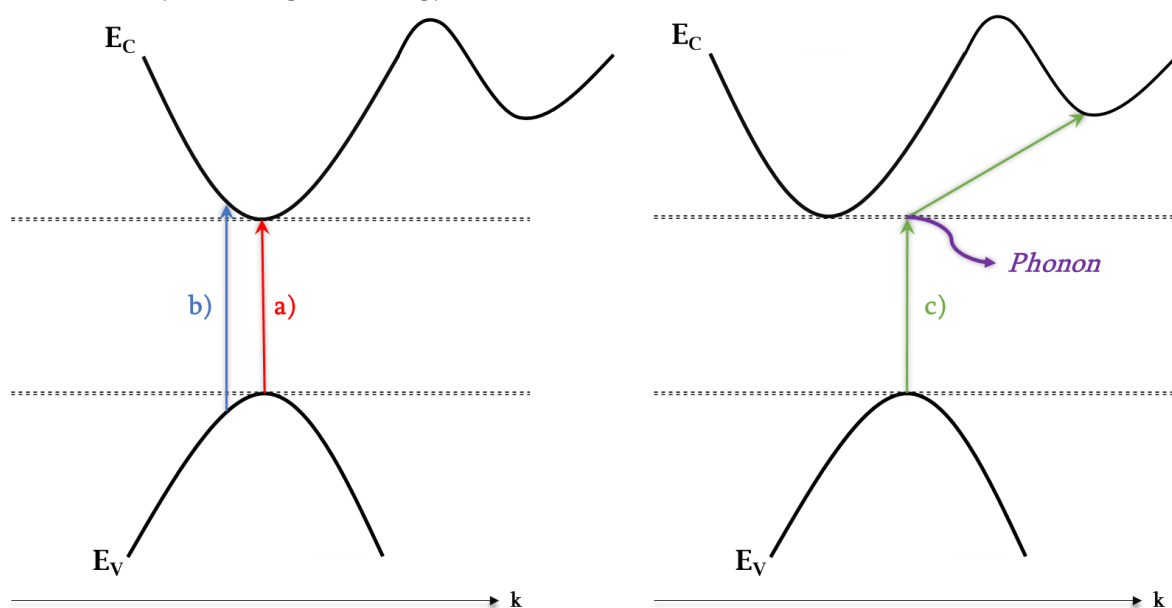


Figure 2.11. Simplified Band transition representation: (a) allowed and (b) forbidden *direct* transition; absorption of a photon with energy E_g can occur without the presence of a phonon; (c) for the *indirect* transition the presence of the phonon is required.

2.3.2 – Tauc Plot – Determination of Band Gap

The Kubelka-Munk function is used for the determination of the optical band gap of semiconductors. As shown above, it depends on the scattering coefficient S and the absorption coefficient K . Assuming that the scattering coefficient S changes negligibly, the Kubelka-Munk function depends solely on K . The correlation between the absorption α connected to the absorption coefficient K and the incident photon energy $E = h\nu$ can be achieved with a correlation function involving also an electronic transition-dependent exponent n .

For the calculation of the optical band gap, Kubelka-Munk function needs to be modified. By multiplying the $F(R)$ with $h\nu$ and using the exponent discussed above we can correlate the $F(R)$ function with the absorption α as follows:

$$(F(R_\infty) \cdot h\nu)^n \sim (\alpha \cdot h\nu)^n \quad (2.10)$$

The onset of the electronic band gap can be linearized as follows⁷⁹:

$$\alpha \cdot h\nu = C_1 (h\nu - E_g)^n \quad (2.11)$$

Substituting Eq. 2.11 into Eq. 2.10 we end up in the modified Kubelka-Munk function which reads as:

$$(\alpha \cdot h\nu)^{(1/n)} = C(h\nu - E_g) \quad (2.12)$$

where E_g is the bandgap energy, α is the absorption, $h\nu$ is the incident photon energy, C is a constant and n is the electronic transition dependent exponent.

Depending on which type of transition each time occurs, the exponent n takes the following values.

Transition Type	n
direct, allowed	1/2
direct, forbidden	3/2
indirect, allowed	2
indirect, forbidden	3

Table 2.1 Types of electronic dipole transitions and their corresponding exponent n .

2.4 – Electron Paramagnetic Resonance Spectroscopy (EPR)

By plotting the left part of Eq. 2.12 against the photon energy $h\nu$ the bandgap energy E_g can be extracted by a linear fit at its rise as shown in Fig. 2.13. The crossing point between fit and abscissa will determine the bandgap energy. This representation is called *Tauc Plot*⁸⁰ and it provides quantitative calculation of bandgaps. It should be noted that an ideal material with no imperfections would have a step-function like plot and as a result the bandgap in the Tauc plot would be measured precisely. An actual material contains impurities, surface defects things that alter their structure and as a result the spectrum by introducing bends in the ideal step-function like line. For precise calculation of the bandgap, the fitted line must always pass through the middle of the experimental line as shown in Fig. 2.13.

A misuse of the Tauc Plot to determine the bandgap energy of the semiconductors may lead to erroneous estimates especially in the case of modified semiconductors. *Makula et al* addressed the aforementioned issue and proposed the correct way to determine the bandgap energy. As shown in Fig. 2.12 an additional linear fit used as an abscissa is applied for the slope below the fundamental absorption. The point where the two lines cross is the bandgap energy of the semiconductor.

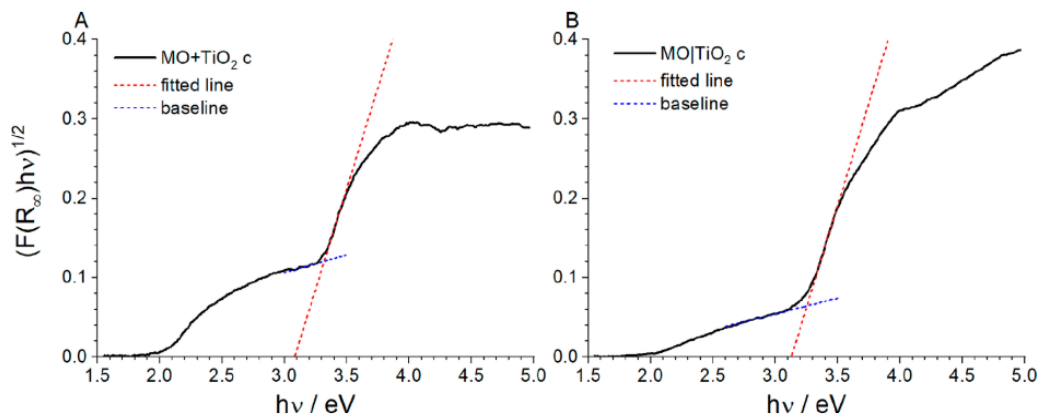


Figure 2.12. Transformed reflectance spectrum plot and the determination of the bandgap energy E_g ⁸¹.

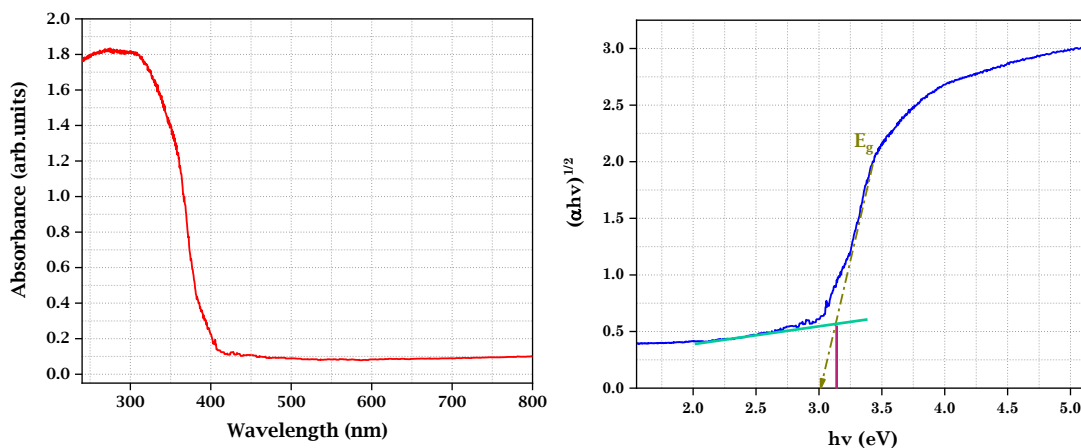


Figure 2.13. Left: Typical Diffuse Reflectance Spectrum of TiO_2 nanoparticles. Right: Typical Tauc Plot of TiO_2 nanoparticles.

2.3.3 - DRS Experimental Set Up (Dept. of Physics UOI)

DRS experiments were conducted using a Perkin Elmer Lambda 35 spectrophotometer. The spectrophotometer uses one halogen lamp and one deuterium lamp to cover the wavelength range from 190 to 1100 nm. The switch from the halogen lamp to the deuterium lamp occurs at around 380 nm. The beam path is shown in Fig. 2.14. The procedure starts with the measurement of the standard reference sample in order to perform autozero. Barium sulfate (Riedel-de Haën 11432) is used due to its high absolute reflectance ranging from 0.973 to 0.988. After performing autozero, the sample to be measured is placed on the DRS holder and the measurement starts. As discussed before, all the samples to be measured must be packed carefully in order to have a smooth surface. After the measurement is taken the spectrum and the data are processed by a software.



Figure 2.14. (Left): Perkin Elmer Lambda 35 spectrophotometer. (Right): Beam path inside the DRS.

2.4 - Electron Paramagnetic Resonance Spectroscopy (EPR)

Electron Paramagnetic Resonance Spectroscopy (EPR) is a technique based on the absorption of electromagnetic radiation, which is usually in the microwave frequency region, by a paramagnetic sample placed on a magnetic field. Paramagnetic species (species that have unpaired electrons) like free radicals and transition metal ions can be identified in solids and liquids and gases as well as defects can be studied.

2.4.1 - EPR Basic Principles

The electron possesses an intrinsic angular momentum; the spin. Electron is a spin $S = 1/2$ particle and in the quantum mechanical description the electron spin can be in two states $m_s = +1/2$ and $m_s = -1/2$. These two states, which are the projection of the electron spin, differ only in the orientation of the angular momentum in space and not in the magnitude. Postulate of quantum mechanics states that definite components of the spin can be determined only in a specific axis. This means that the two spin states can be in only one axis usually around z-axis. At the absence of interactions between the electron spin with its environment, any choice for the direction in space of the z-axis is allowed. The electrons spin randomly, and the two states have the same energy; they are degenerate⁸².

The electron spin angular momentum is associated with the magnetic moment by the formula:

$$\boldsymbol{\mu}_e = g\mu_B\mathbf{S} \quad (2.13)$$

where μ_B is Bohr's magneton and g is the Lande factor or simply the g-factor. The energy of a magnetic moment when a constant magnetic field is applied is given by the scalar product between the magnetic moment $\boldsymbol{\mu}_e$ and the magnetic field \mathbf{B} . Spin comes along the z-axis as discussed earlier and therefore the scalar product reduces to a single term if the magnetic field is applied into z-direction. This reads as:

$$E = -\boldsymbol{\mu}_e \cdot \mathbf{B} = g|\mu_B|\mathbf{S} \cdot \mathbf{B} = g|\mu_B|B_0S_z \quad (2.14)$$

Since spin (S_z) has two states $m_s = +1/2$ and $m_s = -1/2$ by substituting in Eq. 2.14 we take the following expression:

$$E_{\pm} = \pm \left(\frac{1}{2}\right) g|\mu_B|B_0 \quad (2.15)$$

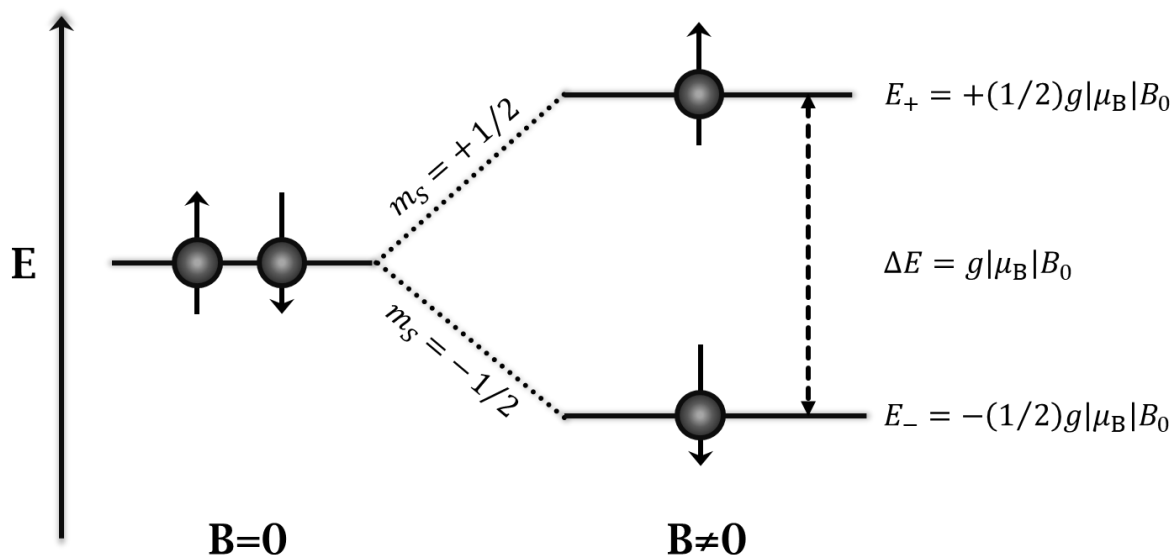


Figure 2.15. The Zeeman effect. At zero field ($B=0$) the spin states have the same energy. Application of static magnetic field ($B \neq 0$) leads to separation of the two states one with high energy when the magnetic moment is aligned with the magnetic field and one with low energy when the magnetic moment is aligned against the magnetic field.

The splitting of the electron spin energy levels into two levels in the presence of magnetic field is called the Zeeman effect⁸³. The energy difference between the two states is⁸⁴:

$$\Delta E = h\nu = g|\mu_B|B_0\Delta m_s = g|\mu_B|B_0 \quad (2.16)$$

It is apparent from Eq. 2.16 that without a magnetic field there is no energy difference to measure. Another thing to mention is that the energy difference depends linearly on the magnetic field.

There are two different ways in order to obtain an EPR spectrum. As shown in Eq. 2.16 we could either keep the frequency of the electromagnetic radiation constant and scan the magnetic field or we can keep the value of the magnetic field fixed and scan the frequency. Most EPR spectrometers operate at a constant frequency in the range of microwaves and scan the magnetic field. Absorption of energy occurs when the magnetic field “tunes” the spin states so that the energy difference matches the energy of the applied radiation. The spectrum is plotted as the first derivative of the absorption versus the magnetic field.

The parameter used as a fingerprint for each molecule would be the g -factor since it's the only factor that can remain constant at different frequencies and magnetic fields. It helps distinguish and identify types of samples. A useful expression is the following:

$$g = \frac{h\nu}{\mu_B B_0} = 714.5 \frac{\nu(\text{Ghz})}{B_0(\text{Gauss})} \quad (2.17)$$

2.4.1 – EPR Basic Principles

So far, we have only discussed for one molecule, in a fixed orientation. Since molecules are oriented in space, mixing them would make the analysis direction dependent. This is expressed in observable parameters with the anisotropy of the g -factor. With the term anisotropic, we refer to the different g -values due to the molecule's orientation relative to the external magnetic field. The g -factor has a set of principal axis system labeled as g_x , g_y and g_z . Depending on the values of the g -factor we have different line shapes in an EPR spectrum as shown in Fig. 2.16.

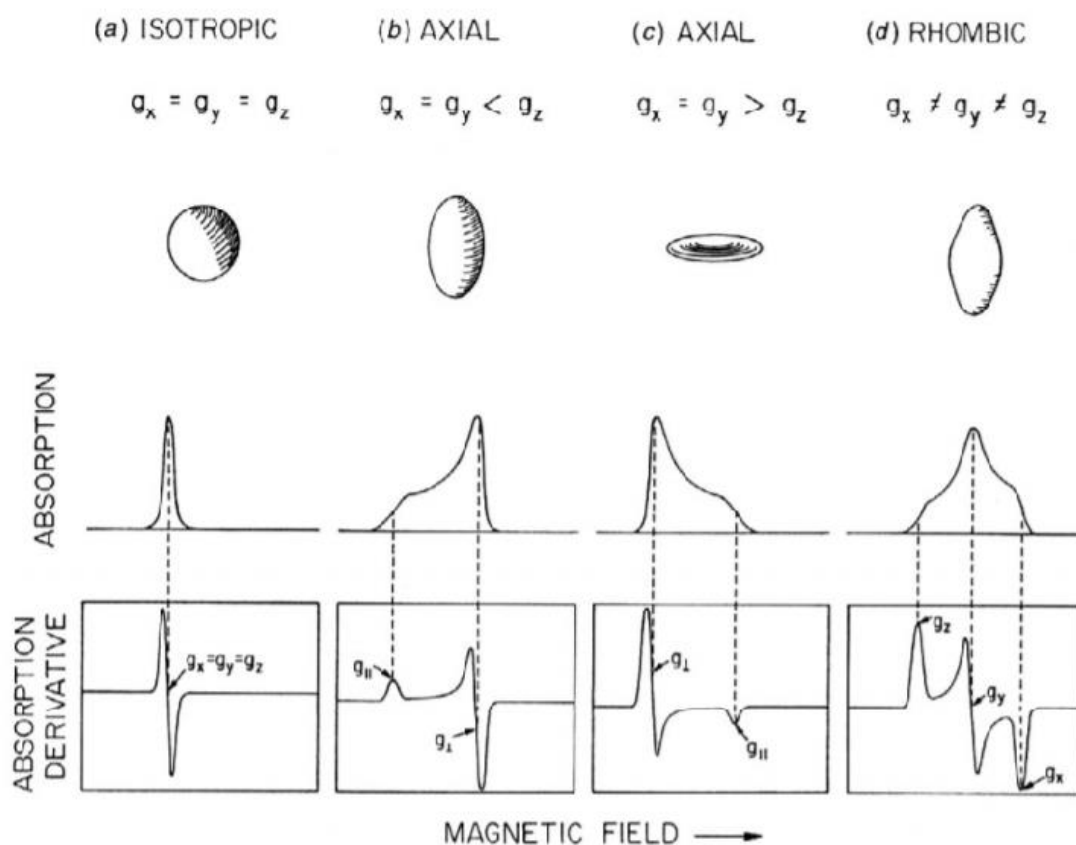


Figure 2.16. Schematic representation of g -tensor and the corresponding absorption and EPR spectra. Depending on the g -values we have different classes of anisotropy. Equal g -values in 3 directions results in isotropic g -tensor (a). An axial class has one component different than the others (b,c). The rhombic class has g -tensor with different components in 3 directions (d)⁸⁵.

As shown in Fig. 2.16 anisotropy is responsible for the lineshape in an EPR spectrum. Starting from the isotropic case where only dipolar interactions are considered the absorption spectrum follows a Gaussian distribution. As we progress to higher order perturbation theory and more interactions are added like exchange interactions the isotropic spectrum begins to deviate and the absorption line takes the form of a Lorentzian distribution.

2.4.2 – Spin Trapping in EPR

A typical EPR spectrum of a powder sample is shown in Fig. 2.17. For the electron-hole separation the sample is illuminated with an arc Xenon lamp.

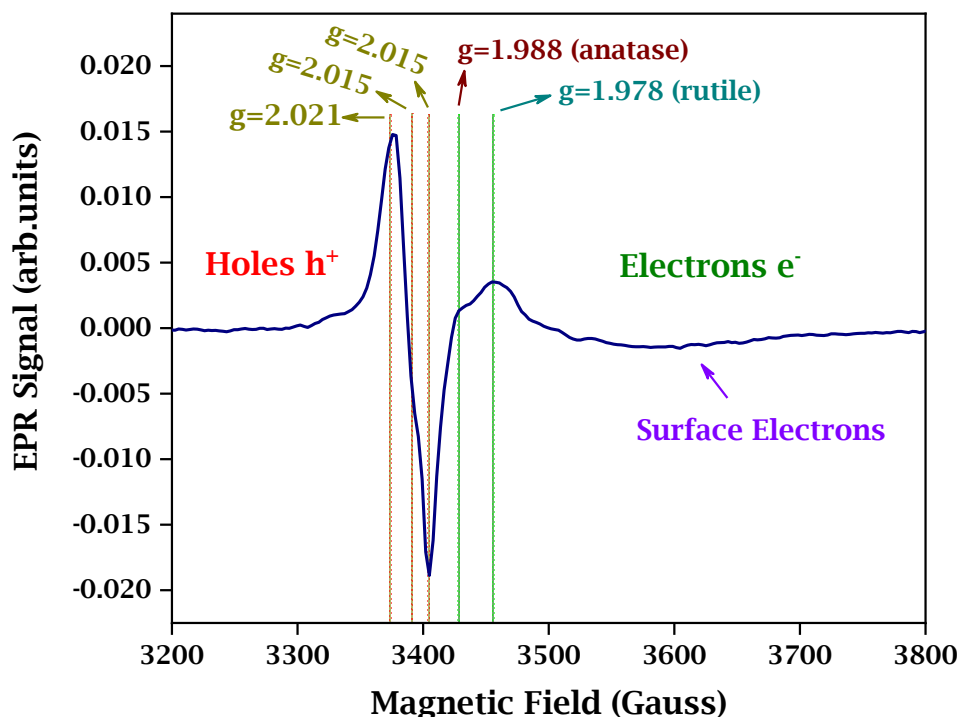
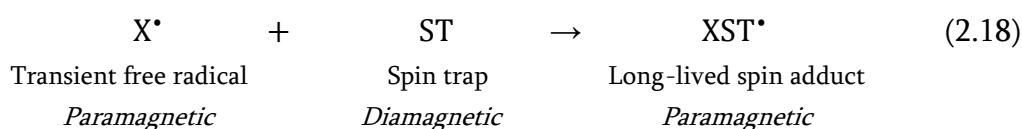


Figure 2.17. Typical EPR spectrum of TiO₂ nanoparticles with the corresponding g-values for electrons and holes. The interactions have effect on the spectrum and we can see the difference from an isotropic signal.

Just like any other spectroscopy, the area under the spectrum can be used for quantification of the signals. The quantification is done using some spin standards. The area of the measured spectrum is compared with the measured area of a spin standard with a known concentration and in this way the concentration of the signal of interest is determined. For radicals the spin standard used is 2,2-diphenyl-1-picrylhydrazyl (DPPH) whereas for spin 1/2 systems the spin standard is copper nitrate. In an EPR spectrum the area under the absorption spectrum is a direct measurement of the concentration of the unpaired electrons. Since the EPR spectrum is the first derivative of the absorption spectra, we have to integrate twice to obtain the correct area. Some signals are difficult to quantify due their broad shape or due to non-flat baselines.

2.4.2 - Spin Trapping in EPR

EPR is the technique of choice when it comes to the study of free radicals. The direct detection of free radicals is usually not possible due to their high reactivity and their transient nature. In this case, spin trapping is used. Spin trapping involves the addition to the system under consideration of a small amount of diamagnetic molecule, usually a nitron or nitroso compound, which reacts with a free radical to produce a more stable paramagnetic radical species that can reach EPR detectable levels. The observable radical species is called spin adduct and the molecule undergoing radical addition is a spin trap. The spin trapping process is schematized in Eq. 2.18.



The most used spin trap is the 5,5-dimethyl-1-pyrroline N-oxide (DMPO) and the α -phenyl-N-t-butyl nitron (PBN). A typical spin trapping EPR spectrum is shown in Fig. 2.18.

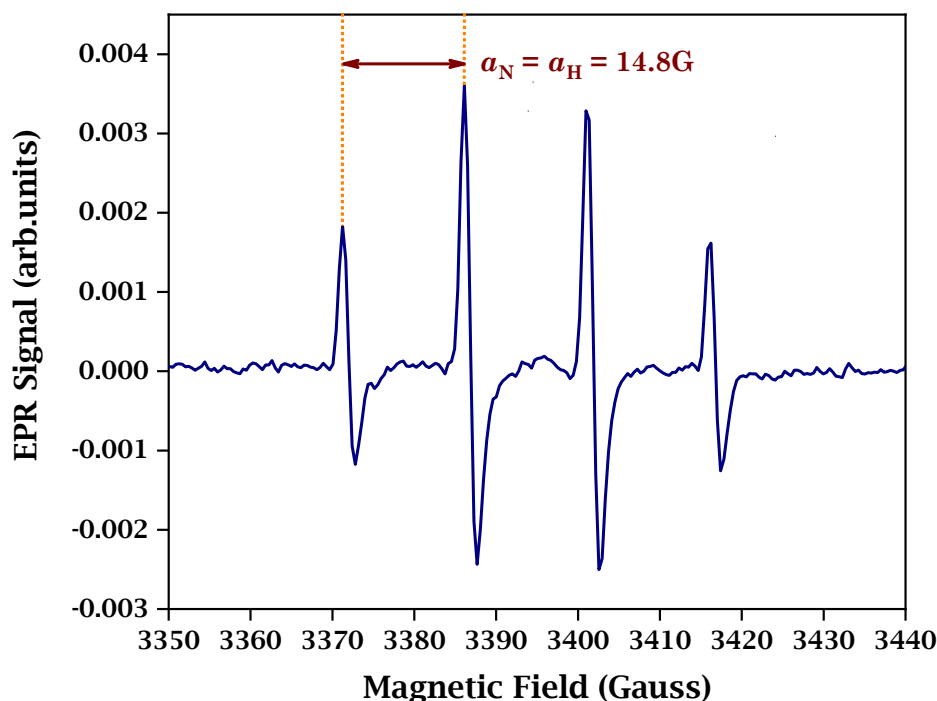


Figure 2.18. Typical EPR spectrum of DMPO-OH spin adduct on TiO₂ nanoparticles. The hyperfine coupling constants are used to determine the spin adduct.

By determination of the parameters such as hyperfine coupling constant and split between peaks we are able to determine the type of radical trapped. The hyperfine coupling constants for the DMPO-OH adduct are⁸⁶ $\alpha_N = \alpha_H = 14.8$ Gauss.

2.4.3 - EPR Experimental Set-Up (Dept. of Physics UOI)

The basic components of an EPR spectrometer are the microwave bridge and the EPR magnet. Starting from the microwave bridge, the most used microwave bridge would be the X-Band microwave bridge operating at around 9.6 GHz. From Eq. 2.17 it is apparent that $g=2$ comes for a field of resonance of 3380 Gauss. The microwave bridge houses the source and the detector. The microwaves are produced in the source as shown in Fig. 2.19 and pass through a variable attenuator. The attenuator controls the flow of microwave radiation and thus we can precisely tune the microwave power.

Most EPR spectrometers are reflection spectrometers meaning that they detect reflected radiation from the microwave cavity which is a metal box where the sample is placed. This happens with the circulator. The circulator guides the microwaves with the aid of waveguides towards the cavity. The microwaves are coupled into the cavity via the iris which tunes the amount of radiation being reflected back by matching the impedances of the waveguide and the cavity. The reflected radiation passes from the circulator and is guided to the detector. Any remaining radiation that reflects back from the detector is forced by the circulator into the upward waveguide and the radiation is converted into heat. The detector measures DC current. The DC current is transformed into AC with a lock-in amplifier thus producing the EPR signal.

These properties give rise to an EPR signal in the following way. The cavity in general stores microwave energy and thus at resonance frequency no microwaves will be reflected back but will remain inside the cavity. When the sample absorbs the microwave energy the impedance in the cavity changes and thus the cavity is no longer coupled, and the microwaves will be reflected back to the bridge resulting in the corresponding EPR signal.

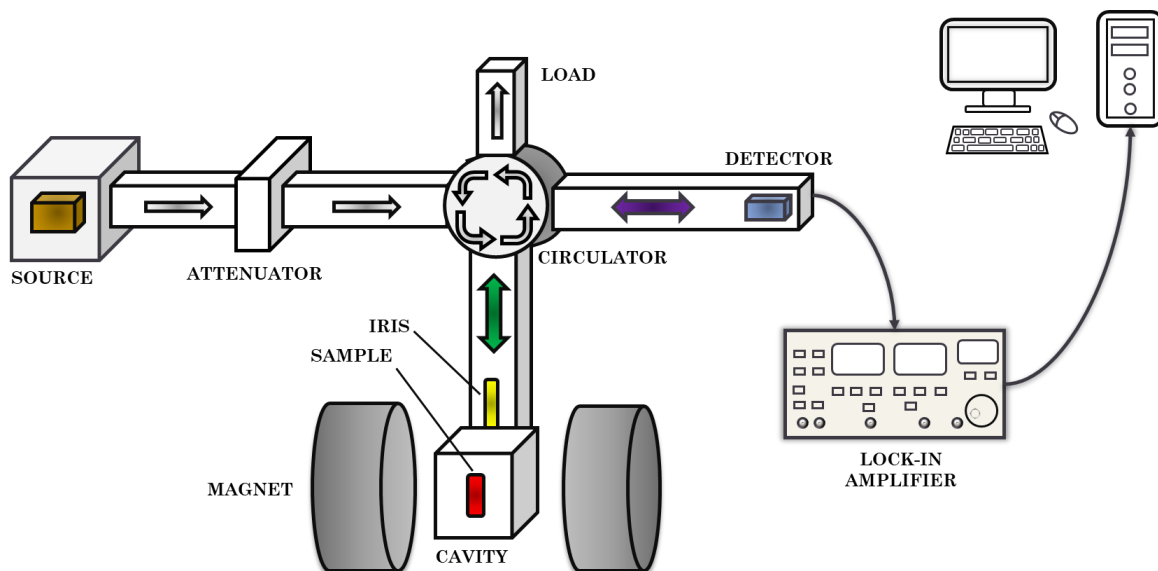


Figure 2.19. Schematic representation of an EPR spectrometer.

2.4.3 – EPR Experimental Set-Up

EPR experiments are conducted on various temperatures ranging from that of liquid helium (4.2K), liquid nitrogen (77K), room (RT) up to high (1200 K) temperature.

The EPR experiments were carried out using a Bruker ER 200D spectrometer with a Bruker X-Band microwave bridge operating in the region of 9-10 GHz. Samples for electron-hole studies were placed in quartz tubes of 5mm, degassed and placed inside the dewar at liquid nitrogen temperature (77K). For the spin trapping experiments the samples were placed with the aid of a syringe into 2 capillaries and then placed in quartz tubes of 5mm inside the dewar at room temperature (RT). The samples were illuminated using an Oriel 6293 Arc Xenon Lamp with a maximum output of 800W. The microwave power was controlled with a microwave controller and the magnetic field with a field controller. The EPR spectra were recorded and processed using Lab-View software.

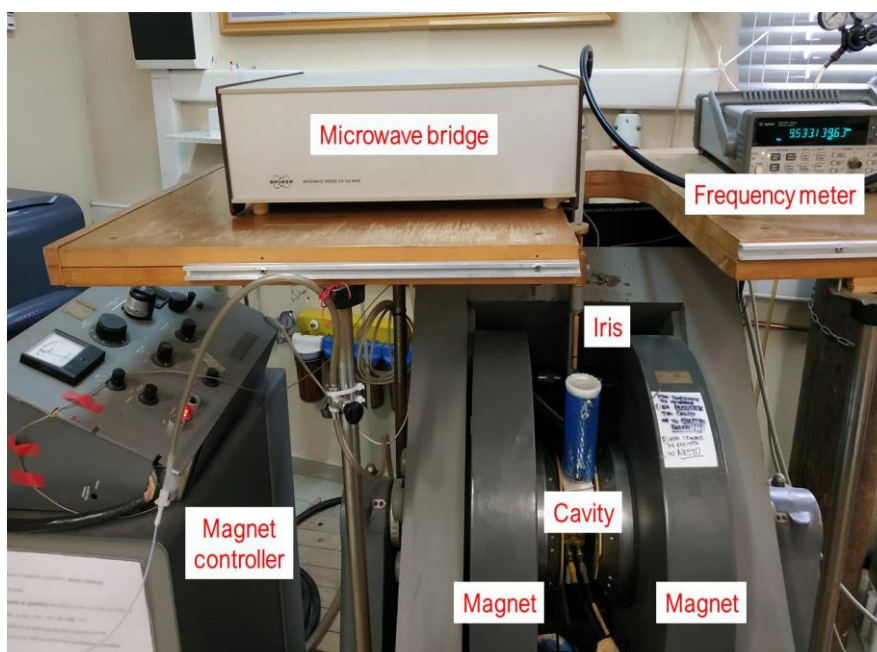


Figure 2.20. Bruker ER 200D spectrometer with its components noted.

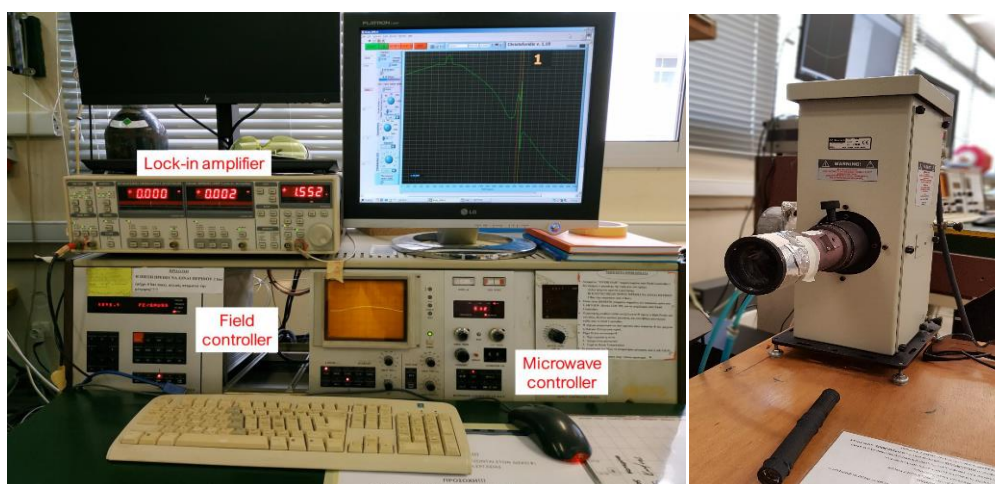


Figure 2.21. (Left): Microwave and field controller, lock-in amplifier. (Right): Oriel 6293 Arc Xenon Lamp.

2.5 - Furnace for Calcination (Dept. of Physics UOI)

The samples were calcined either for better crystallization or for surface modification using a Thermansys 30802 tubular furnace as shown in Fig. 2.22. The nanopowders were placed in ceramic capsules and then inserted at the center of the tubular furnace. The two edges of the tube were sealed using a rubber gasket and metallic seals to ensure calcination under the desired atmosphere. The calcinations were performed under inert atmospheres using nitrogen N_2 gas (Linde, purity >99.9%) or carbon-rich atmospheres using methane CH_4 (Linde, purity >99.5%). All the calcinations parameters including temperature, temperature gradient during heat up and cooldown, calcination duration were set using appropriate software while the gas flow was controlled with a rotameter. The metallic seals are water-cooled, and the tube is made of alumina.



Figure 2.22. Thermansys 30802 tubular furnace used for calcination of samples.

2.6 – X-Ray Photoelectron Spectroscopy (XPS)

X-Ray Photoelectron Spectroscopy (XPS) is a surface-sensitive spectroscopic technique, that can identify the elemental composition and the nature of the elemental bonding that exists at the surface of a material. The basis of this spectroscopic technique is the photoelectric effect⁸⁷, in which the sample under investigation is bombarded with a beam of X-rays while simultaneously measuring the kinetic energy of electrons that are emitted from the outer shell of the material. XPS was developed in the 1960's by Kai Siegbahn⁸⁸ and has since become a powerful spectroscopic technique used for surface analysis and investigation of the efficacy of surface engineering.

2.6.1 – XPS Basic Principles

The basis of the XPS is the photoelectric effect. As outlined in Fig. 2.23, when radiation of known energy usually X-rays is absorbed by an atom or a molecule, an electron can be ejected. The kinetic energy of the ejected electron depends upon the incident photon energy ($h\nu$), and the binding energy (E_b) that is the energy required to remove the electron from the surface.

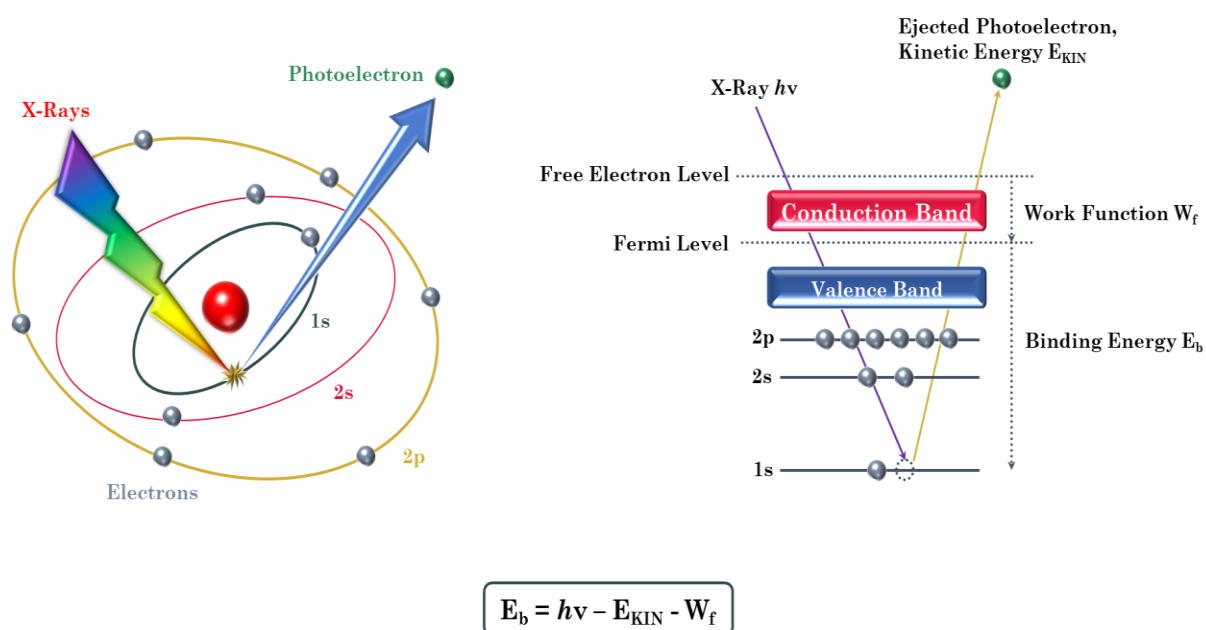


Figure 2.23. The photoelectric effect involved in XPS analysis.

By measuring the kinetic energy of the ejected electrons, it is possible to determine which electrons are near a material's surface as well as the binding energy of the electron.

2.6.1 –XPS Basic Principles

The binding energy is characteristic for each element and depends on the orbital from which the electron was ejected as well as the chemical environment of the atom from which the electron was emitted. XPS only identifies photoelectrons that reach the detector, the elemental signals from the surface are much stronger than those from deeper in the sample. Therefore, the emitted photoelectrons originate from atomic layers close to the surface.

High vacuum conditions must be fulfilled in XPS experiments of about 10^{-9} - 10^{-10} Torr. High vacuum facilitates photoelectron transport to the analyzer and also prevents recontamination of clean samples.

The spectrum is plotted as a function of binding energy. The position of a peak relatively to the binding energy can give information about elemental and chemical composition of the surface. The spectrum usually exhibits a doublet peak structure as shown in Fig. 2.24, which is a result of spin-orbit coupling. Furthermore, chemical shift in peaks is strongly influenced by the oxidation state of the atom as well as the local physicochemical environment. Atoms with higher positive oxidation state exhibit a higher binding energy due to the extra coulombic interaction. The XPS spectrum can give information about the content of the surface quantitatively by integrating the peaks of the signal.

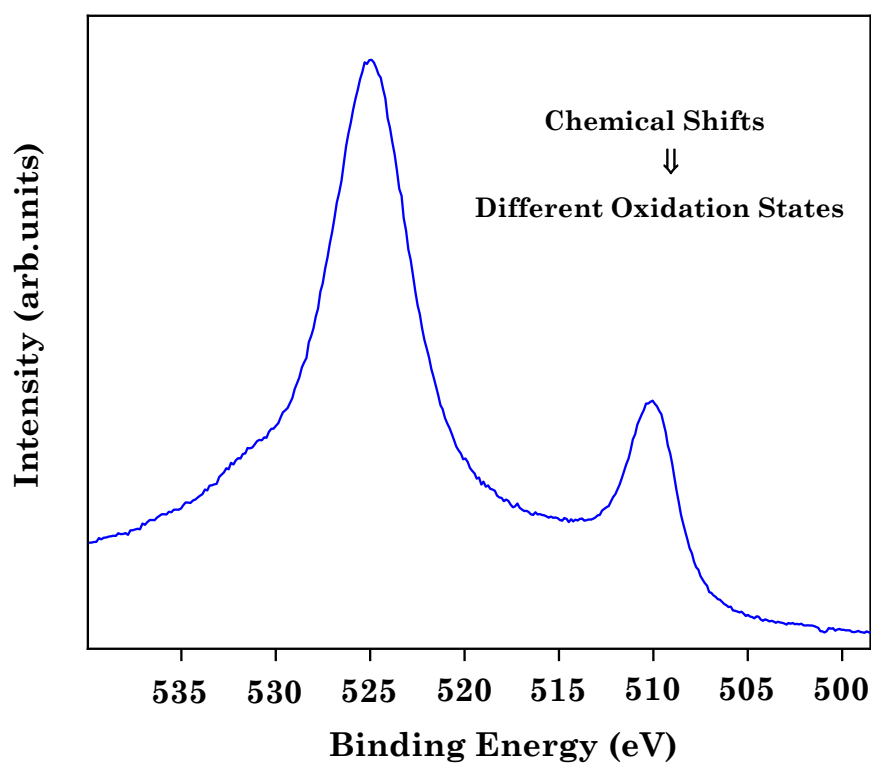


Figure 2.24. Typical XPS spectrum showing the doublet peak structure.

2.6.2 – XPS Experimental Set – Up (Dept. of Physics UOI)

The basic components of an XPS spectrometer are the source, the ultra-high vacuum system, and the analyzer-detector. Starting from the source, where a filament is heated, and then high energy electrons are directed towards a metallic target. The most commonly used X-ray sources are the Mg K_α radiation and the Al K_α radiation with incident energies of 1253.6 eV and 1486.6 eV respectively. In some cases, the source can house dual anode that enables the switch between two different energies for experimental optimization. The incident radiation is monochromated using a quartz crystal and then is directed to the sample.

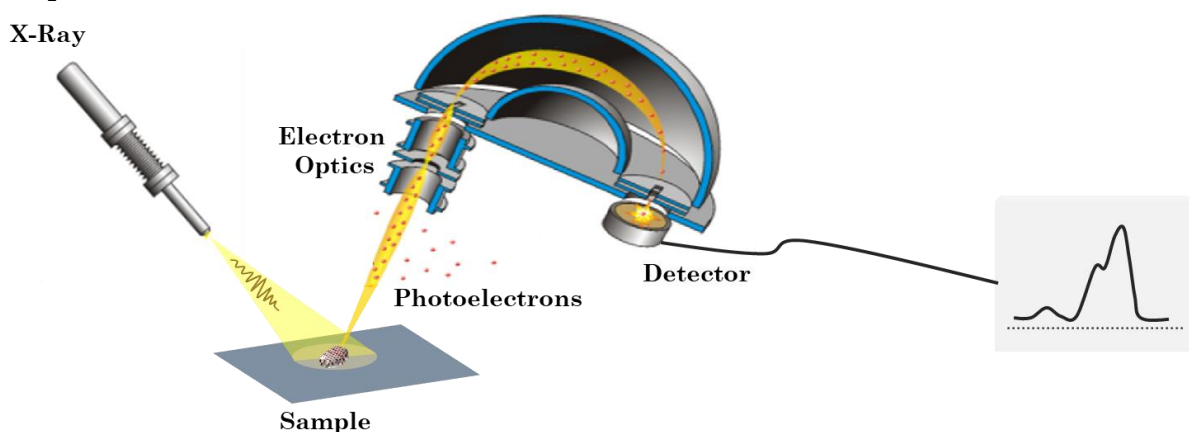


Figure 2.25. Schematic representation of an XPS spectrometer.

Upon sample irradiation, the photoelectrons are focused into a hemispherical analyzer by an electrostatic lens system. The hemispherical analyzer is an electrostatic device that disperses electrons as a function of their kinetic energy, in analogy with a prism which disperses light depending on its wavelength. At the end of the analyzer, the detector is attached which counts electrons. By scanning the range of binding energies, the spectrum is recorded. The entire source-analyzer system is enclosed in a high vacuum chamber which utilizes high vacuum pumps to ensure longer photoelectron path length and non-contaminated samples.

X-ray photoelectron spectrum were recorded in a surface analysis ultrahigh vacuum system (SPECS GmbH) equipped with a twin Al-Mg anode X-ray source, and a multichannel hemispherical electron analyzer (HSA-Phoibos 100). The pass-energy was 30 eV, providing a line-width of 1.18 eV. Spectral analysis included a Shirley background subtraction and fitting with a minimum number of peaks. The profile of the peaks was taken as a convolution of Gaussian and Lorentzian functions, using the least-squares curve fitting program WinSpec.

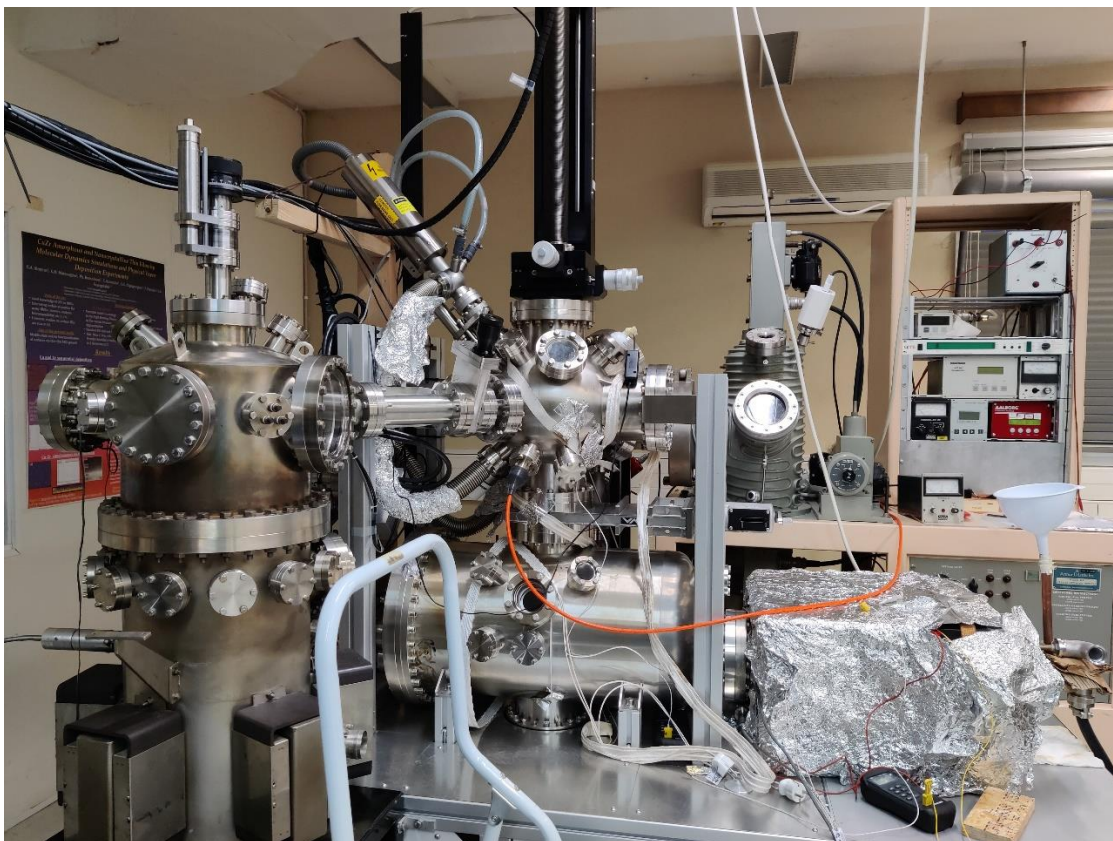


Figure 2.26. XPS experimental setup.

2.7 – Brunauer – Emmett – Teller (BET) Analysis

The BET method (abbreviated from Brunauer-Emmett-Teller theory) is the most widely used procedure for the determination of the surface area of solid or porous materials. BET analysis provides important information concerning the materials physical structure as the surface affects how the solid will interact with its environment. It was proposed by Brunauer, Emmett and Teller in 1938⁸⁹ and is an extension of the Langmuir theory which is a theory of monolayer adsorption to multilayer adsorption.

2.7.1 – BET Basic Principles

BET measures surface area based on gas adsorption. The specific surface area of a particle is determined at an atomic level by adsorption of an unreactive gas usually nitrogen (N_2). In order to prevent interaction between the solid and the gas, the procedure is done at cryogenic temperatures. The temperature at the solid is kept constant under isothermal conditions, whereas the pressure of the adsorbing gas is increased. As the relative pressure

2.7.1 – BET Basic Principles

is increased, more and more molecules adsorb on the surface. A thin layer will eventually cover the entire surface. The adsorption isotherm is obtained by measuring the amount of gas adsorbed across a wide range of relative pressure at a constant temperature (typically liquid N₂ at 77 K). Conversely, desorption isotherms are achieved by measuring gas removed as pressure is reduced.

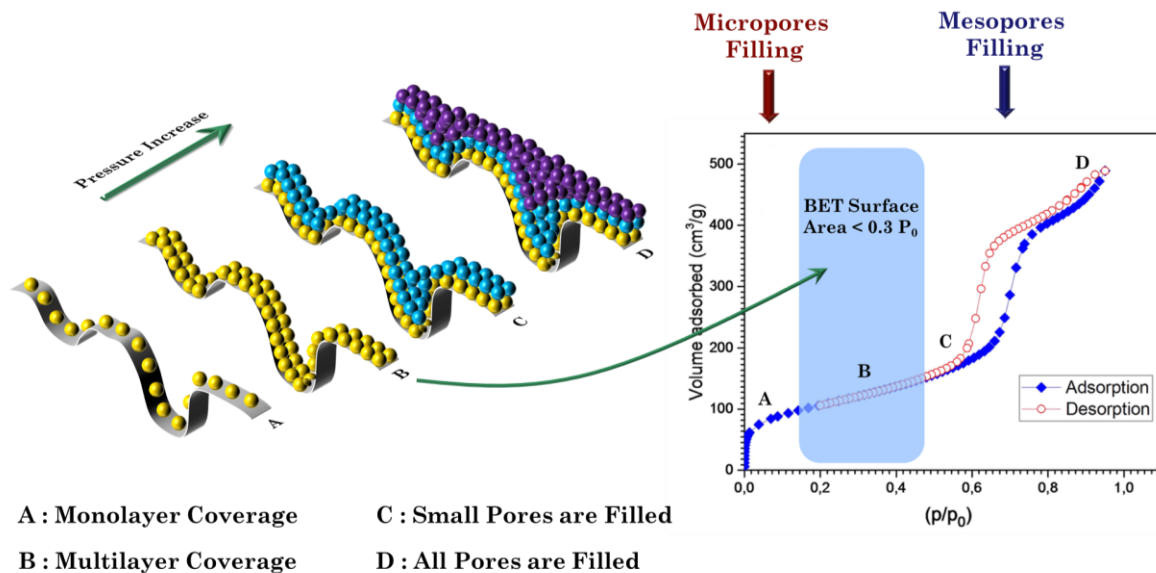


Figure 2.27. Adsorption and Desorption process as a function of pressure. Layer coverage is also noted.

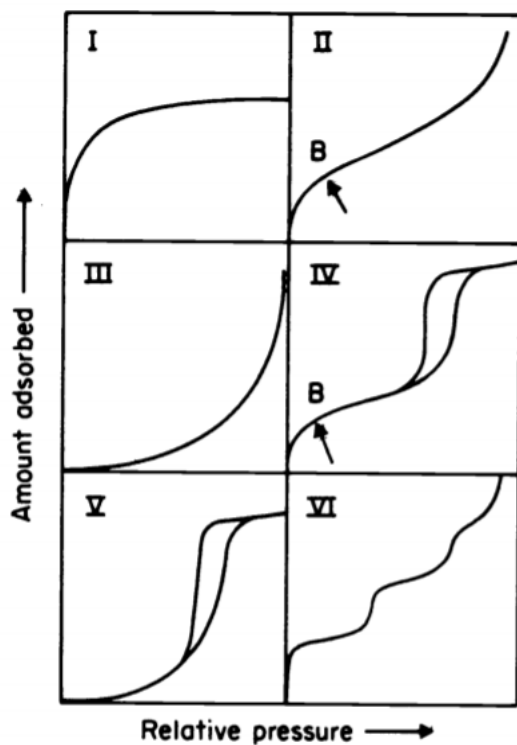


Figure 2.28. Type of isotherms in BET theory.

The shape of the sorption isotherms is strongly influenced by the pore width which are classified as follows⁹⁰; *Micropores* : pores with internal width less than 2 nm; *Mesopores* : pores of internal width between 2 and 50 nm; *Macropores* : pores of internal width greater than 50 nm. The surface area is determined using the BET equation:

$$\frac{1}{W\left(\left(\frac{P}{P_0}\right)-1\right)} = \frac{1}{W_m C} + \frac{C-1}{(W_m C)} \left(\frac{P}{P_0}\right) \quad (2.19)$$

where W is the weight of gas adsorbed at relative pressure P/P_0 , W_m is the weight of adsorbate constituting a monolayer of surface coverage. The C constant is related to the magnitude of the adsorbent / adsorbate interactions.

2.7.2 – BET Experimental Set-Up

The type of isotherms⁹¹ is summarized in Fig. 2.28. Type I isotherms are obtained when adsorption is limited to only a few molecular layers. Type II isotherms are typically obtained in the case of non-porous or microporous adsorbent. Point B indicates at which stage monolayer coverage is complete and multilayer adsorption begins to occur. The reversible Type III isotherm is obtained when $C < 1$ and shows the formation of a multilayer. The adsorbate-adsorbent interactions are relatively weak. Type IV isotherms are typical for mesoporous materials. In these isotherms the hysteresis loop should be noted which is a result of pore condensation. The limiting uptake over a range of high P/P_0 indicates complete pore filling. Type V isotherms shows hysteresis and pore condensation just like Type IV, but the initial part is similar to Type III indicating relatively weak interactions between the adsorbent and the adsorbate. Type VI is a special case which represents stepwise multilayer adsorption on a uniform, non-porous surface.

2.7.2 – BET Experimental Set – Up (Dept. of Physics UOI)

Prior to any measurement, the sample must be preconditioned to remove physically bonded impurities from the surface of the powder in a process called degassing. Samples are usually degassed either at vacuum conditions or with continuously flowing inert gas like N_2 at elevated temperatures. The temperature of the degassing process as well as the duration are carefully chosen to avoid structural changes on the sample.

Once the degassing process is completed, the powders are ready for measurement. The samples are inserted to the analysis port. Dewars of liquid nitrogen are used to ensure constant temperature during the measurement. The adsorbate usually liquid nitrogen is injected in the sample cell with a calibrated piston for the adsorption measurement and is evacuated for the desorption measurement. BET analysis must be done in the linear region of the BET plot.



Figure 2.29. Quantachrome NOVAtouch LX2.

BET measurement were carried out using a Quantachrome NOVAtouch LX2 BET surface area and pore analyzer with a dedicated P_0 station and four sample degassing ports. The analysis of the isotherms and factors like degassing duration and temperature as well as BET related factors were controlled with Quantachrome TouchWin software.

2.8 Flame Spray Pyrolysis (FSP)

Flame Spray Pyrolysis (FSP) is a versatile one-step continuous process for the production of nanopowders^{66,67} at a high rate⁹² with controlled-particle characteristics⁶⁸. It consists of the spray pyrolysis of a liquid precursor, under a heat treatment from a flame. The combustion of the spray converts the liquid precursors into nano-sized metal or metal-oxide particles, depending on the material and the operating conditions. The production of high purity nanopowders with the absence of waste and the proven scalability makes this method a strong contender in the process of nanomaterials production.

2.8.1 Basic Principles of FSP

A typical FSP reactor is generally comprised by the three main parts⁹³: an atomizer, a burner and a collecting system. As shown in Fig. 2.30 the liquid precursor must be atomized into micron-sized droplets.

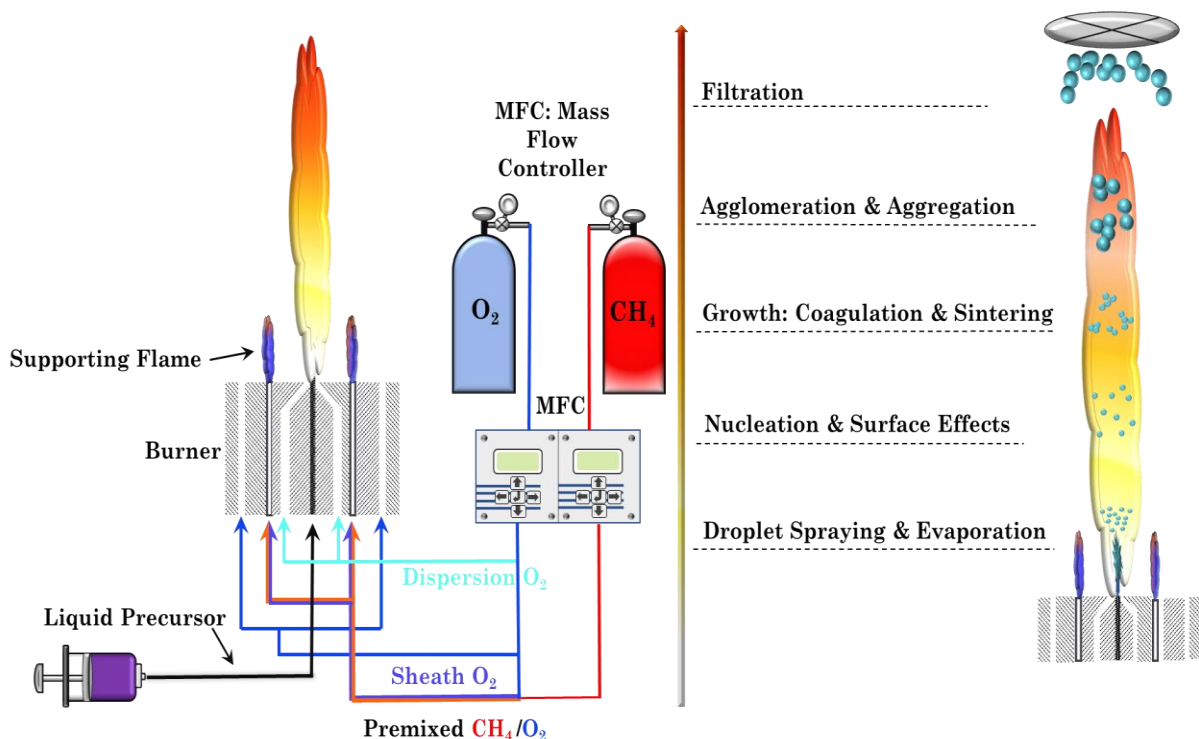


Figure 2.30. Schematic representation of a typical FSP apparatus.

Atomization can be achieved with different techniques like ultrasonic, electrostatic or even air blasts. The droplet size, velocity and rate of atomization are very important for the whole FSP process. The droplet is sprayed on the flame environment at the burner. The burner comes in two types: a diffusion burner where the fuel (CH_4) and the oxidant (O_2)

2.8.1 – Basic Principles of FSP

are not mixed before entering the flame zone, and a premixed burner where the oxidant (O_2) and the fuel (CH_4) are mixed before entering the flame zone. The premixed fuel and oxidant comprise the pilot flame where the dispersion gas (O_2) is responsible for the nebulization angle of the droplet, the conversion of the precursor into micron-sized droplets and acts as an additional oxidant for the flame environment. An additional O_2 gas flow termed sheath O_2 creates an upward stream for protection of the flame environment and assistance in the nanoparticle's collection. The liquid precursor is injected in the flame environment with the form of droplets, the droplets are combusted, and the particles are then collected in a glass fiber filter.

2.8.2 Particle Formation Process

In FSP there are two possible routes leading to particle formation, droplet-to-particle or gas-to-particle. We must clarify at this point that even though the precursor is sprayed in micron-sized droplets into the flame environment, that does not mean that particle formation occurs only through the droplet-to-particle pathway.

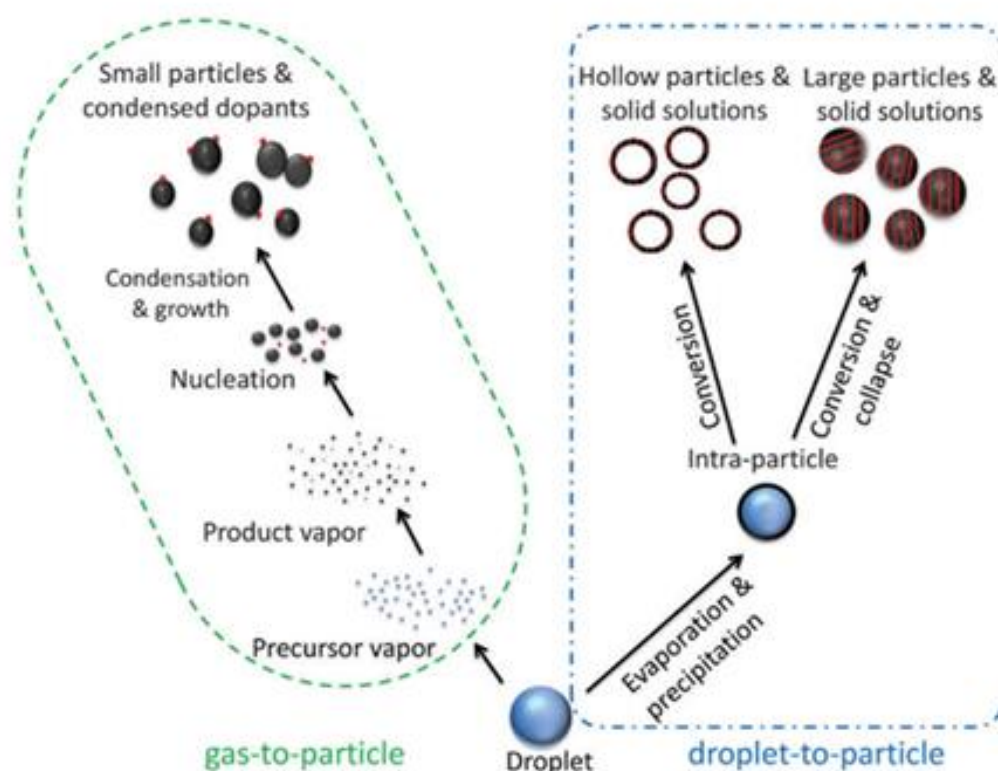


Figure 2.31. Gas-to-particle and droplet-to-particle pathways for particle formation in aerosol synthesis⁷⁰.

2.8.3 – Oxygen-lean (Anoxic) Flame Spray Pyrolysis

In the particle formation process, there are two basic criteria affecting the final product. These are the combustion enthalpy density and the fraction $T_{bp} / T_{d,mp}$. T_{bp} refers to the boiling point of the solvent whereas $T_{d,mp}$ refers to the decomposition point of the metal precursor. It has been found that⁹⁴ high combustion enthalpies ($>4.7 \text{ kJ/g}_{\text{gas}}$) and $T_{bp} / T_{d,mp} >1.05$ lead to homogenous powders. The liquid precursors used are usually metalorganic compounds which account only a small fraction of the total combustion enthalpy. Most of the combustion enthalpy comes from the solvents, where high enthalpy solvents like xylene are used.

In the gas-to-particle route, the $T_{bp} / T_{d,mp} >1.05$ and thus the precursor decomposes before the solvent evaporates. The precursor spray ignites and reacts exothermically resulting in the decomposition of the precursor leaving a metal vapor in the hot flame environment ($\sim 2400^\circ\text{C}$). These conditions lead to the formation of molecular nanoclusters by nucleation. These nanoclusters due to Brownian motion and difference in their velocities collide with each other, resulting in coagulation. Coagulation is the main growth mechanism. During their growth, particles collide and stick together, either retaining their individual shape or fuse together forming a spherical particle. This sintering process is called coalescence. The final particle morphology depends on the temperature profile (cooling rate) and primary particle size and are categorized into single particles, aggregates where the primary particles are connected by strong sinter necks or agglomerates where the primary particles are held together by weak van der Waals bonds. When sintering is faster than coagulation, single particles are formed. When sintering and coagulation are comparable aggregates are formed whereas when sintering is negligible agglomerates are formed⁹⁵.

In the droplet-to-particle route, $T_{bp} / T_{d,mp} <1.05$ thus the solvent evaporates before the decomposition of the precursor thus leaving the precursor into the high temperature zone. The nanoparticle's size depends on the droplet size. The precursor is concentrated on the outer layer of the droplet preventing further vaporization of the solvent. In this case precipitation occurs and if fast enough, a shell is formed outside the droplet and micron-explosion occurs which induces shell-like particles. Other products include micron-sized particles.

2.8.3 Oxygen-lean (Anoxic) Flame Spray Pyrolysis

Flame spray synthesis produces metal-oxide nanoparticles of various metals. A step further would be the production of metal nanoparticles. As shown above, conventional flame spray pyrolysis is conducted without taking into account the atmosphere. While noble metal nanoparticles like Au^0 , Ag^0 , Pt^0 can be obtained in oxygen-rich atmospheres

2.8.3 – Oxygen-lean (Anoxic) Flame Spray Pyrolysis

like ambient air, the production of non-noble metals (more technically important metals) requires atmospheres with low content in oxygen termed reducing or anoxic atmospheres. By the term “reduced metal oxides” we refer to metal oxides at which the metal is at a lower oxidation state than the thermodynamically most stable state at room temperature. Implementation of the reducing conditions could possibly alter the nanoparticles characteristics and growth path. It has been shown that⁹⁶ the anoxic conditions do not affect the physical process of nucleation, growth and aggregation.

In order to achieve the anoxic conditions required, the open-flame FSP apparatus has been modified⁹⁷. The first step is the enclosure of the flame with a sinter metal tube with an inner porous or perforated tube as shown in Fig. 2.32. The second step is to insert an inert gas like nitrogen, helium or argon (N_2 most used). The sinter metal tube with its inner tube creates a radial inflow which protects the flame environment against oxidation. In the nitrogen inner atmosphere, the amount of oxygen accessible for combustion can be limited to the oxygen initially fed to the flame.

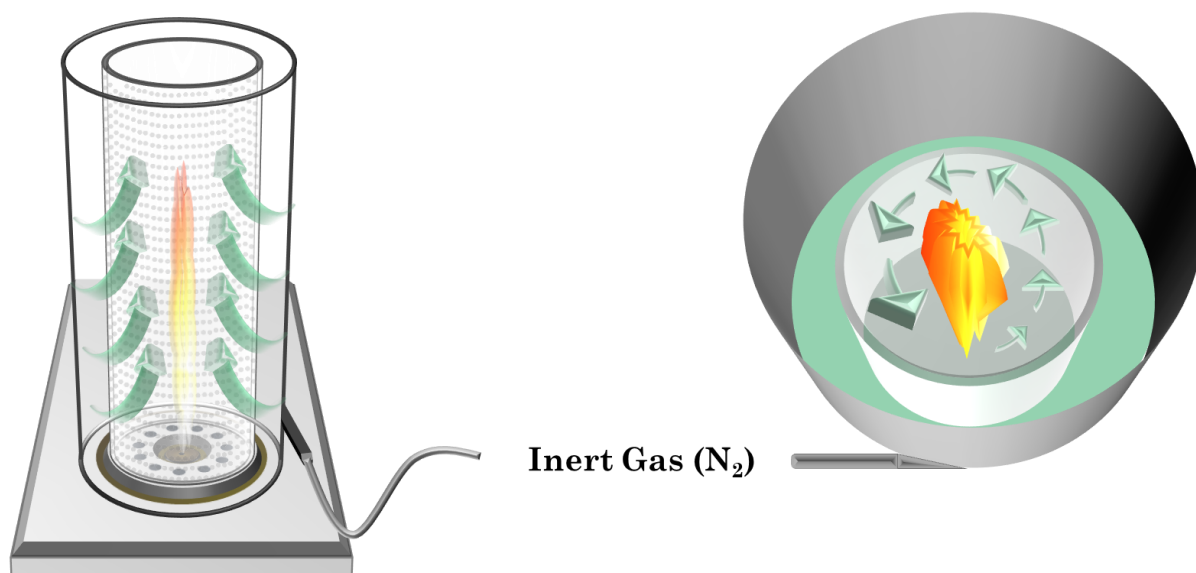


Figure 2.32. Schematic representation of anoxic FSP apparatus.

Controlling the flame atmosphere is detrimental to the final product. At low oxygen concentrations novel phases such as reduced metal oxides can be produced. At very low oxygen concentrations (<100 ppm O_2), oxygen deficiency prevents metal oxidation and as a result metallic nanoparticles are produced⁹⁸. The main parameter affecting the composition of the flame environment atmosphere is the inert gas flow. High N_2 flows tend to create more anoxic conditions. Flame pyrolysis must also be considered. Highly anoxic conditions mean low oxygen concentrations in the burner chamber. If the oxygen initially fed to the system is inadequate for the full combustion of methane, traces of non-combusted carbon may be found in the final product.

2.8.4 Coating in Flame Spray Pyrolysis

The synthesis of nanomaterials in an one step-process can be done using flame spray pyrolysis. Surface functionalization, however, is another process. Surface functionalization can be done either at the nanoparticles surface or with the addition of a shell around the core material. Coating is used for surface functionalization, or for protection against oxidation or leaching. It is apparent that the synthesis and coating of such particles are two distinct processes. Traditional wet chemical methods do not allow the control of the hermeticity and shell thickness and are also multi-step processes. The combination of flame synthesis and particle coating in a single gas-phase process is the “holy grail” in flame aerosol technology. Two possible routes can be followed when it comes to coating in aerosol reactors. The first one is the feed of premixed precursors in the flame, a process which however can only be applied on certain occasions. The operation window is quite challenging since co-oxidation of precursors at high temperatures results in particles with segregated domains⁹⁹. The alternative route is by the separate introduction of precursors to the flame burner. This approach is more favorable for the production of core-shell nanoparticles.

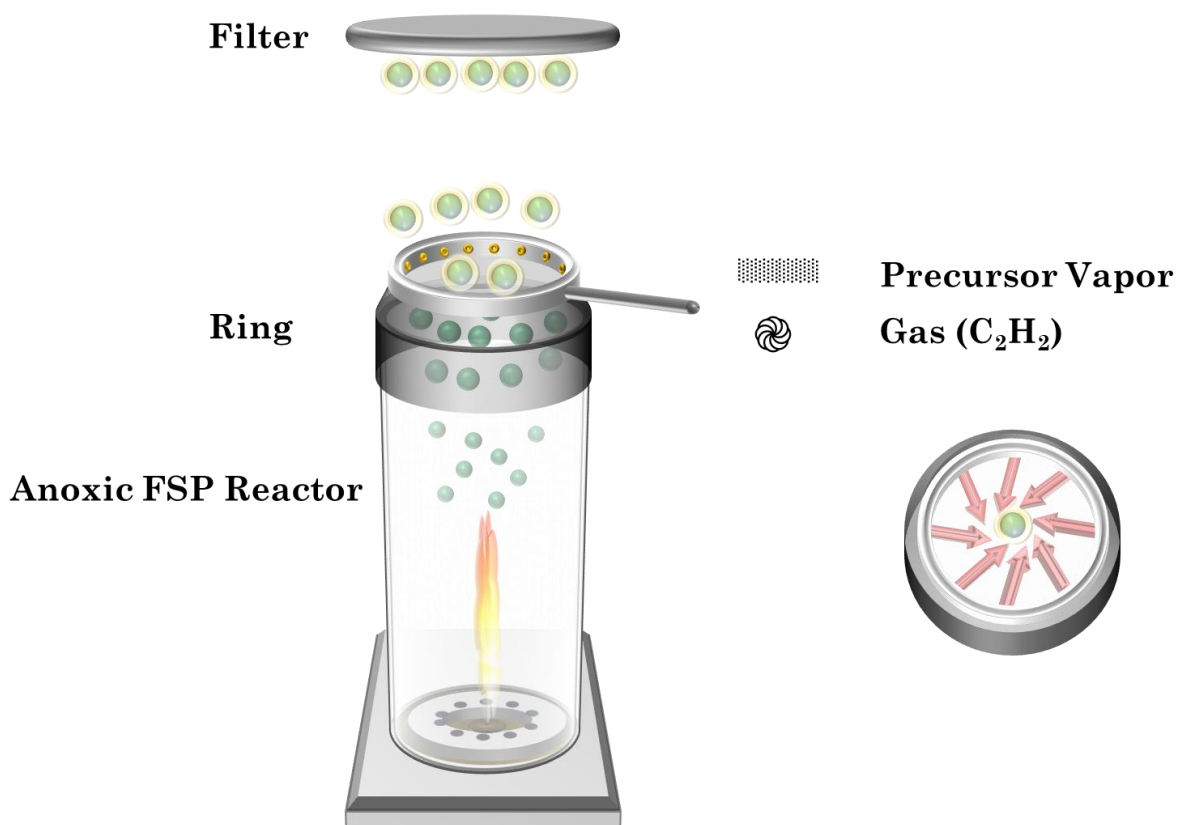


Figure 2.33. Schematic representation of coating FSP apparatus.

2.8.5 – FSP Experimental Set - Up

As shown in Fig. 2.33, the coating setup⁷¹ consists of a metal torus ring placed above the metal-sinter tube. The ring has radially equispaced openings each pointing away from the center line and pointing downstream to ensure no stagnation flow upstream and to create a swirl effect. In case of core-shell $XO_2@YO_2$ nanoparticles at which the core metal oxide is coated with a metal oxide shell, the precursor vapor is supplied to the flame environment with the aid of an inert carrier gas usually nitrogen¹⁰⁰. In the case of carbon-coated nanoparticles, carbon-rich gases like acetylene (C_2H_2) are supplied to the ring and the shell is formed by the pyrolysis of acetylene in the flame environment.

2.8.5 FSP Experimental Set-Up (Dept. Of Physics UOI)

The FSP reactor used for the production of nanomaterials is shown in Fig. 2.34. As discussed above, the FSP reactor comprises of three main parts: an atomizer, a burner and the collection system.

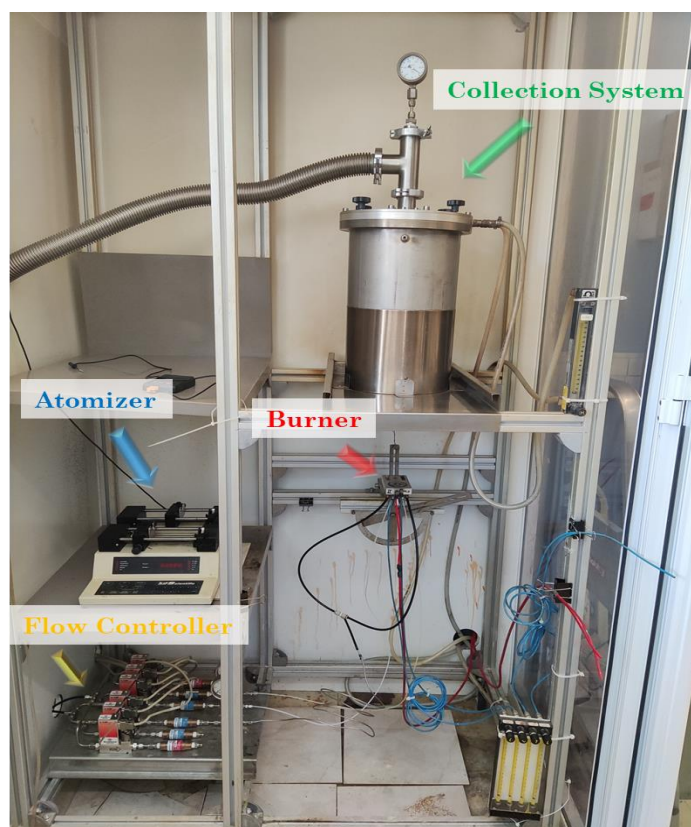


Figure 2.34. FSP reactor with its components noted.

Starting from the basic component of the FSP apparatus the burner, it consists of a gas-assisted nozzle made from a capillary of 0.5mm inner diameter and 0.6mm that lies in an opening of 0.8mm thus creating an annular gap. Oxygen gas is supplied in the annular gap and acts as the dispersion gas, whereas the flamelets are supplied with premixed O_2 and

2.8.5 – FSP Experimental Set - Up

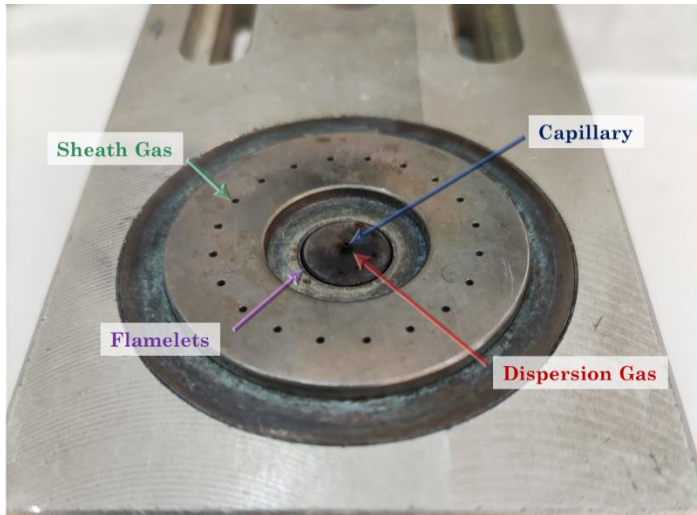


Figure 2.35. FSP burner configuration.

CH₄, comprising the pilot flame. The spray angle is determined by the height of the capillary above the nozzle opening. As shown in Fig. 2.35 and 2.36, the precursor is sprayed into the flame environment after it has been converted into micron-sized droplets with the aid of the dispersion gas. The pilot flame is responsible for the initial ignition and the sheath gas protects the flame environment and facilitates particle collection.

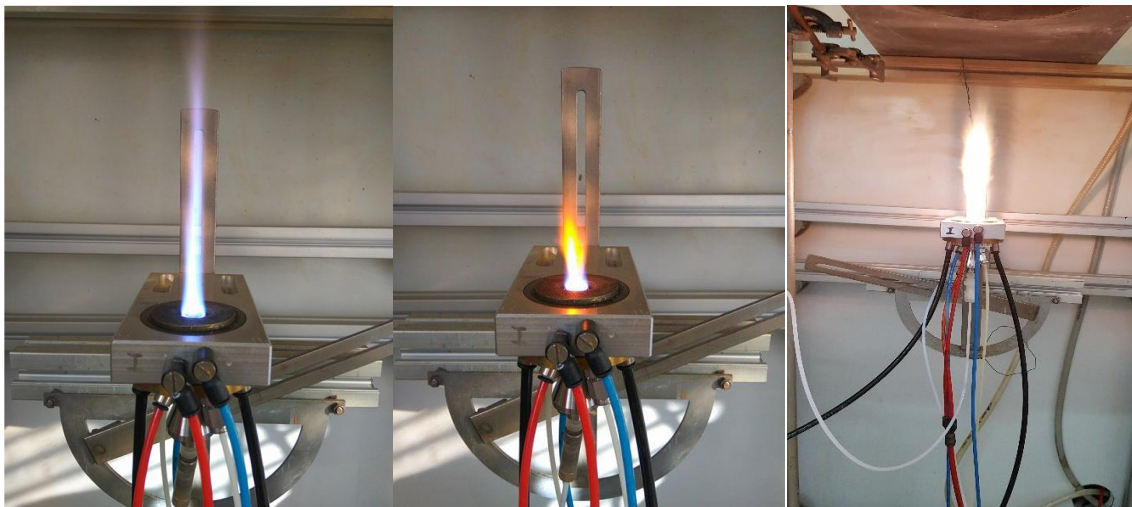


Figure 2.36. (Left): Pilot flame. (Middle): Dispersion. (Right): Precursor combustion.



Figure 2.37. Atomization device. The precursor is converted into micron-sized droplets and sprayed with the aid of a syringe pump.

2.8.5 – FSP Experimental Set - Up



Figure 2.38. Particle collection. Nanopowders are collected in a glass fiber filter.

The precursor is supplied into the form of micron-sized droplets with the aid of a syringe pump (Kd Scientific). Precursor flow rate can be manually adjusted as shown in Fig. 2.37. Particle collection is done in a glass-fiber filter ([Hahnemühle GF6 filter](#)) as shown in Fig. 2.38 with the aid of a vacuum pump.

For the oxygen-lean anoxic FSP configuration, a metal sinter tube was used for the enclosure of the flame environment. Nitrogen was supplied through an inlet to achieve reducing conditions. The inner tube, responsible for the radial inflow is made either porous from Inconel alloy, or perforated from stainless-steel as shown in Fig. 2.39.



Figure 2.39. (Top Left): Metal sinter tube for the anoxic FSP configuration. (Top Right): Porous inner tube. (Bottom): Perforated inner tube.

2.8.5 – FSP Experimental Set - Up

The coating setup is shown in Fig. 2.40. At the top of the metal sinter tube, a metal torus ring was placed with 4.5 cm diameter. The ring has 12 radially equispaced openings with interdistance ID = 0.6 cm each pointing 10° away from the center line and 20° downstream to ensure no stagnation flow upstream. Through these openings, acetylene gas (C_2H_2) was fed to the system. Above the ring a 25 cm quartz tube was placed for controlled pyrolysis of the acetylene.

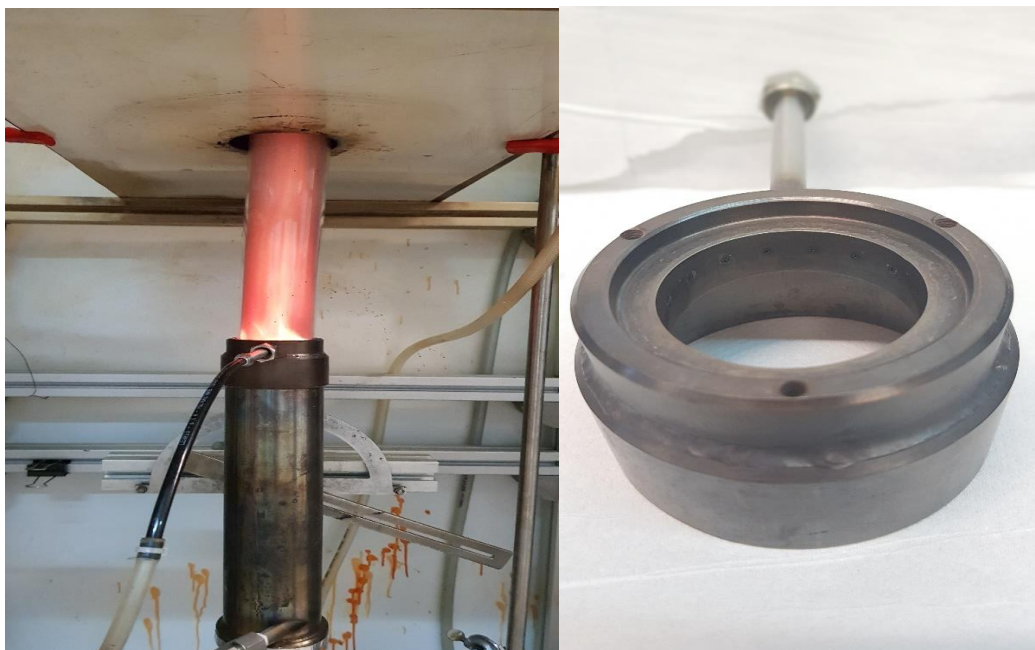


Figure 2.40. (Left): Coating configuration for carbon-coated nanopowders. (Right): The coating ring.

For the synthesis of TiO_2 core particles, titanium (IV) isopropoxide (TTIP, Sigma Aldrich, purity $>97\%$) was dissolved in xylene (Sigma Aldrich, purity $>99.9\%$) and acetonitrile (ACN, Sigma Aldrich, purity $>99.9\%$), with a volume ratio of 2.2:1 and a fixed concentration of 0.64 M. Through the FSP nozzle capillary, 5 mL min^{-1} of that solution was fed and dispersed by $2\text{--}5\text{ L min}^{-1}$ O_2 gas (Linde, purity $>99.95\%$) from the surrounding annulus and sheathed by an additional $5\text{--}20\text{ L min}^{-1}$ N_2 gas (Linde, purity $>99.9\%$) flowing through the openings of the sinter metal plate. The pressure drop at the nozzle tip was held constantly at 1.5 bar. A premixed stoichiometric ring-shaped methane-oxygen flame CH_4 $1\text{--}3.5\text{ L min}^{-1}$ (Linde, purity $>99.5\%$) and O_2 $2\text{--}5\text{ L min}^{-1}$ (Linde, purity $>99.95\%$) was used to ignite the spray.

For the synthesis of Core-Shell carbon-coated TiO_{2-x} suboxides ($C@TiO_{2-x}$), supplementary to the above was the addition of N_2 gas $3\text{--}60\text{ L min}^{-1}$ through the inlet on the metal sinter tube or suboxic conditions to be fulfilled, and supply of $0.3\text{--}3.5\text{ L min}^{-1}$ of acetylene C_2H_2 gas (Linde, purity $>99.6\%$) through the coating ring.

Chapter 3

Results – Discussion

3.1 – Nanoparticle Synthesis

The scalability of the FSP process described in Chapter 2, enabled us to successfully synthesize carbon-coated titanium suboxides TiO_{2-x} @ C and the FSP-made pristine titanium oxides TiO_2 and suboxides TiO_{2-x} were calcined under carbon-rich CH_4 atmosphere to examine the effect of the reducing atmosphere in terms of the defects created. Table 3.1 summarizes all the produced nanoparticles along with the variable parameters that determine the final product in terms of composition, phase percentage, size and crystallinity.

Material	Particle Configuration	Precursor	Solvents	Precursor Feed rate (mL min ⁻¹) / Dispersion (L min ⁻¹)	Pilot Flame O ₂ /CH ₄ (L min ⁻¹)	Sheath Gas N ₂ /[O ₂] (L min ⁻¹)	N ₂ Blow (L min ⁻¹)	C ₂ H ₂ Flow (L min ⁻¹)
1219	TiO ₂	TTIP 0.64M	Xylene /ACN	5/5	2/1	-	-	-
1221	TiO _{2-x}	TTIP 0.64M	Xylene /ACN	5/5	2/1	10	20	-
1226	TiO ₂	TTIP 0.64M	Xylene /ACN	5/5	2/1	-	-	-
1227	TiO ₂ @C	TTIP 0.64M	Xylene /ACN	5/5	2/1	-	-	1
1228	TiO ₂ @C	TTIP 0.64M	Xylene /ACN	5/5	2/1	-	-	1.5

3.1 – Nanoparticle Synthesis

Material	Particle Configuration	Precursor	Solvents	Precursor Feed rate (mL min ⁻¹) / Dispersion (L min ⁻¹)	Pilot Flame O ₂ /CH ₄ (L min ⁻¹)	Sheath Gas N ₂ /[O ₂] (L min ⁻¹)	N ₂ Blow (L min ⁻¹)	C ₂ H ₂ Flow (L min ⁻¹)
1229	TiO _{2-x}	TTIP 0.64M	Xylene /ACN	5/5	2/1	10	-	-
1230	TiO ₂ @C	TTIP 0.64M	Xylene /ACN	5/5	2/1	10	-	3
1231	TiO ₂ @C	TTIP 0.64M	Xylene /ACN	5/5	2/1	10	-	5
1248	TiO ₂ @C	TTIP 0.64M	Xylene /ACN	5/5	2/1	10	3	3
1249	TiO ₂ @C	TTIP 0.64M	Xylene /ACN	5/5	2/1	10	3	1
1250	TiO ₂ @C	TTIP 0.64M	Xylene /ACN	5/5	2/1	10	20	1.5
1251	TiO ₂ @C	TTIP 0.64M	Xylene /ACN	5/5	2/1	10	20	4
1264	TiO ₂ @C	TTIP 0.64M	Xylene /ACN	5/5	2/1	-	25	3
1265	TiO ₂ @C	TTIP 0.64M	Xylene /ACN	5/5	2/1	-	25	1
1290	TiO ₂	TTIP 0.64M	Xylene	5/5	2/1	10	-	-
1292	TiO _{2-x}	TTIP 0.64M	Xylene	5/5	2/1	10	-	-
1294	TiO _{2-x}	TTIP 0.64M	Xylene	5/5	2/1	10	40	-
1321	TiO ₂ @C	TTIP 0.64M	Xylene	5/5	2/1	5	25	2
1322	TiO _{2-x}	TTIP 0.64M	Xylene	5/5	2/1	10	25	-
1323	TiO ₂ @C	TTIP 0.64M	Xylene	5/5	2/1	10	25	3.5

3.1 – Nanoparticle Synthesis

Material	Particle Configuration	Precursor	Solvents	Precursor Feed rate (mL min ⁻¹) / Dispersion (L min ⁻¹)	Pilot Flame O ₂ /CH ₄ (L min ⁻¹)	Sheath Gas N ₂ /[O ₂] (L min ⁻¹)	N ₂ Blow (L min ⁻¹)	C ₂ H ₂ Flow (L min ⁻¹)
1463	TiO _{2-x}	TTIP 0.64M	Xylene /ACN	5/5	3/2.2	10	-	-
1465	TiO _{2-x}	TTIP 0.64M	Xylene /ACN	5/3	3/2.2	10	10	-
1466	TiO _{2-x}	TTIP 0.64M	Xylene /ACN	5/3	3/2.2	10	20	-
1467	TiO _{2-x}	TTIP 0.64M	Xylene /ACN	5/2.5	3/2.2	10	20	-
1468	TiO _{2-x}	TTIP 0.64M	Xylene /ACN	5/2	3/2.2	10	20	-
1469	TiO _{2-x}	TTIP 0.64M	Xylene /ACN	5/2.25	3/2.2	10	20	-
1470	TiO _{2-x}	TTIP 0.64M	Xylene /ACN	5/2	3/2.2	10	10	-
1474	TiO _{2-x}	TTIP 0.64M	Xylene /ACN	5/3	3/2.2	10	10	-
1477	TiO ₂ @C	TTIP 0.64M	Xylene /ACN	5/3	3/2.2	10	10	0.3
1478	TiO ₂ @C	TTIP 0.64M	Xylene /ACN	5/3	3/2.2	10	10	1
1479	TiO ₂ @C	TTIP 0.64M	Xylene /ACN	5/3	3/2.2	10	10	0.6
1480	TiO ₂ @C	TTIP 0.64M	Xylene /ACN	5/3	3/2.2	10	10	2.5
1481	TiO ₂ @C	TTIP 0.64M	Xylene /ACN	5/3	3/2.2	10	10	2
1598	TiO ₂	TTIP 0.64M	Xylene /ACN	5/5	2/1	[10]	-	-
1599	TiO ₂	TTIP 0.64M	Xylene /ACN	5/5	2/1	[10]	-	-

3.1 – Nanoparticle Synthesis

Material	Particle Configuration	Precursor	Solvents	Precursor Feed rate (mL min ⁻¹) / Dispersion (L min ⁻¹)	Pilot Flame O ₂ /CH ₄ (L min ⁻¹)	Sheath Gas N ₂ /[O ₂] (L min ⁻¹)	N ₂ Blow (L min ⁻¹)	C ₂ H ₂ Flow (L min ⁻¹)
1600	TiO ₂	TTIP 0.64M	Xylene /ACN	5/5	5/3.5	20	-	-
1601	TiO ₂	TTIP 0.64M	Xylene /ACN	5/5	5/3.5	20	-	-
1602	TiO _{2-x}	TTIP 0.64M	Xylene /ACN	5/3	3/2.2	10	10	-
1603	TiO _{2-x}	TTIP 0.64M	Xylene /ACN	5/3	3/2.2	10	25	-
1604	TiO _{2-x}	TTIP 0.64M	Xylene /ACN	5/3	3/2.2	10	25	-
1605	TiO _{2-x}	TTIP 0.64M	Xylene /ACN	5/3	3/2.2	10	25	-

Table 3.1. List of FSP experimental parameters for all synthesized nanoparticles.

The FSP reactor setup was thoroughly investigated in order to achieve the optimal setup for our purpose. The encapsulation of the TiO₂ particles with a carbon shell required the enclosure of the FSP reactor to ensure the core particles follow the correct pathway to meet the acetylene gas flow during the FSP process. The acetylene gas served as the source of the carbon shell and contrary to the process of coating with metal oxides where the precursor vapor of the metal oxides is introduced to the burner chamber with the aid of an inert carrier gas via a ring as discussed in Chapter 2, carbon coating required the pyrolysis of the acetylene gas to ensure carbon shell deposition. The introduction of the acetylene gas at the early stages of the core particle formation process as shown in Fig. 3.1 resulted in segregated domains of carbon and TiO₂. The introduction of premixed C₂H₂ and N₂ gases was not feasible since the setup for the production of metal suboxides required nitrogen radial flows greater than 10 L min⁻¹ as compared to the sub-5 L min⁻¹ of the acetylene gas and the miscibility between the two gases could not be achieved.

3.1 – Nanoparticle Synthesis

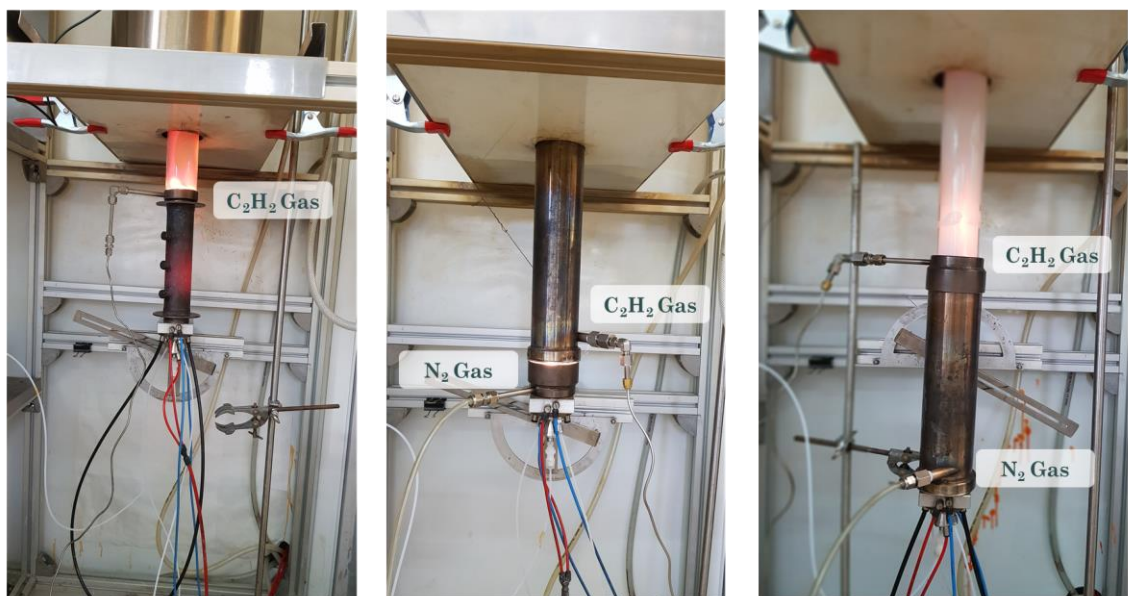


Figure 3.1. Left: FSP reactor setup for carbon-coated TiO₂ oxide particles. Middle: In this FSP setup the C₂H₂ is inserted as a radial flow which leads to segregated domains of TiO₂ and carbon. The introduction of the N₂ gas via a ring doesn't create the swirl effect and reducing atmosphere necessary for the production of TiO_{2-x} suboxides. Right: The optimal FSP setup for the production of TiO_{2-x}@C.

Precursor molarity was kept fixed at 0.64M titanium (IV) isopropoxide (TTIP) and the xylene and acetonitrile solvents were mixed with a 2.2:1 ratio. In some cases, pure xylene was used as a solvent. Sheath gas was constantly fed to the burner to ensure a high temperature zone presence which allows longer residence times in the flame zone and protection of the particle formation pathway. The precursor feed rate, the dispersion oxygen gas as well as the premixed pilot O₂/CH₄ flame were investigated to achieve the optimal parameter setup for each purpose every time.

The carbon-coated samples were calcined under a reductive CH₄ atmosphere in a tubular furnace at different temperatures to improve graphitization since the pyrolysis of C₂H₂ is inevitably accompanied by the presence of carbon soot. The materials were further investigated in terms of the possible defect formation during the carbothermal reduction process. Calcination at temperatures exceeding 600°C led to carbon deposition.

The materials chosen to be the basis for our analysis are materials 1290, 1323 and 1479 with their experimental parameters listed at Table 3.1. The materials as prepared and upon calcination are shown in Fig. 3.2.

3.2 – Crystal Structure

Carbothermal treatment of the samples was done at two different temperatures at 350°C and 800°C respectively for the same calcination time of 2 hours. The rate was kept fixed at 5°C/min as well as the flow of the CH₄ gas at 30 mL / min.

The samples will from now on listed as #material @ calcination temperature for the calcined samples and #material for the as prepared samples. 1323 represents the high carbon content material while material 1479 represents the low carbon content material. Material 1290 serves as a reference P25-like flame made material.



Figure 3.2. Left: From left to right material 1290 and upon calcination at 350°C and 800°C under CH₄ atmosphere, respectively. Middle: From left to right material 1323 and upon calcination at 350°C and 800°C under CH₄ atmosphere, respectively. Right: From left to right material 1479 and upon calcination at 350°C and 800°C under CH₄ atmosphere, respectively.

3.2 – Crystal Structure

3.2.1 – XRD Pattern and Crystal Size

X-Ray Diffraction (XRD) was used to study the crystal structure of the nanomaterials. Fig. 3.3, 3.4 and 3.5 presents the XRD patterns for the as prepared samples and upon calcination at 350°C and 800°C respectively. The XRD patterns were analyzed using Rietveld refinement for the calculation of the phase percentages of each material. The effect of the temperature can be seen directly from the XRD pattern of material 1290. Whereas the as prepared and mildly calcinated material at 350°C are not affected in terms of crystal size and phase composition, the calcinated material at 800°C inevitably experienced phase transition from anatase to rutile as well as crystal growth from 14 nm to 35 nm. This is also the result of the carbon deposition at high calcination temperatures. Furthermore, none of the Magnéli phases has been detected from the XRD pattern of all pristine materials and upon calcination.

3.2.1 – XRD Pattern and Crystal Size

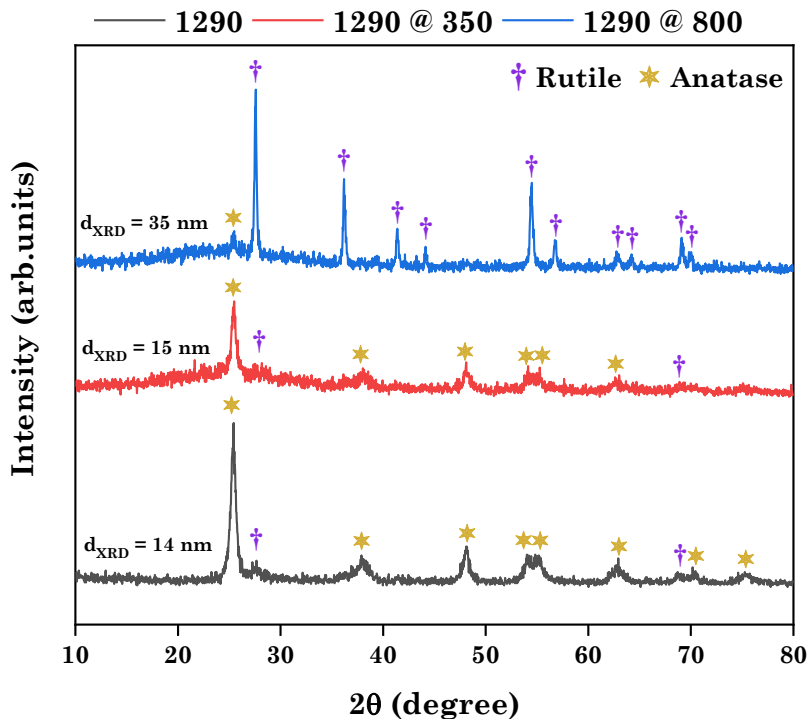


Figure 3.3. XRD pattern of material 1290 and upon calcination at 350°C and 800°C under CH₄ reductive atmosphere respectively.

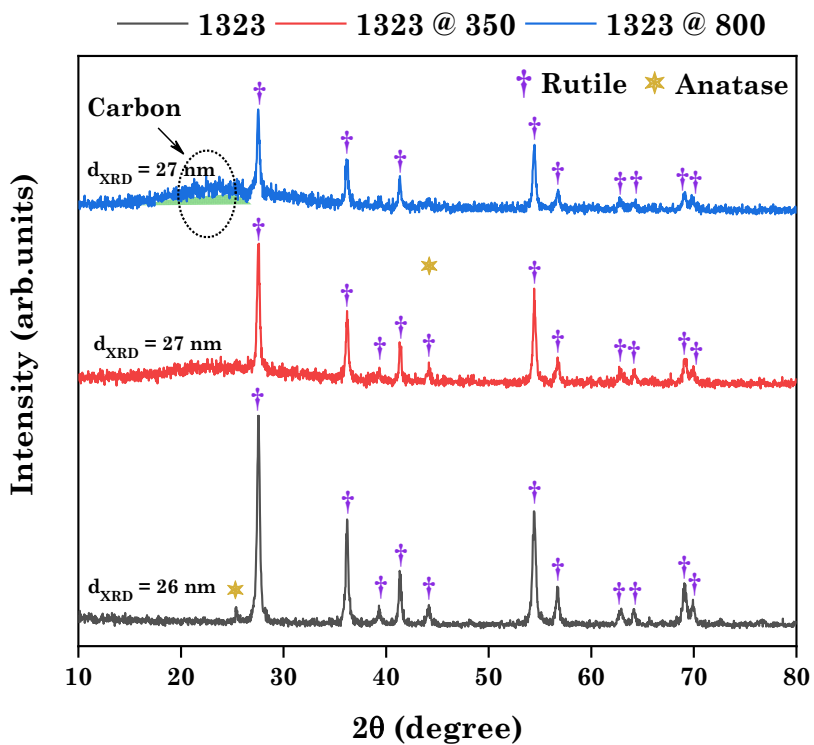


Figure 3.4. XRD pattern of material 1323 and upon calcination at 350°C and 800°C under CH₄ reductive atmosphere respectively.

3.2.1 – XRD Pattern and Crystal Size

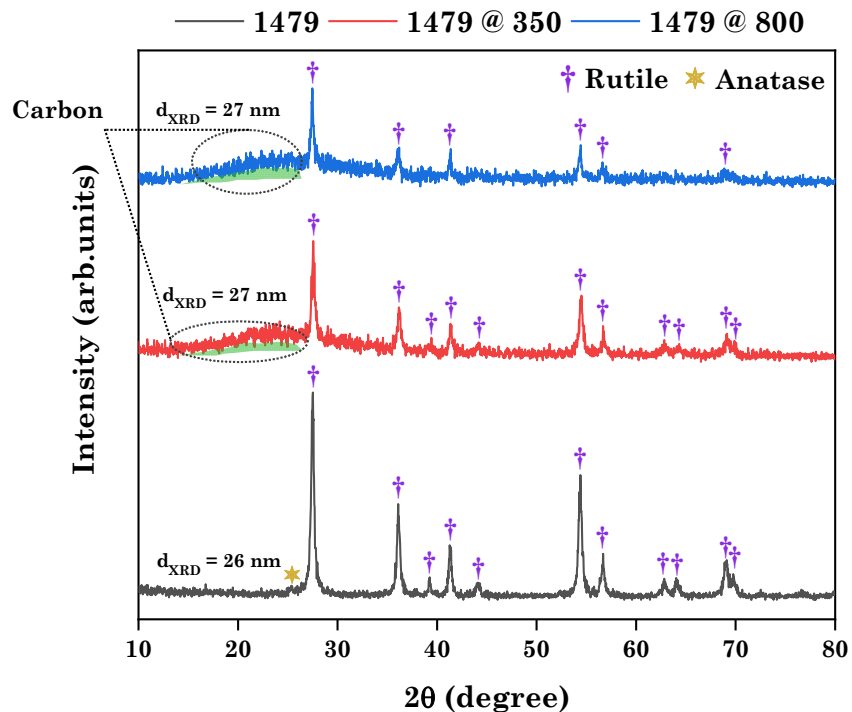


Figure 3.5. XRD pattern of material 1479 and upon calcination at 350°C and 800°C under CH₄ reductive atmosphere, respectively.

Material	% Anatase	% Rutile	d_{XRD} - Anatase (nm)	d_{XRD} - Rutile (nm)
1290	81	19	14	-
1290 @ 350	80	20	15	-
1290 @ 800	12	88	-	35
1323	2	98	-	26
1323 @ 350	3	97	-	27
1323 @ 800	2	98	-	27
1479	2	98	-	26
1479 @ 350	3	97	-	27
1479 @ 800	2	98	-	27

Table 3.2. Phase composition and crystal size of synthesized nanoparticles as prepared and upon calcination at 350°C and 800°C under CH₄ atmosphere, respectively.

3.2.1 – XRD Pattern and Crystal Size

If we investigate the XRD pattern of materials 1323 and 1479 and upon calcination, we conclude that no particle growth occurred upon calcination and that the dominant crystal phase is rutile. In contrary to the open flame material 1290 which is the TiO₂ oxide, the carbon-coated suboxides 1323 and 1479 are almost completely rutile and no particle growth occurred. This can be due to the carbon shell which suppressed further growth.

The rutile structure of the carbon-coated suboxides in materials 1323 and 1479 can be correlated with the presence of the acetylene gas during the combustion process. For each flame of P mL/min precursor solution and D L/min dispersion oxygen, hereafter denoted as P/D flame, the ratio of the combustion enthalpy introduced by the precursor, solvent and fuel (methane) into the flame (\dot{H}_c in MJ/min) over the total (liquid and gas) inlet mass flow rate, $\dot{m}_{\text{tot,in}}$ (kg/min) can be calculated using the following formula¹⁰¹:

$$\frac{\dot{H}_c}{\dot{m}_{\text{tot,in}}} = \frac{(\dot{n}_{\text{precursor}}\Delta H_c^{\text{precursor}} + \dot{n}_{\text{solvent}}\Delta H_c^{\text{solvent}} + \dot{n}_{\text{CH}_4}\Delta H_c^{\text{CH}_4})}{\dot{m}_{\text{precursor-solution}} + \dot{m}_{\text{dispersion-O}_2} + \dot{m}_{\text{CH}_4\text{-flame}} + \dot{m}_{\text{O}_2\text{-flame}}} \quad (3.1)$$

where \dot{n} and \dot{m} are the inlet flow rates in mol/min and kg/min, respectively, and ΔH_c is the combustion enthalpy of each compound. The above equation gives only the enthalpy density supplied to the FSP burner without considering entrainment of ambient air into the flame. The ratio $\dot{H}_c/\dot{m}_{\text{tot,in}}$ will be hereafter referred to as “FSP feed enthalpy density”. The presence of the acetylene gas during the combustion process alters the above equation since the acetylene gas serves as an extra fuel to the combustion process and consequently cannot be neglected. Therefore, Eq. 3.1 needs to be modified to incorporate the acetylene gas as follows:

$$\frac{\dot{H}_c}{\dot{m}_{\text{tot,in}}} = \frac{(\dot{n}_{\text{precursor}}\Delta H_c^{\text{precursor}} + \dot{n}_{\text{solvent}}\Delta H_c^{\text{solvent}} + \dot{n}_{\text{CH}_4}\Delta H_c^{\text{CH}_4} + \dot{n}_{\text{C}_2\text{H}_2}\Delta H_c^{\text{C}_2\text{H}_2})}{\dot{m}_{\text{precursor-solution}} + \dot{m}_{\text{dispersion-O}_2} + \dot{m}_{\text{CH}_4\text{-flame}} + \dot{m}_{\text{O}_2\text{-flame}} + \dot{m}_{\text{C}_2\text{H}_2\text{-ring-flame}}} \quad (3.2)$$

The presence of the extra term in Eq. 3.2 to include the acetylene gas contribution has profound effect on the value of the FSP feed enthalpy density. The acetylene gas, upon pyrolysis during the particle formation process elongates the hot zone area in the burner chamber and as a result, the nanoparticles have longer residence times in the hot zone area which inevitably lead to the anatase to rutile transformation. This fact is further supported by the high filter temperature during particle collection. For the materials 1323 and 1479 the filter temperature was over 350°C. If we take into consideration Eq. 3.2 the FSP enthalpy feed density is shown to augment rapidly with the acetylene flow as shown in Fig. 3.6.

3.2.2 – Surface and Pore Analysis

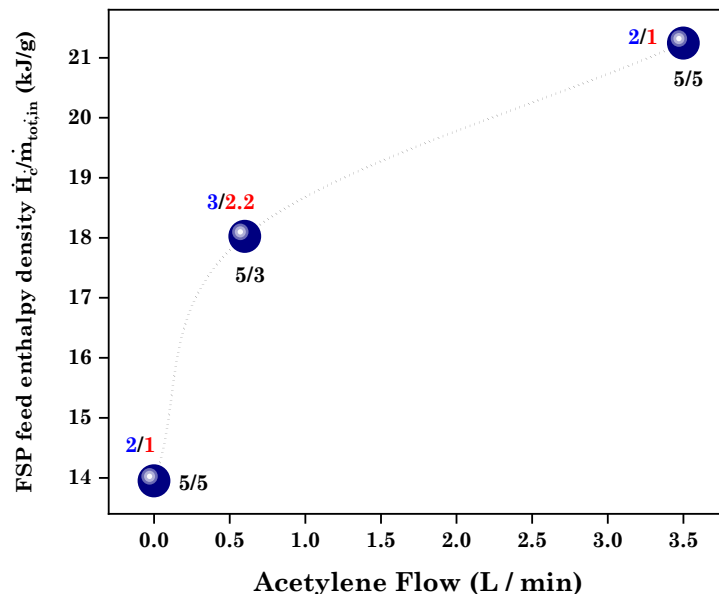


Figure 3.6. FSP feed enthalpy density as a function of the acetylene flow for materials 1290 1323 and 1479. The precursor to dispersion feed ratio P/D is noted along with the pilot flame O_2/CH_4 . Starting from the TiO_2 oxide 1290 material with no acetylene flow at 13.9 kJ/g, the carbon-coated $\text{TiO}_{2-x}\text{@C}$ 1479 material with low acetylene flow at 0.6 L/min at 18 kJ/g and the $\text{TiO}_{2-x}\text{@C}$ 1323 material with high acetylene flow at 3.5 L/min with 21.2 kJ/g.

3.2.2 – Surface Structure and Pore Analysis

In order to get an insight into the surface structure of the materials, Brunauer-Emmett-Teller analysis was implemented to determine the specific surface area (SSA) of the produced nanoparticles. Fig. 3.7, 3.8 and 3.9 show the BET isotherms and the specific surface area (SSA) measurements for the materials 1290, 1323 and 1479, respectively. Starting from the TiO_2 oxide material 1290, the surface area is shown to be in the range of 100 m^2/g . Both the carbon-coated $\text{TiO}_{2-x}\text{@C}$ suboxides namely 1323 and 1479 have significantly less SSA than 1290 valued at 39 m^2/g and 42 m^2/g respectively, however between materials 1323 and 1479, the SSA does not present great fluctuation. Graphite is known for having SSA values exceeding 300 m^2/g , therefore the surface of both 1323 and 1479 consists of defective carbon which explains the smaller SSA values as compared to those of graphite. The increase of the carbon shell thickness from material 1479 to material 1323 was not accompanied with an increase in the specific surface area.

3.2.2 – Surface and Pore Analysis

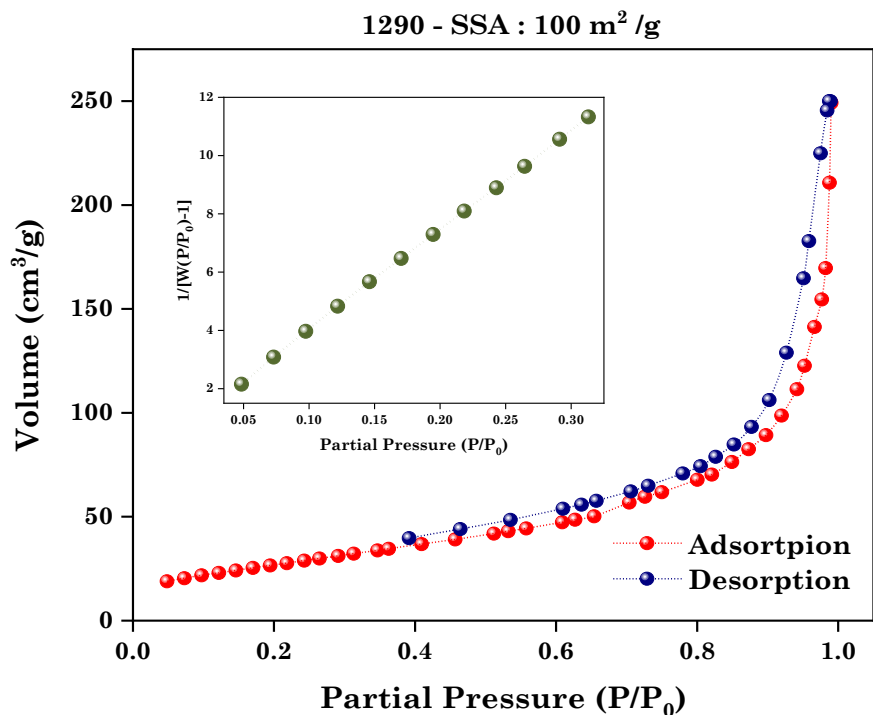


Figure 3.7. BET isotherm of 1290 TiO₂ nanomaterial. Inset: Linear multipoint BET plot for the determination of the specific surface area.

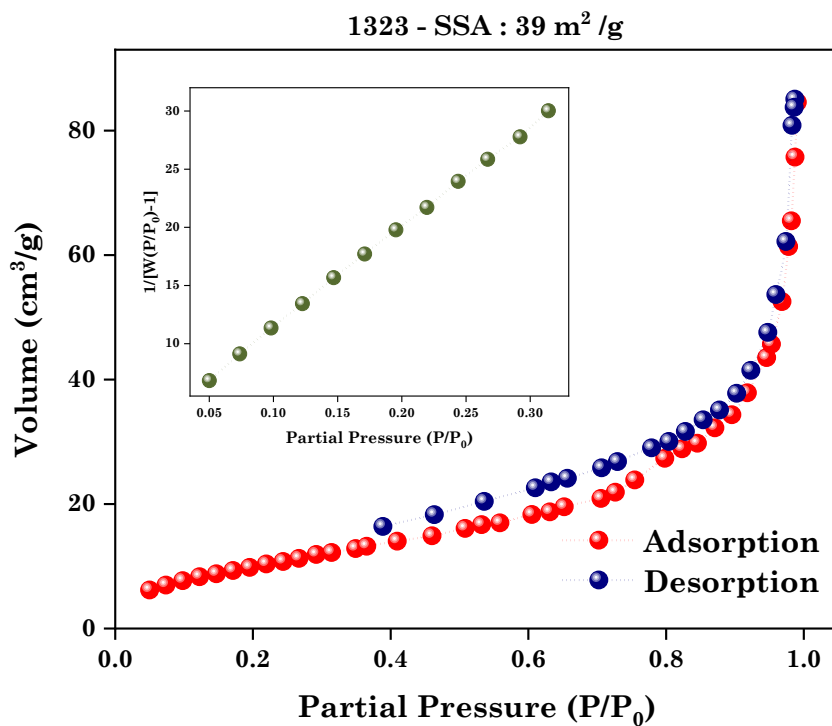


Figure 3.8. BET isotherm of 1323 TiO_{2-x}@C nanomaterial. Inset: Linear multipoint BET plot for the determination of the specific surface area.

3.3 – Uv-Vis Diffuse Reflectance Spectroscopy (DRS) Results

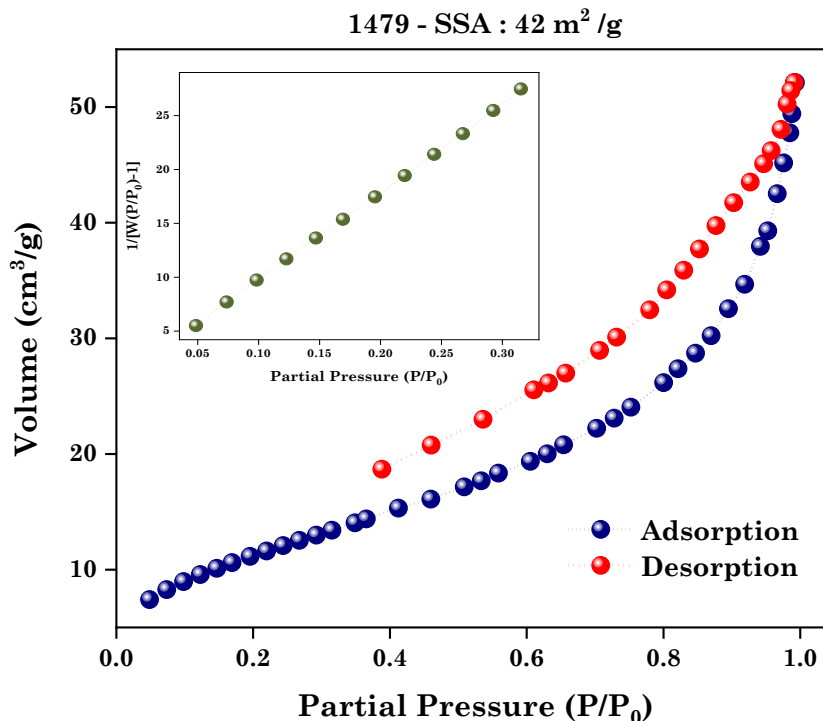


Figure 3.9. BET isotherm of 1479 TiO_{2-x}@C nanomaterial. Inset: Linear multipoint BET plot for the determination of the specific surface area.

3.3 – Uv-Vis Diffuse Reflectance Spectroscopy (DRS) Results

The optical properties of nanoparticles are greatly influenced by their structure as well as the presence of imperfections known as defects. As discussed in Chapter 1, TiO₂ is a wide band-gap semiconductor with optical bandgap values of 3.2 eV and 3.0 eV for anatase and rutile polymorphs, respectively. The surface functionalized carbon-coated titanium suboxide nanoparticles therefore will present different DRS spectrum as compared to their oxide non-coated counterparts. Carbon-coating the surface of a nanoparticle leads to the positioning of mid gap states introduced by the carbon content on the nanoparticles surface. This leads to bandgap narrowing and can lead to visible-driven applications.

Intuitively, the most efficient light-harvesting nanoparticle appears black to naked eye. This was the case with disorder engineered “black Titania”¹⁰² in which the appearance of Ti³⁺ centers upon hydrogenation resulted in the superb visible response of the nanoparticles. In our case, the presence of oxygen vacancies due to the oxygen-lean atmosphere in the FSP burner

3.3 – Uv-Vis Diffuse Reflectance Spectroscopy (DRS) Results

chamber, as well as the carbon entering the subsurface as an intrinsic dopant during the coating process leads to bandgap narrowing. Ti^{3+} ions located at the surface of the particles are known to act as the coloration center¹⁰³.

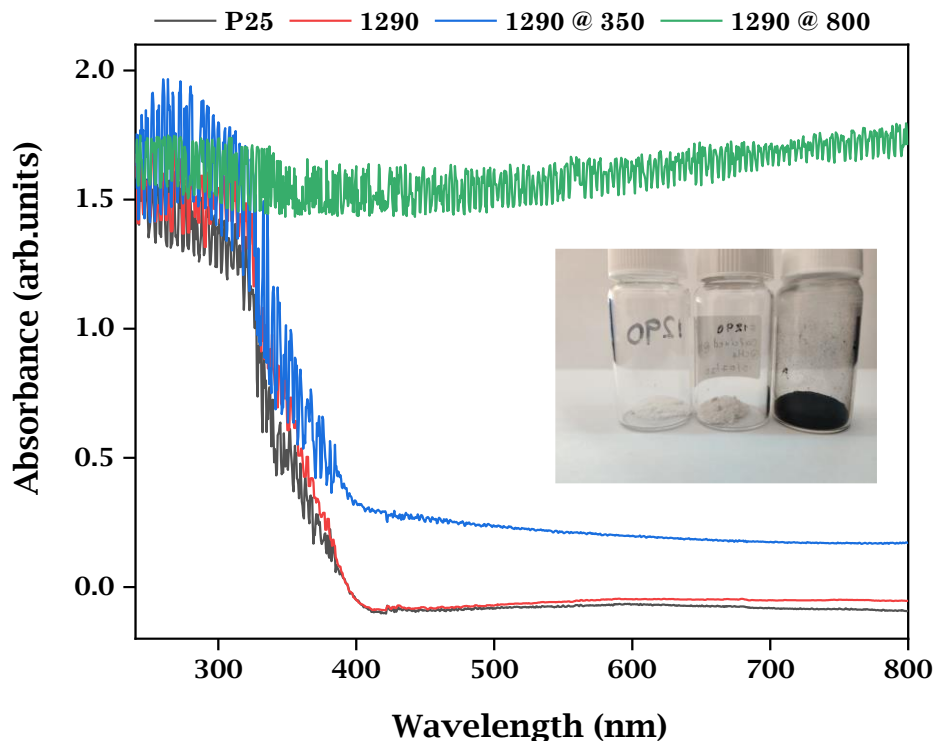


Figure 3.10. DRS spectrum of pristine material 1290 and upon calcination at 350°C and 800°C respectively. P25 is plotted as a reference material. Inset: Color change from left to right for pristine 1290 material and upon calcination at 350°C and 800°C, respectively.

As we can see in Fig. 3.10 starting from the pristine 1290 TiO_2 material, it possesses a bandgap close to that of the P25 reference material. Mild calcination at 350°C under CH_4 atmosphere resulted in a decrease in bandgap value whereas the calcination at 800°C resulted in a complete black material. The upshift of the linear part in DRS plot before the absorption step is consistent with the color change observed between the pristine 1290 material and upon calcination.

Fig. 3.11 presents the Tauc plot used for the determination of the optical bandgap value. As we can see the bandgap value of the pristine material is in close agreement with the P25 reference material. Upon calcination at 350°C, the bandgap value is decreased to approximately 2.5 eV whereas the material calcined at 800°C shows no absorbance at all resulting from the excess carbon deposition during carbothermal treatment.

3.3 – Uv-Vis Diffuse Reflectance Spectroscopy (DRS) Results

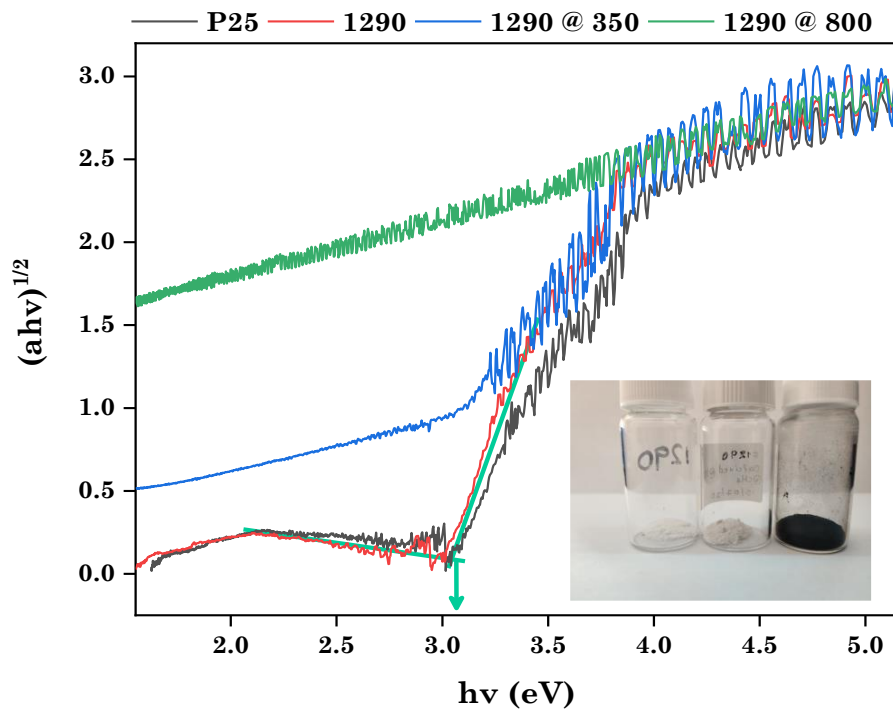


Figure 3.11. Tauc plot of the pristine 1290 material and upon calcination at 350°C and 800°C respectively. P25 reference material is also plotted. Inset: Color change from left to right for pristine 1290 material and upon calcination at 350°C and 800°C, respectively.

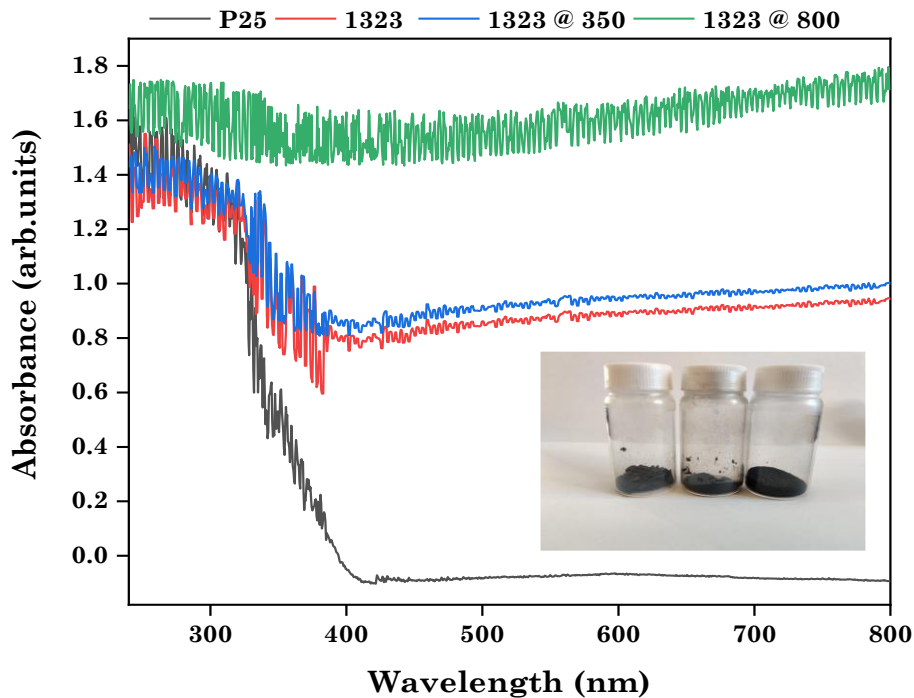


Figure 3.12. DRS spectrum of pristine material 1323 and upon calcination at 350°C and 800°C respectively. P25 is plotted as a reference material. Inset: Color change from left to right for pristine 1323 material and upon calcination at 350°C and 800°C, respectively.

3.3 – Uv-Vis Diffuse Reflectance Spectroscopy (DRS) Results

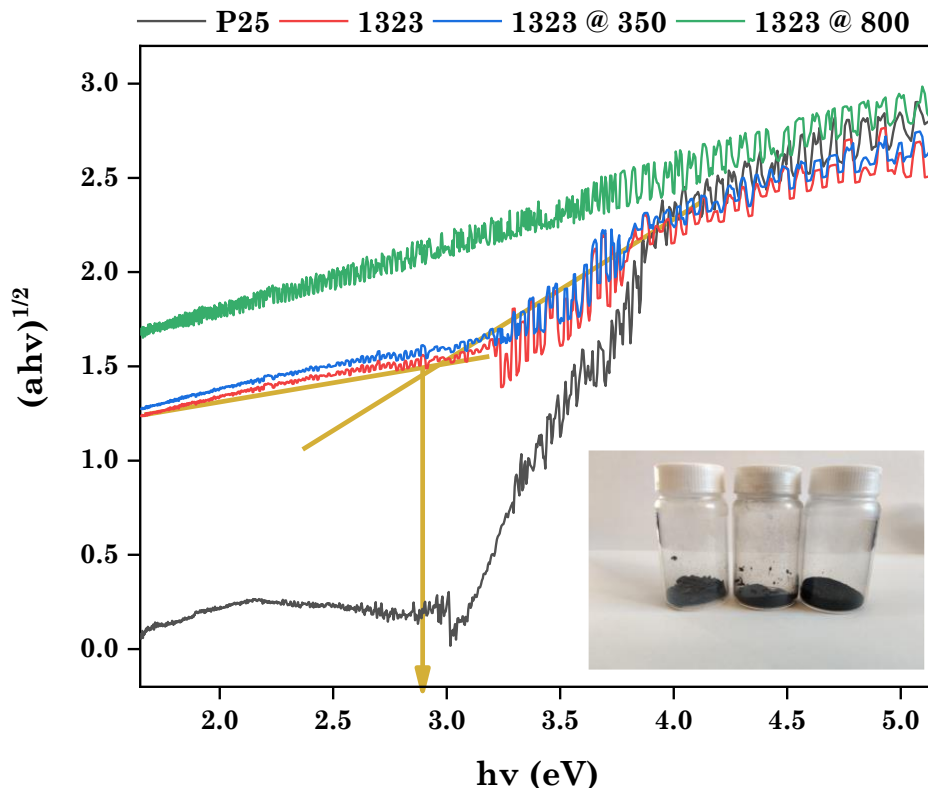


Figure 3.13. Tauc plot of the pristine 1323 material and upon calcination at 350°C and 800°C respectively. P25 reference material is also plotted. Inset: Color change from left to right for pristine 1323 material and upon calcination at 350°C and 800°C, respectively.

The DRS plot of the carbon-coated titanium suboxide $\text{TiO}_{2-x}\text{@C}$ 1323 material is depicted in Fig. 3.12. As we can see beginning from the pristine 1323 material, the upshift of the linear part before the absorption step is in good agreement with the color change noticed in the pristine material as compared to the white TiO_2 . We must also notice here that there is no significant color change between the pristine 1323 material and upon calcination at 350°C and 800°C. We must also notice that the change on the gradient is relatively small as compared to the TiO_2 oxide.

The Tauc plot of 1323 material and upon calcination is presented in Fig. 3.13. It is clear that while both the pristine 1323 and the 350°C calcined materials present a relatively small absorption, the 800°C calcined material shows no sign of absorption at all. This can be explained due the possible thick shell thickness which affects the optoelectronic properties of the core material.

3.3 – Uv-Vis Diffuse Reflectance Spectroscopy (DRS) Results

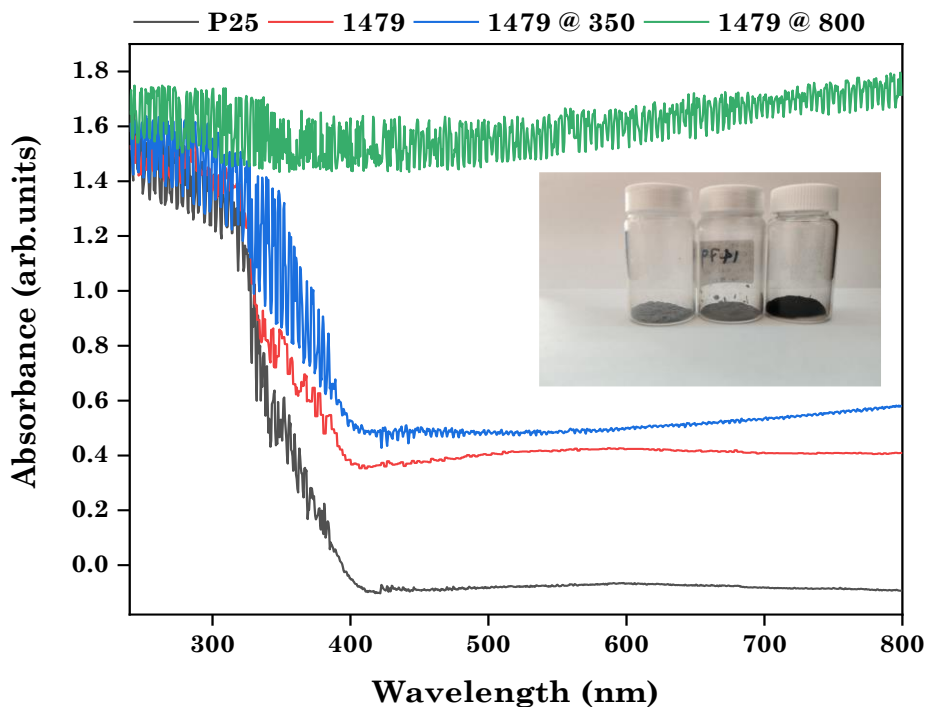


Figure 3.14. DRS spectrum of pristine material 1479 and upon calcination at 350°C and 800°C respectively. P25 is plotted as a reference material. Inset: Color change from left to right for pristine 1479 material and upon calcination at 350°C and 800°C, respectively.

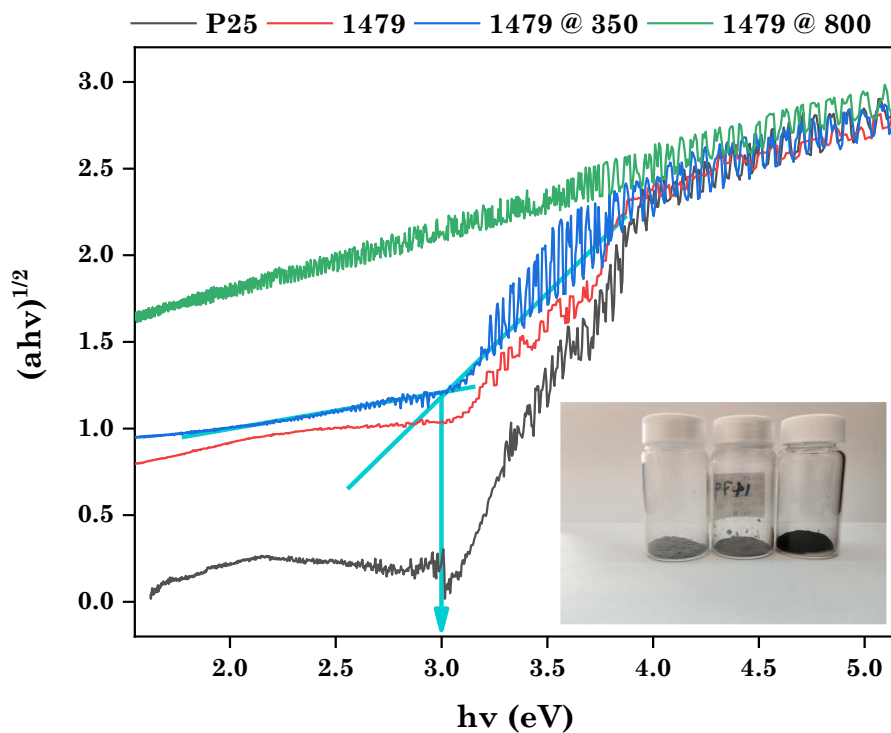


Figure 3.15. Tauc plot of the pristine 1479 material and upon calcination at 350°C and 800°C respectively. P25 reference material is also plotted. Inset: Color change from left to right for pristine 1479 material and upon calcination at 350°C and 800°C, respectively.

3.3 – Uv-Vis Diffuse Reflectance Spectroscopy (DRS) Results

An intermediate state between the oxide TiO₂ 1290 and the carbon-coated TiO_{2-x}@C suboxic 1323 material is encountered in material 1479. In Fig. 3.14, starting from the pristine material, it is clear that the upshift in the linear part before the absorption step at the DRS plot is smaller compared to that of 1323 material. This is consistent with the grey-colored 1479 powder as compared to the blue-black of 1323. Furthermore, the absorption step is significantly greater than that of material 1323 but not as much as TiO₂ 1290 oxide. This implies that then thickness of the carbon shell is less than that of 1323 material. In Fig. 3.15, we can see from the Tauc plot that the bandgap value for the pristine 1479 and the 350°C calcined is close to the 3eV region which can be explained by the presence of the carbon-shell and the possible presence of Ti³⁺ close to the surface. Table 3.3 summarizes the bandgap values of all the pristine and calcined materials as they were calculated from the Tauc plot.

Material	Bandgap Energy (eV)
P25	3.2
1290	3.1
1290 @ 350	2.9
1290 @ 800	-
1323	2.8
1323 @ 350	2.8
1323 @ 800	-
1479	2.9
1479 @ 350	2.9
1479 @ 800	-

Table 3.3. Bandgap energy values for pristine and calcined materials at 350°C and 800°C respectively.

3.4 – Raman Spectroscopy Results

Raman spectroscopy provides information about vibrational and rotational modes of molecules. The shape of the Raman spectrum is dictated by the symmetry of the materials, with each material having a unique fingerprint of Raman modes. The symmetry of the different titanium polymorphs was analyzed in Chapter 1. Based on those symmetries, there are Raman modes for each polymorph. The Raman active modes for anatase and rutile are listed in Table 3.4.

Anatase		Rutile	
Assignment	Raman Shift (cm ⁻¹)	Assignment	Raman Shift (cm ⁻¹)
E _g	144	B _{1g}	143
E _g	197	-	235
B _{1g}	399	E _g	447
A _{1g}	513	A _{1g}	612
B _{1g}	519	B _{2g}	826
E _g	639		

Table 3.4. Raman active modes for anatase and rutile respectively¹⁰⁴.

The presence of the carbon shell will also influence the shape of the Raman spectrum. Two characteristic peaks appear in the Raman spectrum of carbon-related materials which determine if the material is graphite-like (sp²) or diamond-like (sp³). Ferrari *et al*¹⁰⁵ reported the a mode at around 1350 cm⁻¹ termed as D-Band and another mode at 1580 cm⁻¹ termed as G-Band. G-Band is assigned to graphite whereas the D-Band reveals the defects of the carbon species. The peak intensity ratio of the D-Band to that of the G-Band is a direct measure of the defective nature of the carbon.

3.4 – Raman Spectroscopy Results

The peak position as well as the graphitelike-diamondlike shape of the curve is strongly influenced by the excitation energy of the source¹⁰⁶. Lower excitation energies (as in our case the 785 nm laser source) tend to shift the D-Band to lower values from the original 1350 cm^{-1} close to 1310 cm^{-1} , whereas the G-Band shifts are not so observable. Furthermore, the ratio I_D / I_G alters between samples measured with different excitation sources.

The combustion of the precursor in the flame environment is accompanied by the presence of carbon soot. In some cases, the presence of carbon soot is verified via Raman spectroscopy. The addition of the acetylene gas during the carbon-coating process, adds additional fuel to the flame environment inevitably depositing carbon soot on the carbon-coated nanoparticles. It is often in Raman spectrum of soot-containing nanoparticles to present a photoluminescence background¹⁰⁷.

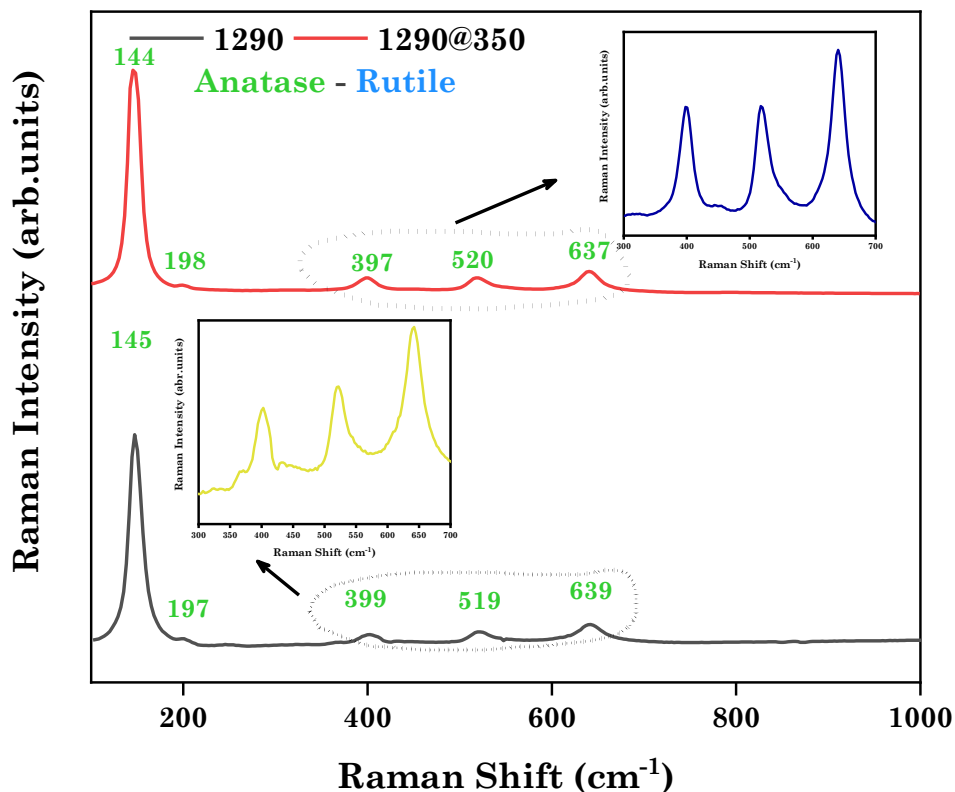


Figure 3.16. Raman spectrum of pristine TiO_2 material 1290 and upon calcination at 350°C respectively. Photoluminescence background appears in the calcined sample without the detection of carbon soot.

Starting from the pristine material 1290 and we can see clearly the well-defined peaks of anatase vibrational modes as stated in Table 3.4. Upon calcination at 350°C the spectrum exhibits a photoluminescence background which as stated before is usually soot related. The broad scan up to 2000 cm^{-1} did not reveal the presence of carbon soot.

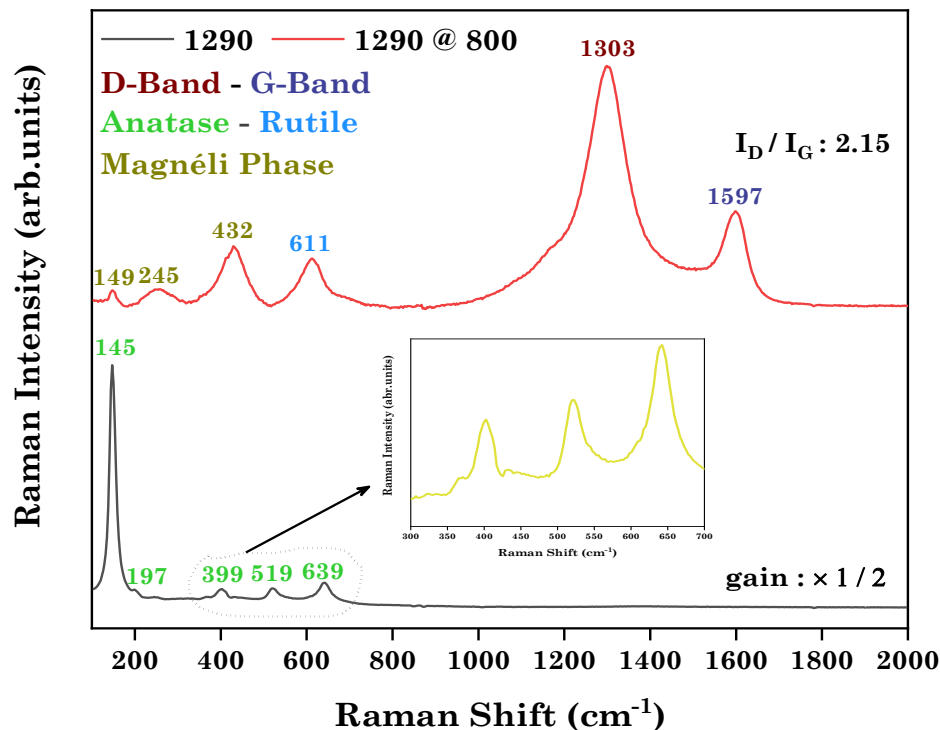


Figure 3.17. Raman spectrum of pristine TiO₂ material 1290 and upon calcination at 800°C. Calcination at elevated temperatures led to heavy carbon deposition which explains the black colored powder.

Calcination at elevated temperatures of 800°C was accompanied with carbon deposition which is verified in Fig. 3.17. The white-colored pristine TiO₂ material 1290 eventually upon calcination came out black-colored. The I_D/I_G ratio reveals that the deposited carbon is not graphitic but defective. We must also note the peak shift of D-Band from 1350 cm⁻¹ to 1303 cm⁻¹ and the smaller peak shift of the G-Band from 1580 cm⁻¹ to 1597 cm⁻¹. As stated above, this shift is correlated with the excitation source (785 nm laser).

Raman spectrum of the pristine carbon-coated TiO_{2-x}@C material 1323 and upon calcination at 350°C is presented in Fig. 3.18. As expected from the XRD results, we encounter the well-defined peaks, but one might notice that if we compare the peak positions present in both the pristine and the calcined material with those of rutile listed on Table 3.4, a shift in the main peaks is observed. Wang *et al*¹⁰⁸ reported shift in rutile peaks on Magnéli phase titanium suboxides. The shift reported matches the shift observed in both pristine 1323 and the 350°C-calcined material. Since Raman spectroscopy is a surface-sensitive technique, and there is no XRD evidence of Magnéli phases, we hypothesize that are randomly distributed close the surface since the XRD provides information about the bulk material and not about the surface.

3.4 – Raman Spectroscopy Results

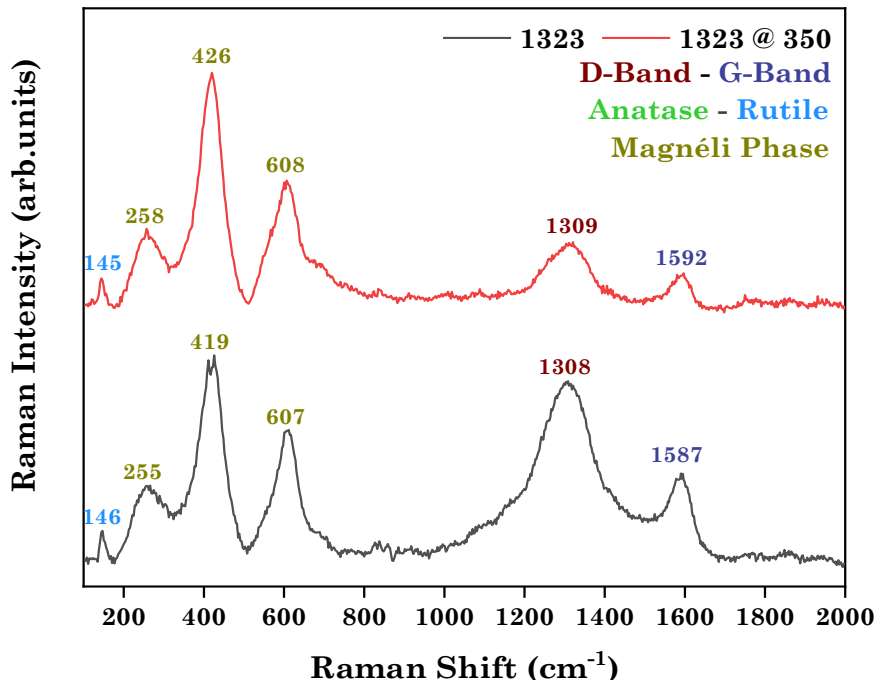


Figure 3.18. Raman spectrum of pristine carbon-coated TiO_{2-x}@C material 1323 and upon calcination at 350°C. The shift of the rutile peaks is evident for both the pristine and calcined material.

The 235 cm⁻¹ peak has shifted to 255 cm⁻¹ and 258 cm⁻¹ in the pristine 1323 and calcined material respectively. The same behavior is observed in the 447 cm⁻¹ rutile peak, only this time shift is towards lower values at 419 cm⁻¹ and 426 cm⁻¹ for the pristine 1323 and calcined material.

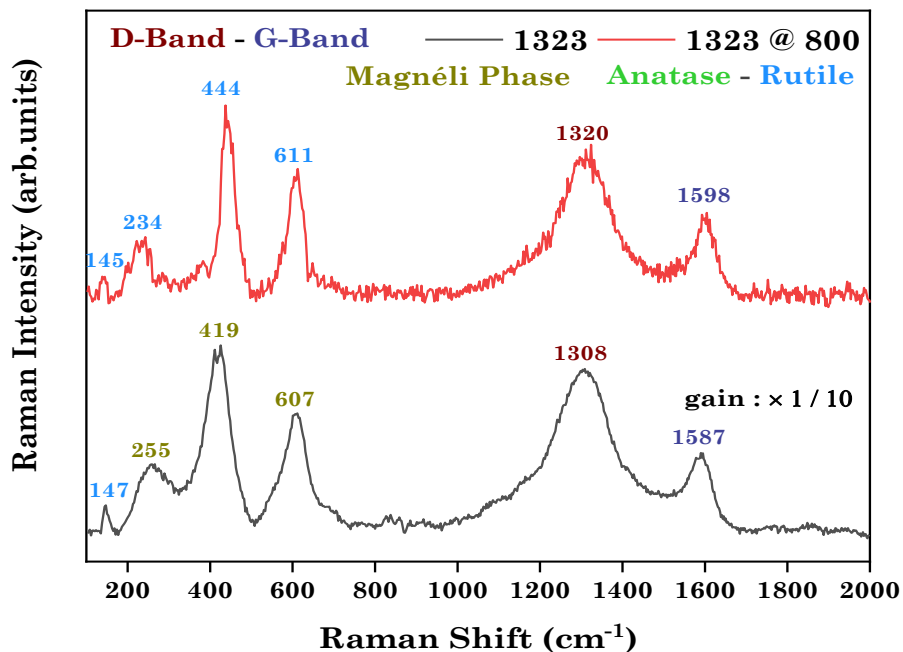


Figure 3.19. Raman spectrum of pristine carbon-coated TiO_{2-x}@C material 1323 and upon calcination at 800°C. The shift of the rutile peaks observed in the 350°C-calcined material is not observed in the 800°C-calcined.

3.4 – Raman Spectroscopy Results

This is not the case for the calcined 1323 material at 800°C. As shown in Fig. 3.19, the peaks are not shifted but are in very good agreement with the typical rutile peaks. The elevated calcination temperature allowed the material to crystallize to the original rutile phase rather than having Magnéli phase clusters close to the surface.

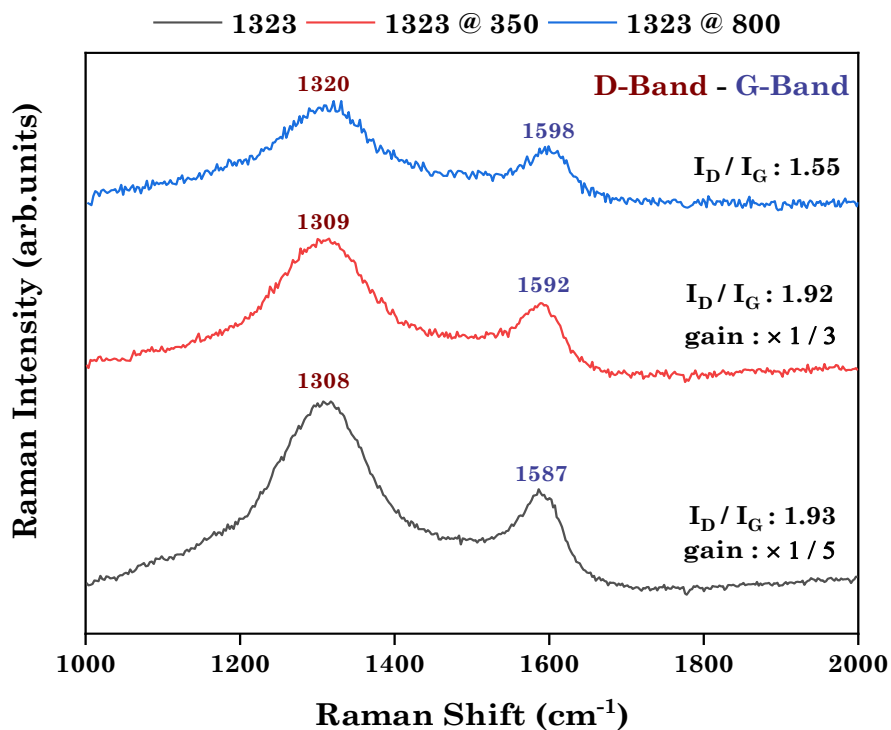


Figure 3.20. Raman spectrum of pristine 1323 material and upon calcination at 350°C and 800°C respectively. The graphitization of the carbon shell is shown to improve upon calcination at high temperature based on the ratio I_D / I_G .

If we examine the scan between 1000 cm⁻¹ and 2000 cm⁻¹ in Fig. 3.20, we can see that the calcination improved the graphitization of the carbon shell. The reduction of the I_D / I_G ratio from 1.93 for the pristine 1323 material down to 1.55 for the 800°C-calcined 1323 material suggests that the core particle is covered with a carbon shell that upon calcination begins to “heal” the defective carbon species and carbon-soot present from the pyrolysis of the acetylene in the FSP process.

An intermediate between the fully oxide TiO₂ 1290 material and the high-carbon content TiO_{2-x}@C 1323 material is the carbon-coated 1479 material. If we have a look at Fig. 3.21 and Fig. 3.22, we can again see the shift of the main rutile peaks to higher and lower values for the pristine and the calcined 1479 materials. This as before, can be attributed to the presence of Magnéli phase clusters, close to the surface that cannot be detected by means of XRD.

3.4 – Raman Spectroscopy Results

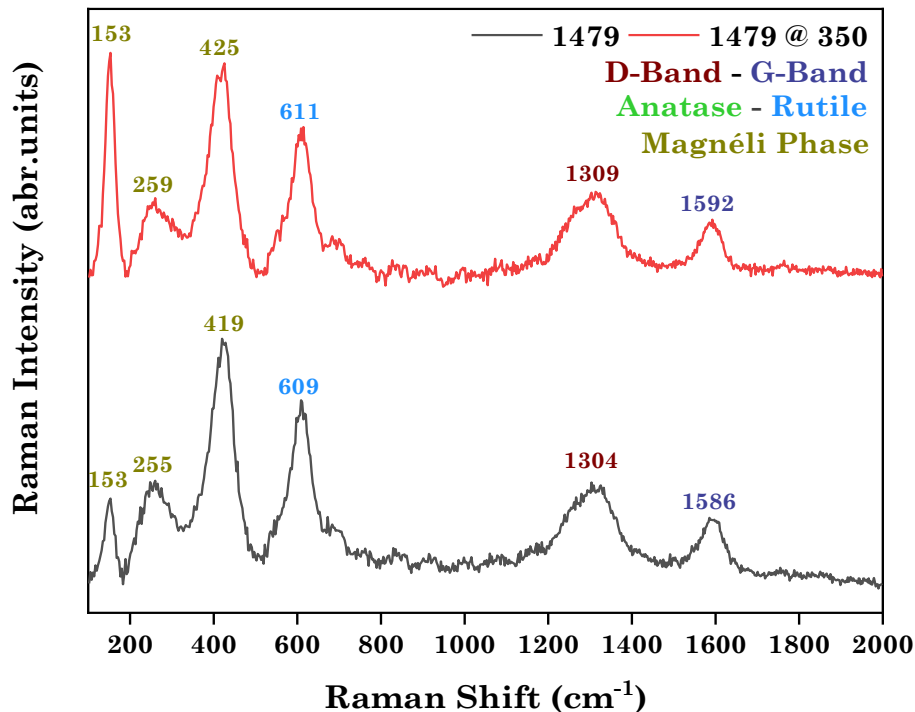


Figure 3.21. Raman spectrum of pristine carbon-coated TiO_{2-x}@C material 1479 and upon calcination at 350°C. The shift of the rutile peaks is evident for both the pristine and calcined material.

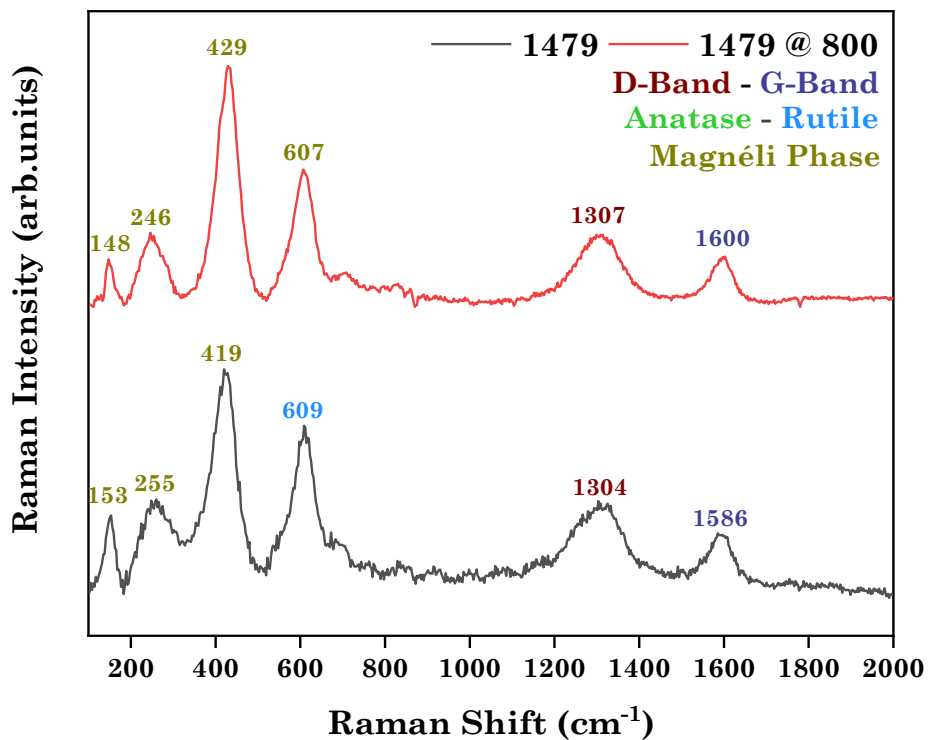


Figure 3.22. Raman spectrum of pristine carbon-coated TiO_{2-x}@C material 1479 and upon calcination at 800°C. The shift of the rutile peaks is evident for both the pristine and calcined material.

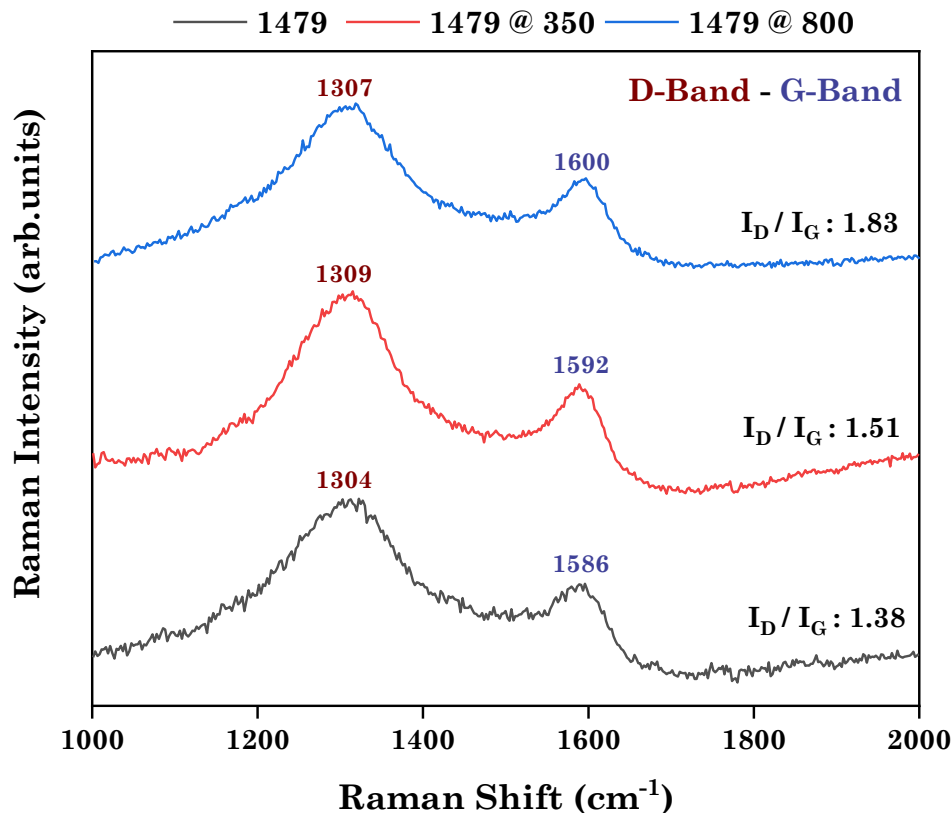


Figure 3.23. Raman spectrum of pristine 1479 material and upon calcination at 350°C and 800°C respectively. The graphitization of the carbon shell is shown to be affected negatively upon calcination at moderate and high temperature based on the ratio I_D / I_G .

If we examine 1479 material and upon calcination from the carbon perspective, as shown in Fig. 3.23, we can see the calcination negatively affects the carbon shell in terms of graphitization. The I_D / I_G ratio begins to shift to higher values thus affecting the quality of the carbon species in the coating shell. This can be attributed to the fact, that due to the low acetylene flow during the FSP process in 1479 material, the core is not entirely encapsulated with a hermetic shell but rather a “patchy” shell. This “patchy” shell upon calcination begins to become more hermetic but the carbon deposition in the carbothermal treatment seems to fill the “patches” with defective carbon species. This is the reason the graphitization of the carbon shell worsens upon carbothermal treatment. If we take into account the 800°C-calcined TiO₂ 1290 material, it is evident that the carbon deposition was with defective carbon species hence the 2.15 I_D / I_G ratio.

Similar findings as far as the carbon coating part is concerned using FSP technology have been reported by Athanassiou *et al*^{72,109} on carbon-coated copper nanoparticles.

3.5 – Comparison of XRD, DRS and Raman Results

If we combine the results from the DRS and Raman spectroscopy with the diffraction patterns from XRD we can come to some conclusions concerning the structure of both the core and the shell material.

XRD patterns of all pristine and calcined materials did not show the presence of Magnéli phases. This means that should these novel phases exist, they cannot be found in the bulk of the material so they must be located in the surface of the materials. Furthermore, we examined the crystal phase of the produced nanoparticles as prepared and upon calcination and found out that at the carbon-coated 1323 and 1479 particles rutile was almost the only phase present. This can be explained as follows: The acetylene gas adds extra fuel to the burner chamber and since it is pyrolyzed, it elongates the hot zone flame environment. As a result, the particles being produced have longer residence times at higher temperature zones which inevitably leads to the anatase to rutile transformation.

DRS spectrum of the produced nanoparticles revealed their optical properties. The pristine 1323 material and the 350°C-calcined one showed minimal absorbance which vanished in the 800°C-calcined material. The minimal absorbance can be explained by the presence of a thick carbon shell which hinders intraband transitions between valence and conduction band of the core TiO₂ nanoparticle. In the case of the 1479 material, things are a little bit different. The absorbance is significantly higher than that of 1323 material and slightly less than that of TiO₂ material.

Raman spectroscopy provided valuable information concerning the structure of the carbon shell as well as the possible presence of Magnéli phase clusters at the surface of the materials. The results suggested in the case of the 1323 material, the presence of a thick carbon shell with defective carbon species which upon calcination ameliorates the degree of graphitization as the methane atmosphere “heals” the defective species. On the contrary, in the case of the 1479 material, it revealed the exact opposite. More specifically, it revealed the presence of a “patchy” shell that upon calcination began to fill the gaps towards a hermetic shell with defective carbon species. Carbon deposition during carbothermal treatment occurred on the “patchy” shell with carbon that degraded the carbon quality of the shell.

As far as the presence of Magnéli phase clusters in the surface of the particles, we discerned that the shift of the main rutile peaks in the carbon-coated pristine and calcined 1323 and 1479 materials has been ascribed to the presence of Magnéli phase clusters at the surface, given that

3.5 – Comparison of XRD, DRS and Raman Results

we have no XRD evidence of Magnéli phase and that Raman spectroscopy is a surface sensitive technique. In order to explain the possible presence of those clusters at the surface we need to go to the particle formation process. In our experimental configuration, acetylene has a dual role. It can serve as a carbon source which upon pyrolysis can carbon-coat nanoparticles but let us not forget that acetylene is a reductive agent. This means that at the elevated temperatures in the burner chamber, the acetylene gas basically *in situ* performs carbothermal reduction in the core nanoparticles. The high acetylene flows tend to converge more to thick carbon-shell creation rather than boosting carbothermal reduction as shown by the absence of peak shifting in the 800°C-calcined 1323 material.

We must also consider the effect of the carbothermal treatment on the particles. When TiO_2 or carbon-coated $\text{TiO}_{2-x}\text{@C}$ is exposed to a reducing agent like CH_4 used for calcination, a significant amount of charged defects may form as oxygen atoms are removed from the lattice and the surface, leaving behind Ti^{3+} sites and oxygen vacancies. We can detect those defects and classify where they originate from lattice or surface by means of EPR.

The verification of the presence of Magnéli phase clusters, as well as the electron behavior and the preliminary evaluation of photocatalytic efficiency will be discussed and determined by means of EPR. So far, the general knowledge about the carbon-coated $\text{TiO}_{2-x}\text{@C}$ nanoparticles can be summarized in Fig. 3.24.

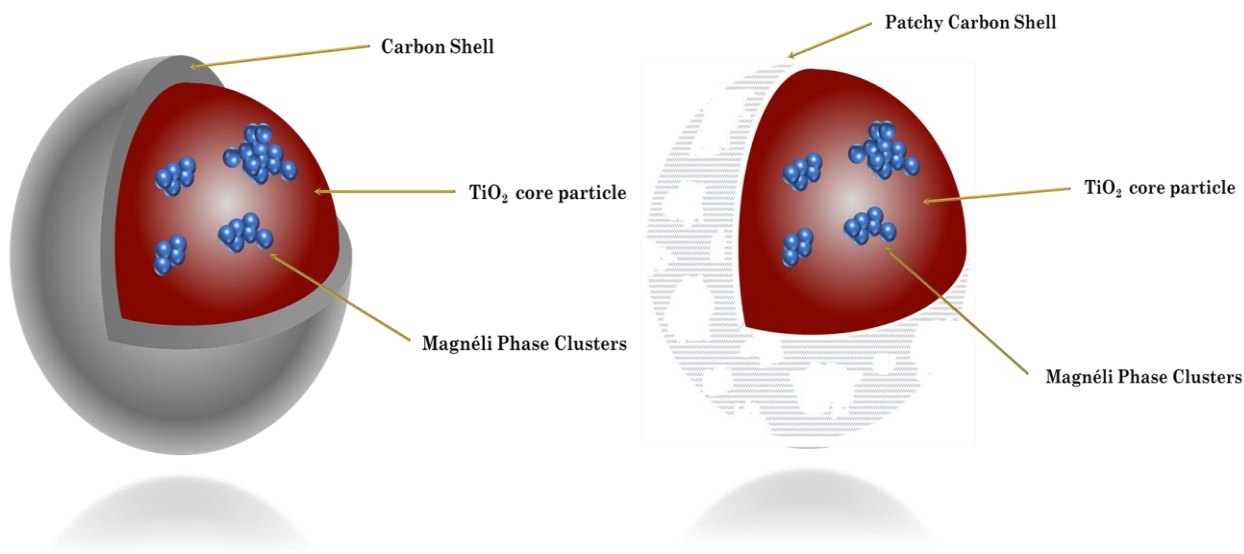


Figure 3.24. Left: High acetylene flows lead to thick carbon-shells like material 1323. Right: Low acetylene flows lead to "patchy" shells like material 1479. Carbothermal treatment improves the degree of graphitization in the thick shell case whereas mends the "patchy" shell with defective carbon species. The acetylene gas serves both as carbon-shell source and as a reductive agent. As a result, Magnéli phase clusters can form near the surface of the particle.

3.6 – Electron Paramagnetic Resonance (EPR) Results

Electron paramagnetic resonance (EPR) is a powerful tool to probe electronic properties of paramagnetic species like carbon-based materials and metal oxide nanoparticles. Information can be extracted concerning the presence of electrons and holes at the bulk or surface of the material as well as the detection of radical generation on the surface of the material. Herein, we employed EPR spectroscopy to investigate the defects created on the carbon-coated nanoparticles as well as to monitor the radical generation.

3.6.1 – EPR Analysis of Pristine and Calcined Materials

In titanium oxide, electrons formed by photoexcitation are trapped by Ti^{4+} ions, forming Ti^{3+} ions. The sites responsible for the stabilization of the holes in metal oxides like in our case TiO_2 are the oxygen ions of the lattice O^{2-} that form paramagnetic $\text{O}^{\cdot-}$ paramagnetic species.



It is therefore understandable that the nature, location (lattice or surface) and features of the charge traps are issues of vital importance. Giamello *et al*¹¹⁰ examined the charge carrier separation as well as the stabilization of the electrons in TiO_2 particles. Fig. 3.25 presents EPR spectra recorded at 77K for the TiO_2 polymorphs anatase and rutile. In anatase, we can detect two main paramagnetic species attributed to Ti^{3+} ions. The first one is an axial signal (signal I) with $g_{\parallel} = 1.992$ and also $g_{\perp} = 1.964$ that has been ascribed to regular lattice sites in the anatase matrix. The second one (signal II) is a broad signal centered at $g = 1.93$ and is ascribed to Ti^{3+} centers close to the surface. The broad linewidth suggests the presence of not-well localized Ti^{3+} centers and the presence of a disordered environment commonly encountered at the surface of nanomaterials.

In the rutile case, we again have two main paramagnetic species emerging upon UV illumination. The first one, is a rhombic signal with $g_1 = 1.970$, $g_2 = 1.961$ and $g_3 = 1.948$ that has been ascribed (signal III) to Ti^{3+} centers at surface of the crystals. The second signal, with a rhombic symmetry (signal IV) with $g_1 = 1.966$, $g_2 = 1.961$ and $g_3 = 1.948$ has been ascribed to Ti^{3+} centers of the bulk rutile structure.

3.6.1 – EPR Analysis of Pristine and Calcined Materials

Fig. 3.25 also presents commercial P25 EPR spectra, that has been a reference material in the field of photocatalysis. P25 is a mixed phase photocatalyst and the signal upon UV illumination can be interpreted as the overlap signals of Ti^{3+} centers from both anatase and rutile polymorphs.

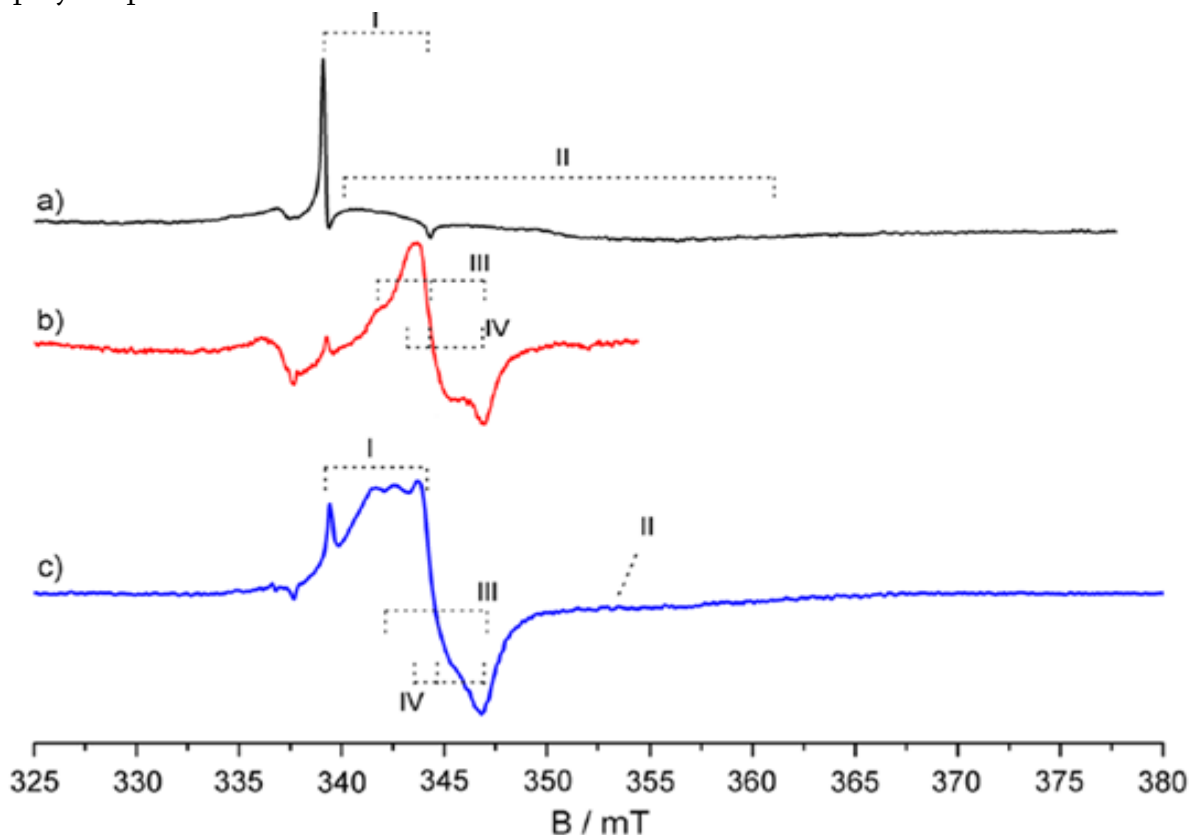


Figure 3.25. CW EPR spectra of (a) anatase, (b) rutile and (c) P25 recorded upon UV illumination at 77K in vacuum. The overlap between anatase and rutile signals is evident in mixed phase P25¹¹⁰.

So far, we have only referred to the Ti^{3+} centers. The sites responsible for the stabilization of the holes are the O^- centers. Nakaoka *et al*¹¹¹ studied the nature and the location of these hole trapping sites. They were able to correlate the signals from TiO_2 anatase particles under UV illumination with the hole trapping sites as well as the hole trapping sites location at the bulk or at the surface of the crystal. They also ascertained the difficulty to produce radicals in rutile TiO_2 powder, corresponding to the poor photocatalytic activity of most rutile powders.

In order to mitigate the poor photocatalytic activity of rutile, most photocatalysts are mixed-phase. Hurum *et al*⁵⁷ examined the synergetic effect of the mixed-phase P25 catalyst, where the rutile does only act as a passive electron sink, but also facilitates stabilization of

3.6.1 – EPR Analysis of Pristine and Calcined Materials

charge through electron transfer at lower energy anatase lattice trapping sites. Therefore, rutile should not be sidelined in photocatalytic applications but must act synergistically. Table 3.5 summarized the g-values for electron and hole trapping sites for both polymorphs.

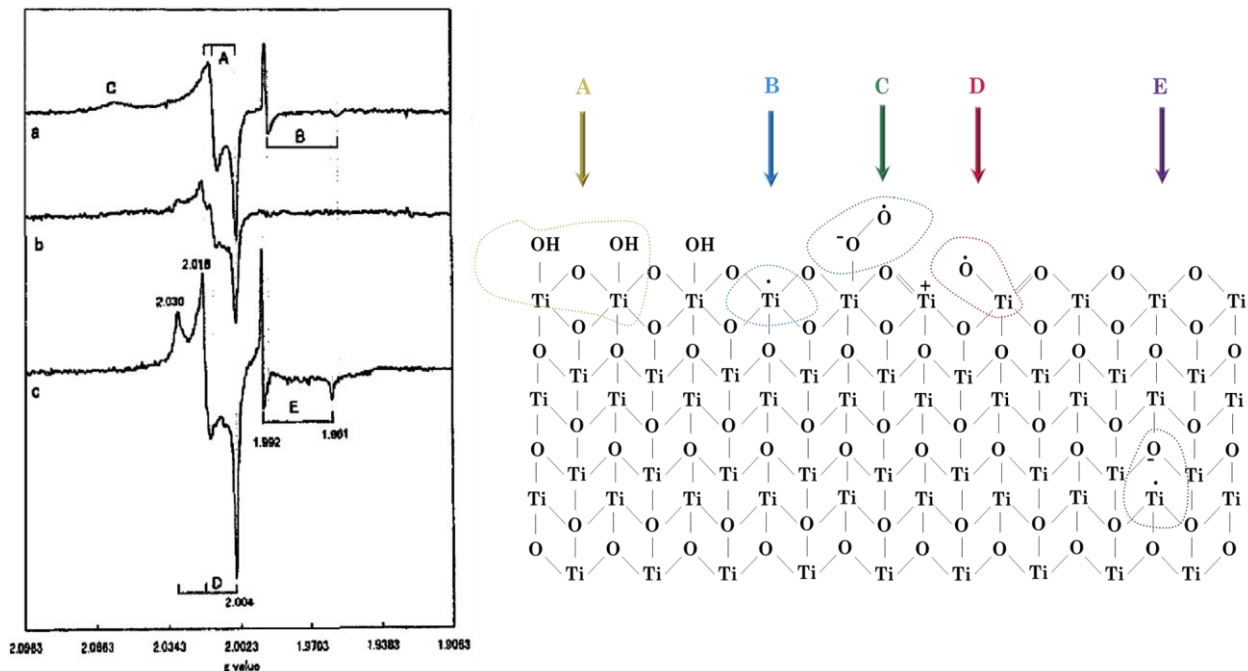


Figure 3.26. Left: EPR spectra of TiO₂ powder upon UV irradiation at 77K for (a) unheated , (b) heated at 350°C for 5h and (c) heated at 700°C for 5h. Right: Plausible chemical structure of the radicals observed on anatase TiO₂. A: trapped hole with OH⁻ group; B: surface trapped electron; C: adsorbed superoxide radical; D: surface trapped hole; E: inner trapped electron¹¹¹.

Species	Anatase			Rutile		
Ti ³⁺	$g_{\perp} = 1.990$	$g_{\parallel} = 1.957$ (lattice)		$g_{\perp} = 1.975$	$g_{\parallel} = 1.940$ (lattice)	
O ⁻	$g_{\perp} = 2.012$	$g_{\parallel} = 2.004$		$g_{\perp} = 2.016$	$g_{\parallel} = 2.002$	
O ²⁻	$g_1 = 2.003$	$g_2 = 2.008$	$g_3 = 2.019$	$g_1 = 2.003$	$g_2 = 2.008$	$g_3 = 2.022$

Table 3.5. G-value parameters of the paramagnetic centers for rutile and anatase polymorphs^{112,113}.

3.6.1 – EPR Analysis of Pristine and Calcined Materials

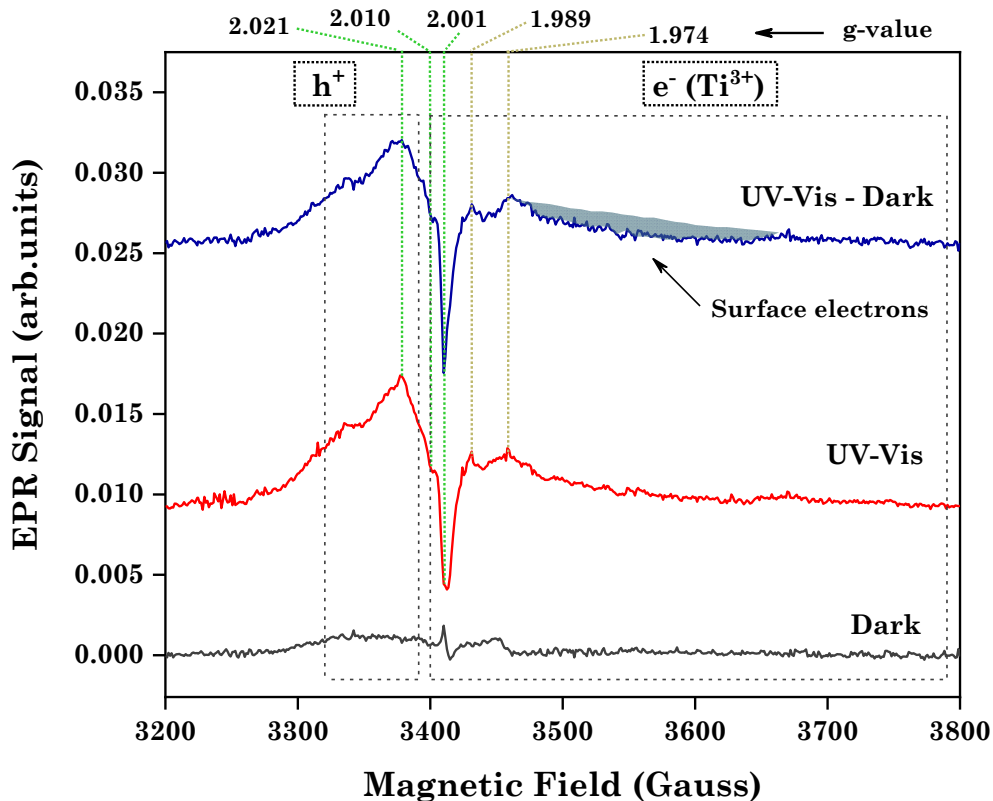


Figure 3.27. EPR spectrum of material 1290 before and upon UV-Vis irradiation.

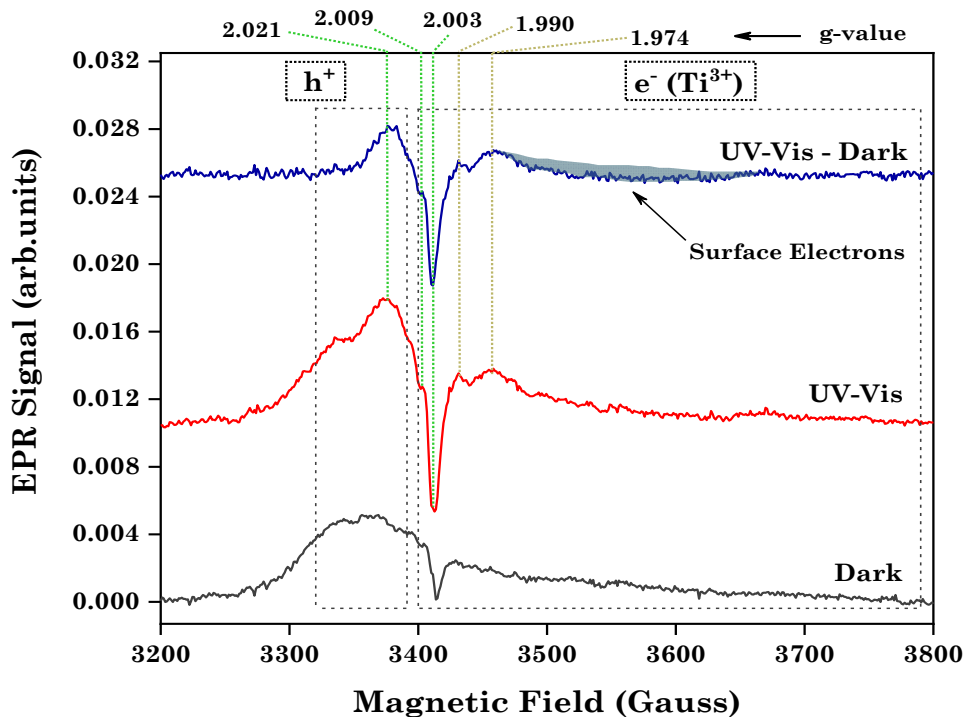


Figure 3.28. EPR spectrum of material 1290 upon calcination at 350°C before and upon UV-Vis irradiation.

3.6.1 – EPR Analysis of Pristine and Calcined Materials

Starting our analysis from the TiO₂ 1290 pristine material as shown in Fig. 3.27, we can detect an axial signal close to $g \sim 2$ which can be attributed to hole trapping sites. The corresponding g -values are in good accordance with those in the literature. The “shoulder” at the signal observed close to $g = 2.021$ is the result of the interaction between surface Ti³⁺ with the atmosphere, probably during the degassing process. As far as the Ti³⁺ centers are concerned, the g -values for anatase at $g = 1.989$ and rutile at $g = 1.974$ respectively are in good accordance with the literature. One might also observe a broad signal beginning after the rutile signal which can be attributed to delocalized electrons that are close to the surface.

Analogously, comparing the 350°C 1290 material as shown in Fig. 3.28 with its pristine counterpart, the trend seems to be the same. The broad shoulder on the dark scan as before is attributed to the interaction of surface Ti³⁺ with the atmosphere. The g -values for the hole trapping sites as well as the lattice rutile and anatase electrons are once more in good accordance with the literature. Surface electrons are also present indicated by the broad signal ranging after the rutile signal.

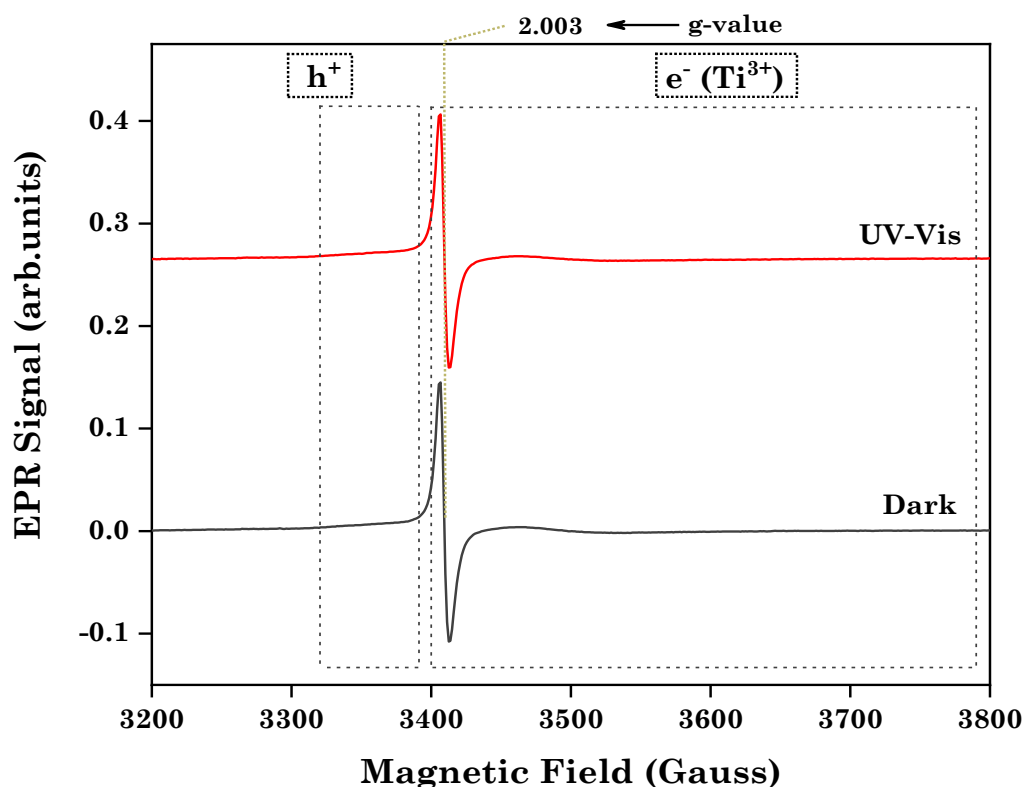


Figure 3.29. EPR spectrum of pristine 1323 before and upon UV-Vis irradiation.

The trend observed in 1290 material and its calcined counterpart, is not followed in pristine 1323 material. As we can see in Fig. 3.29, a sharp axial signal with a g -value at $g = 2.003$ appears and which can either be defect-related or carbon-related. We can see that the

3.6.1 – EPR Analysis of Pristine and Calcined Materials

signal before and upon illumination remains intact. This can be attributed to the presence of a thick carbon shell as it had been proposed earlier in the analysis. The carbon shell, absorbs the incident radiation due to its thickness, suppressing in this way charge separation at the core TiO_{2-x} material and as a result hindering the photocatalytic efficiency since the material is non-photoactive.

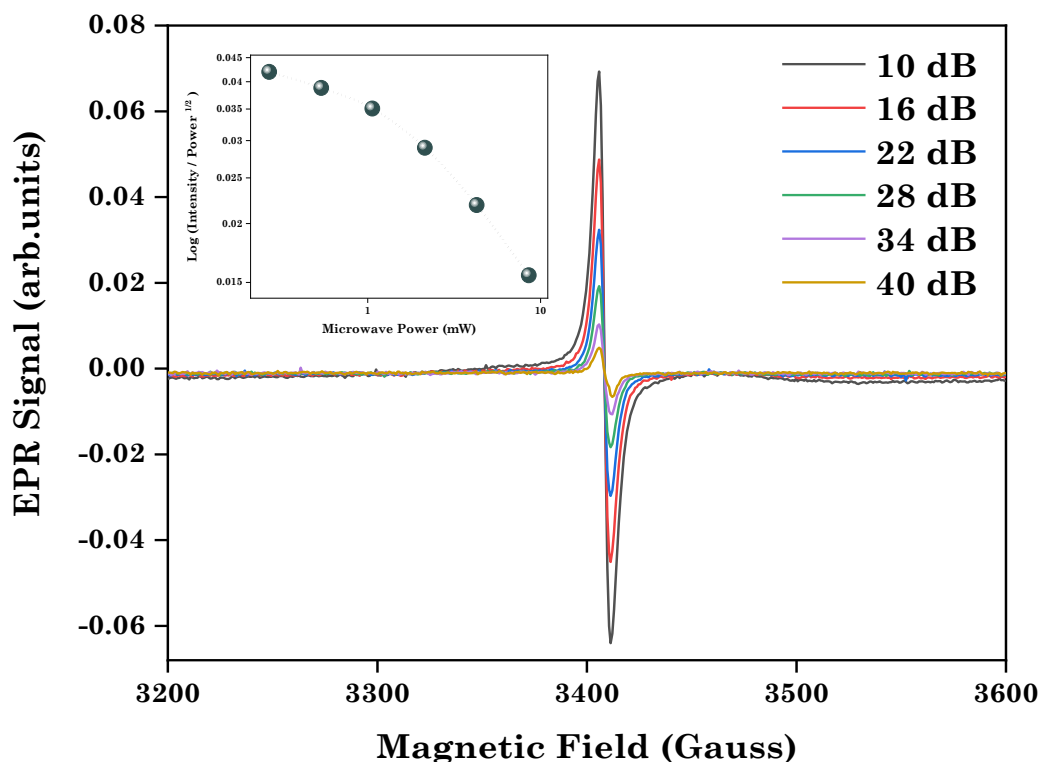


Figure 3.30. $P_{1/2}$ study of the symmetric signal at $g \sim 2$ for the pristine 1323 material.

The above claim can be verified by examining the saturation of the signal. Since carbon behaves as a radical, we expect the signal to saturate. By examining the signal intensity as a function of the microwave power, we can verify the saturation of the signal. The high intensity of the signal is attributed to the high carbon content on the carbon shell.

The 350°C-calcined 1323 material follows the same trend as its pristine counterpart, as we can see in Fig. 3.31. Like material 1323, the sharp axial signal is close to $g \sim 2$ and the signal before and upon illumination does not change. DRS results suggested minimal absorption that was attributed to the presence of a thick carbon shell. Examination of the saturation of the signal as shown in Fig. 3.32, once more reveals the presence of carbon with a decrease in the signal intensity, probably due to the improved graphitization of the shell of the calcined material.

3.6.1 – EPR Analysis of Pristine and Calcined Materials

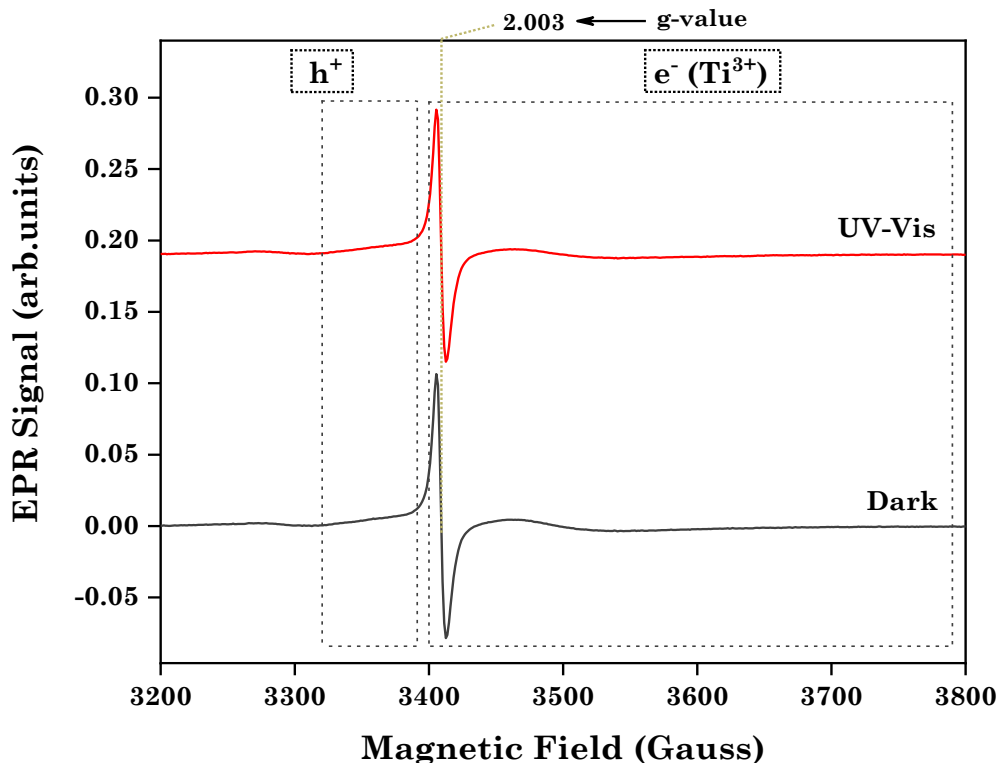


Figure 3.31. EPR spectrum of material 1323 upon calcination at 350°C before and upon UV-Vis irradiation.

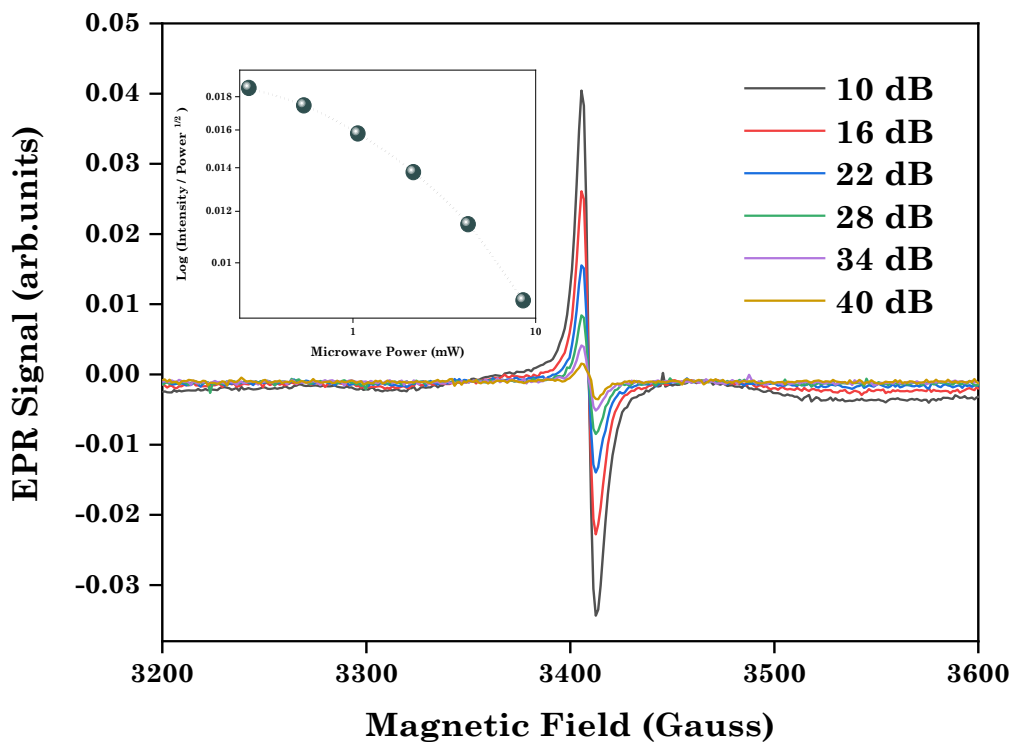


Figure 3.32. P_{1/2} study of the symmetric signal at g~2 for the 350°C-calcined 1323 material.

3.6.1 – EPR Analysis of Pristine and Calcined Materials

The intermediate material between the fully oxide TiO₂ 1290 material and the thick carbon-coated TiO_{2-x}@C 1323 material is material 1479. If we have a look at Fig. 3.33, the trend is a little bit different than that encountered in material 1323. The sharp axial signal at $g \sim 2$ exists but this time, the signal changes upon irradiation. Houlihan *et al*¹¹⁴ have reported similar lineshapes with an axial signal around $g \sim 2$ for different Magnéli phase polymorphs. They correlated the linewidth of each signal with each one of the Magnéli phases. The shorter linewidths corresponded to the higher Ti³⁺ concentration that is the Ti₂O₃ polymorph. Let us not forget that titanium suboxides are mixed-valence compounds with two Ti³⁺ ions (3d¹ electronic configuration) and (n-2) Ti⁴⁺ ions (3d⁰ electronic configuration) (n being the number on the formula Ti_nO_{2n-1}). Since the linewidth in our signals is relatively short, we believe that we have nano-clusters of Ti₂O₃ and Ti₃O₅ located near the surface of the carbon shell since they cannot be detected by means of XRD. While the Magnéli phase titanium suboxides have Ti³⁺ ions at interstitial positions, they also exhibit high conductivity close to that of graphite. Therefore, they should ease charge migration to the surface at photocatalytic applications.

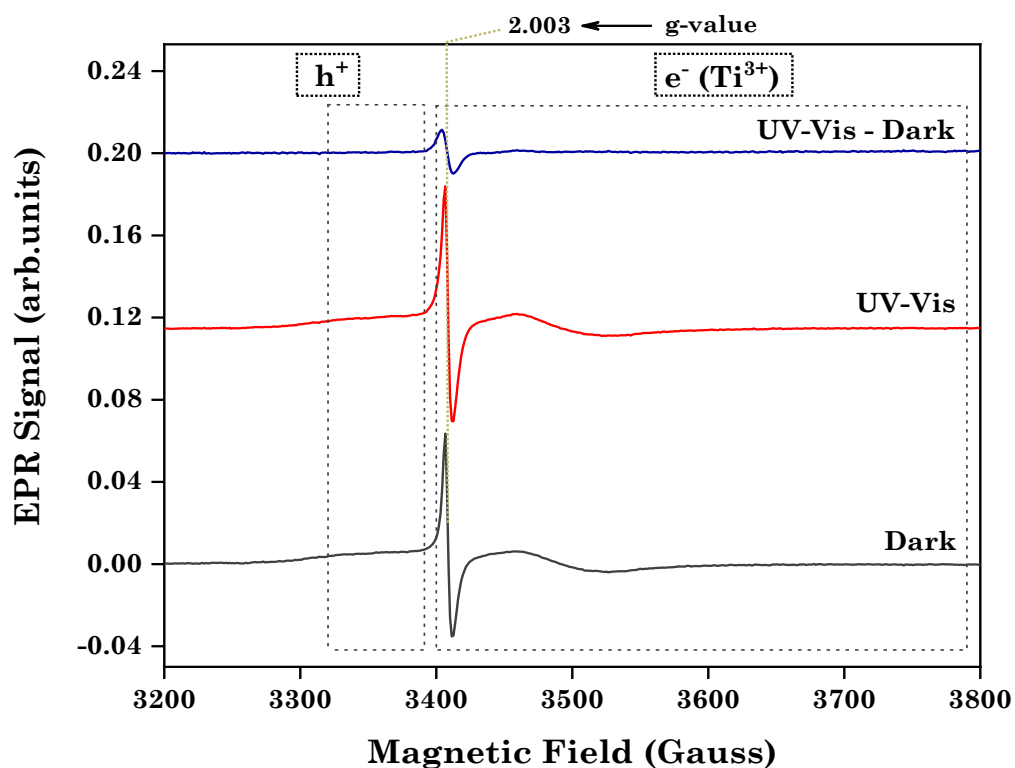


Figure 3.33. EPR spectrum of pristine 1479 before and upon UV-Vis irradiation.

3.6.1 – EPR Analysis of Pristine and Calcined Materials

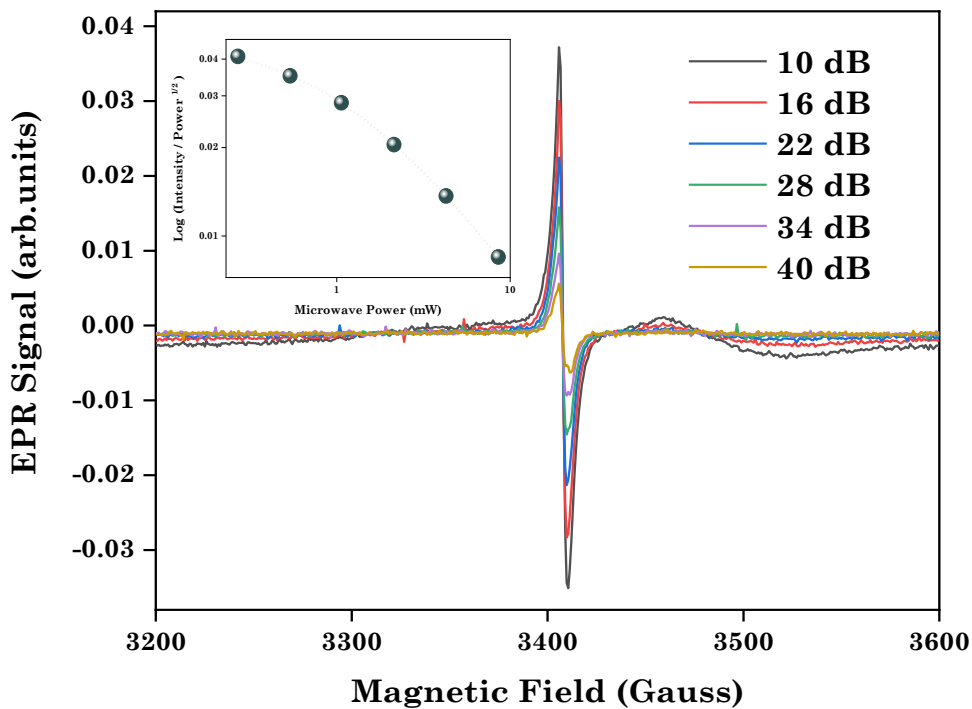


Figure 3.34. $P_{1/2}$ study of the signal at $g \sim 2$ for the pristine 1479 material.

The signal intensity at material 1479 is smaller than that in pristine and calcined 1323 material. In Fig. 3.34 we can see the saturation of the signal which is consistent with our hypothesis.

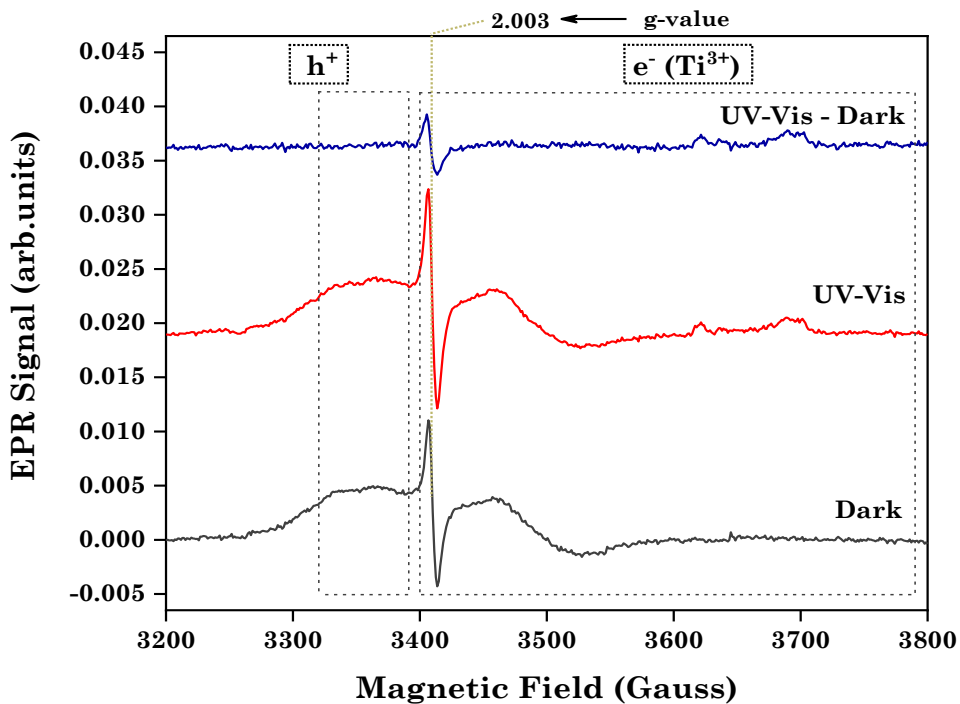


Figure 3.35. EPR spectrum of material 1479 upon calcination at 350°C before and upon UV-Vis irradiation.

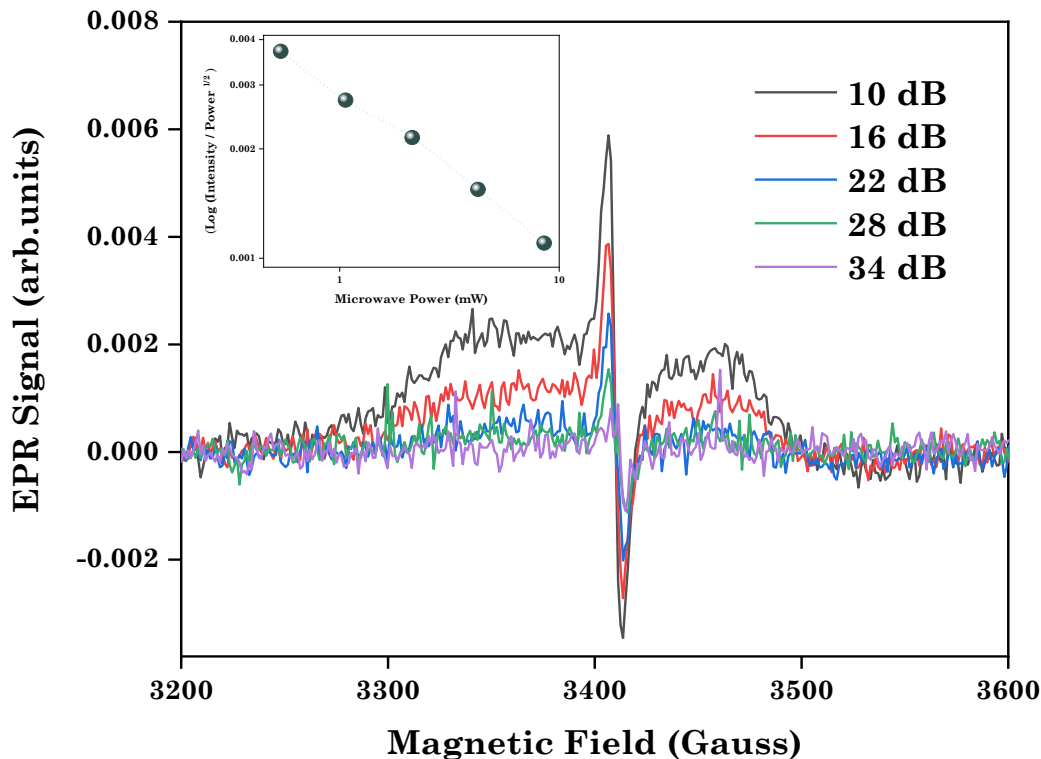


Figure 3.36. $P_{1/2}$ study of the symmetric signal at $g \sim 2$ for the 350°C-calcined 1479 material.

The 350°C-calcined 1479 material's lineshape resembles to that of the pristine 1479 material. The shoulder before the axial signal at $g = 2.003$ is as stated before attributed to the interaction of surface Ti^{3+} with the atmosphere. The axial signal however saturated earlier and this perhaps is due to the fact that the carbon-content in the 350°C carbon-coated 1479 material increased upon carbothermal treatment. The signal is a convolution of the carbon radical and the actual Magnéli phase signal.

By summarizing the above analysis, we came to the conclusion that the thick carbon-coated 1323 material is non-photoactive due to the extended presence of carbon species that block charge separation, while the “patchy”-coated 1479 material is shown to be photoactive, and we were able to verify the signal of the Magnéli phase clusters as we had proposed earlier in the analysis. The actual test of the efficacy of the “patchy” shelled 1479 material will be the photoinduced radical generation in order to ascertain if the patchy shell facilitates photocatalytic applications or trammels the process. Also, the radical monitoring will shed light to the role of the nanoclusters as far as charge transfer is concerned.

3.6.2 – Photoinduced Radical Monitoring

A preliminary test of the photocatalytic efficiency of the nanomaterials is the monitoring of the radical generation upon the nanoparticles surface. Those radical intermediates can be monitored using the EPR spin trapping technique as discussed in Chapter 2. DMPO spin trapping experiments with TiO₂ particles are known for their high yield¹¹⁵ in hydroxyl radicals (OH·).

The procedure that was for the spin trapping experiments is summarized in Fig. 3.37. DMPO was used as the spin trap. 2 mg of nanoparticles were dispersed in 4 mL of MilliQ water and sonicated for 10 minutes. 450 µL of the aqueous solution was mixed with 50 µL of DMPO and 15 µL of those were placed in each one of the two capillaries.

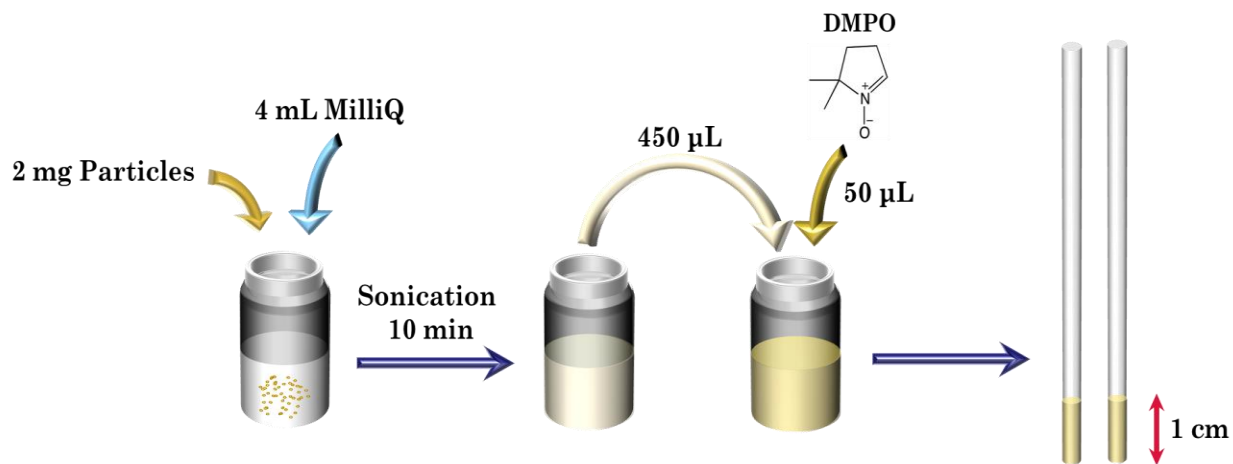


Figure 3.37. Schematic representation of the spin trapping experiment.

P25 was used as our reference material, given the superb photocatalytic efficiency the material exhibits. In Fig. 3.38 we present the spectrum of the radical monitoring for the reference sample P25. The high yield is evident with the maximum photoinduced OH· radicals being 164 µmol g⁻¹ h⁻¹, without the generation of different type of radicals. Fig. 3.39 presents the pristine 1290 material, which is the flame-made TiO₂ with common characteristics with P25. We can see that the yield is decreased, namely 95 µmol g⁻¹ h⁻¹ again without the presence of different type of radicals. Despite the fact that the SSA of P25 is close to 50 m²/g whereas in pristine 1290 the SSA is double this figure, the yield was nearly twice as much of the pristine 1290 in P25.

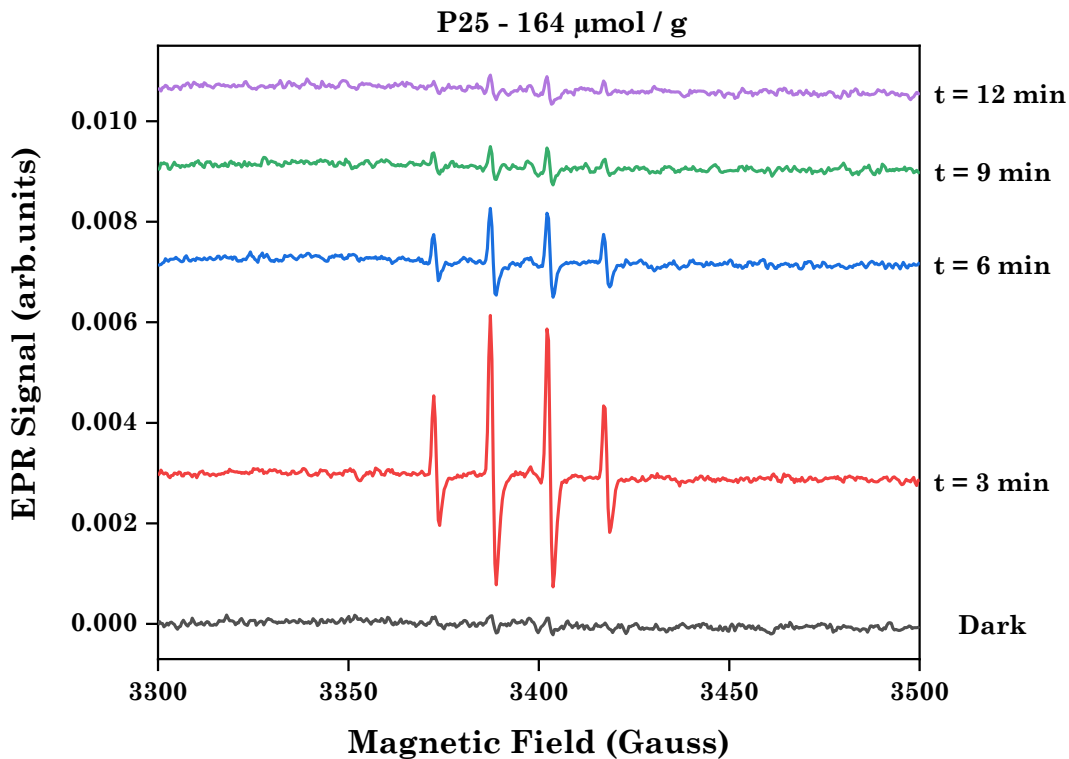


Figure 3.38. Radical generation monitoring using DMPO for reference material P25.

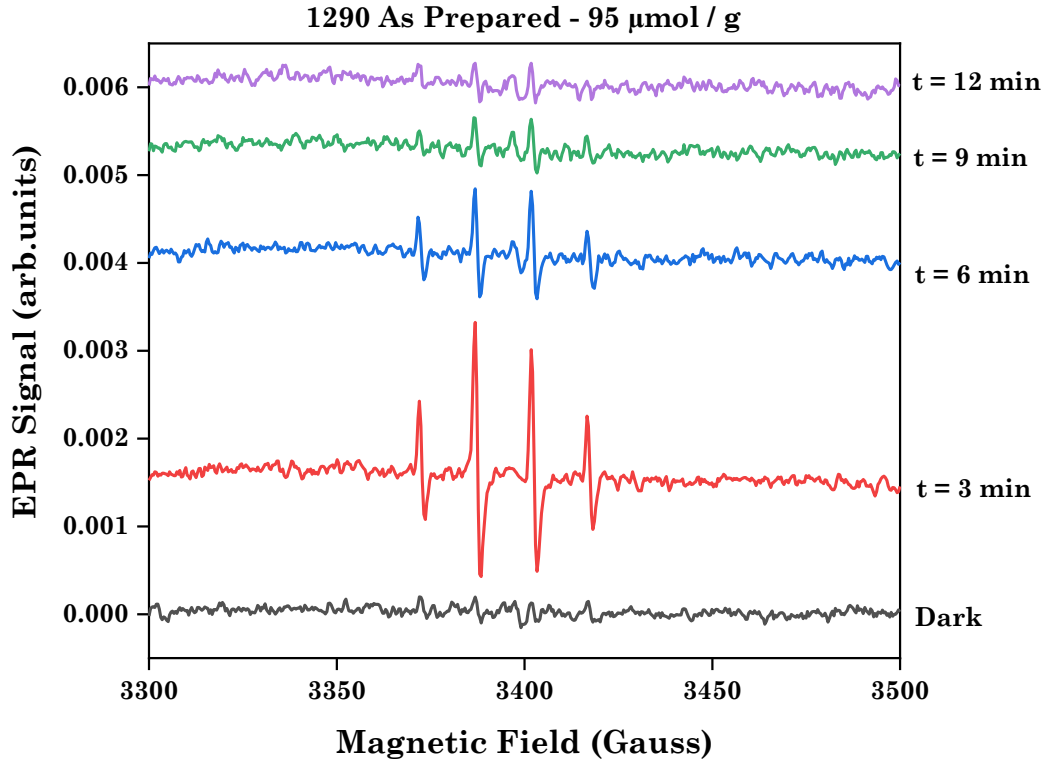


Figure 3.39. Radical generation monitoring using DMPO for pristine 1290 material.

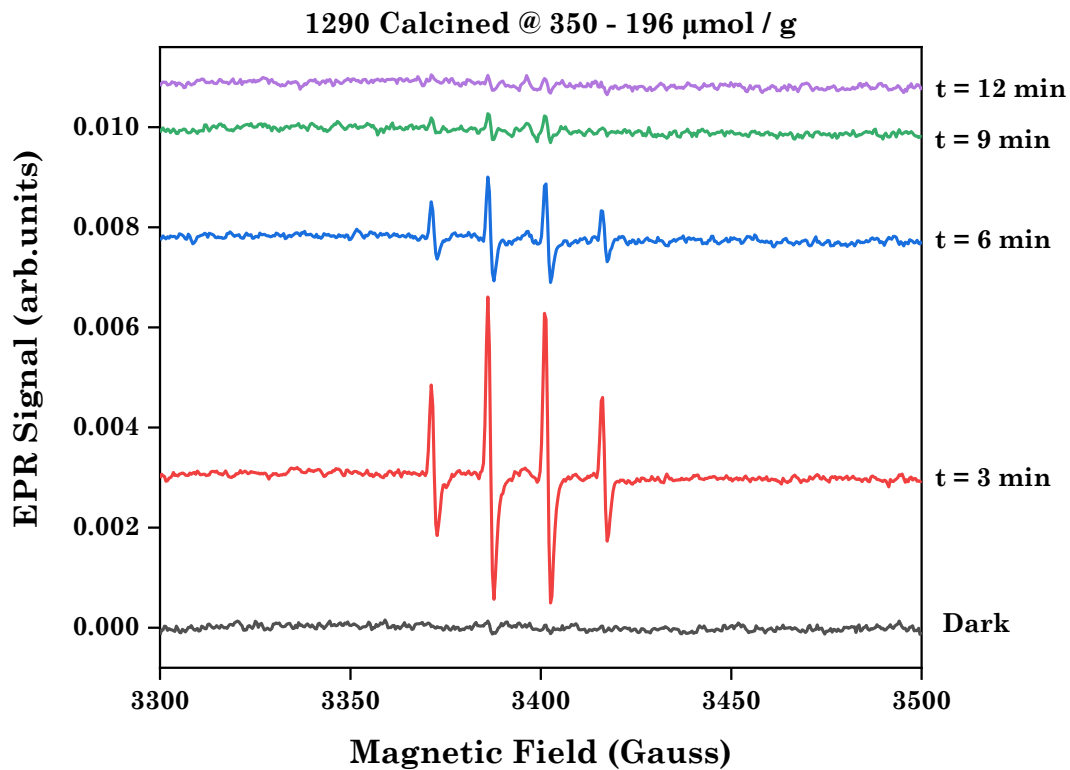


Figure 3.40. Radical generation monitoring using DMPO for the 350°C-calcined 1290 material.

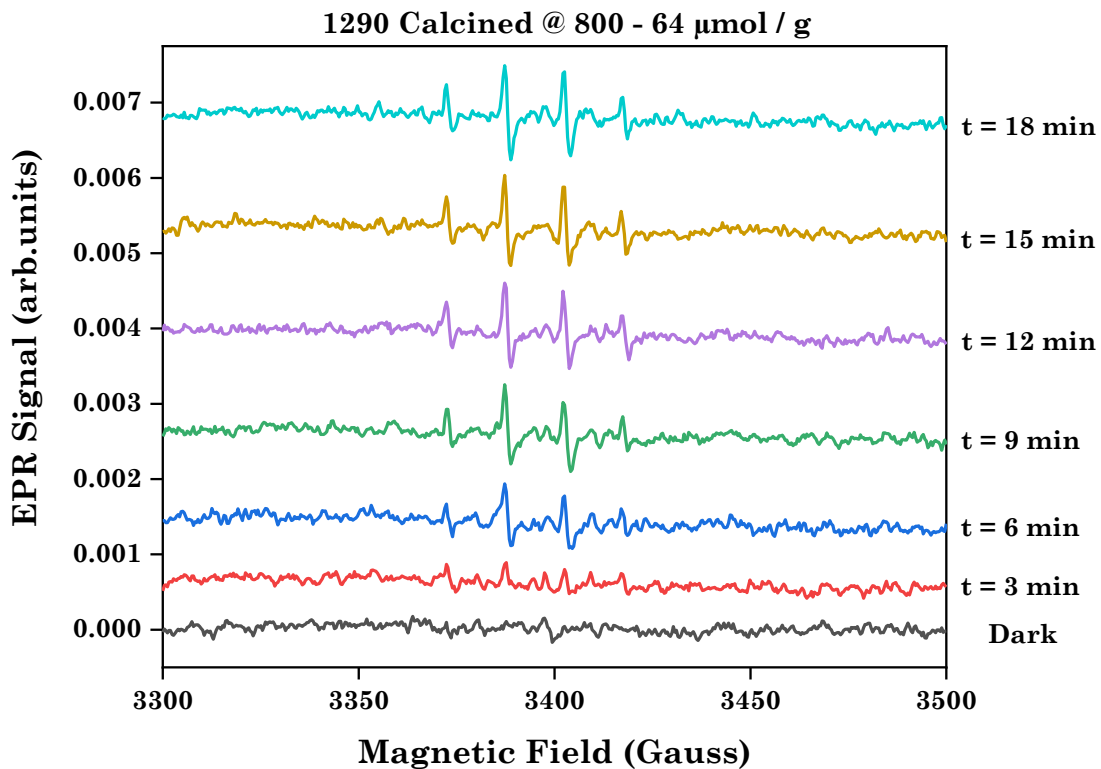


Figure 3.41. Radical generation monitoring using DMPO for the 800°C-calcined 1290 material.

3.6.2 – Photoinduced Radical Monitoring

The 350°C and the 800°C calcined 1290 material show a very different behavior. The 1290@350 material, shown in Fig. 3.40, excels in photoinduced OH⁻ radical generation with a maximum output of 196 $\mu\text{mol g}^{-1} \text{h}^{-1}$. The carbothermal treatment with CH₄ lead to mild reduction of the surface which as a result boosted the radical generation. On the contrary, the 1290@800 material, shown in Fig. 3.41, performed poorly on the radical generation. We detected a small number of superoxide radicals. This can be attributed to the extended defective carbon species deposition during carbothermal treatment which made the material non-photoactive and thus suppressed the core particles efficiency in photocatalytic applications.

The radical generation in the pristine 1323 and the calcined ones is a bit different than those of the reference P25 and 1290. As shown in Fig. 3.42, the pristine 1323 does not perform efficiently in terms of radical generation with just 65 $\mu\text{mol g}^{-1} \text{h}^{-1}$. Also, we can detect the presence of a few superoxide radicals (OOH⁻) which is possibly inducted by the presence of carbon. Upon calcination at 350°C, the 1323@350 material shown in Fig. 3.43, boosts the radical generation reaching a worth mentioning maximum of 102 $\mu\text{mol g}^{-1} \text{h}^{-1}$ hydroxyl radicals. The interesting in this case is however that the radical generation kept on going up for more minutes in contrary to the TiO₂ 1290 and 1290@350 material in which the radical generation deteriorated and almost seized after the 10 minute mark. The 1323@800 shown in Fig. 3.44, delivers 65 $\mu\text{mol g}^{-1} \text{h}^{-1}$ just like the pristine material with differences in the duration of the radical generation.

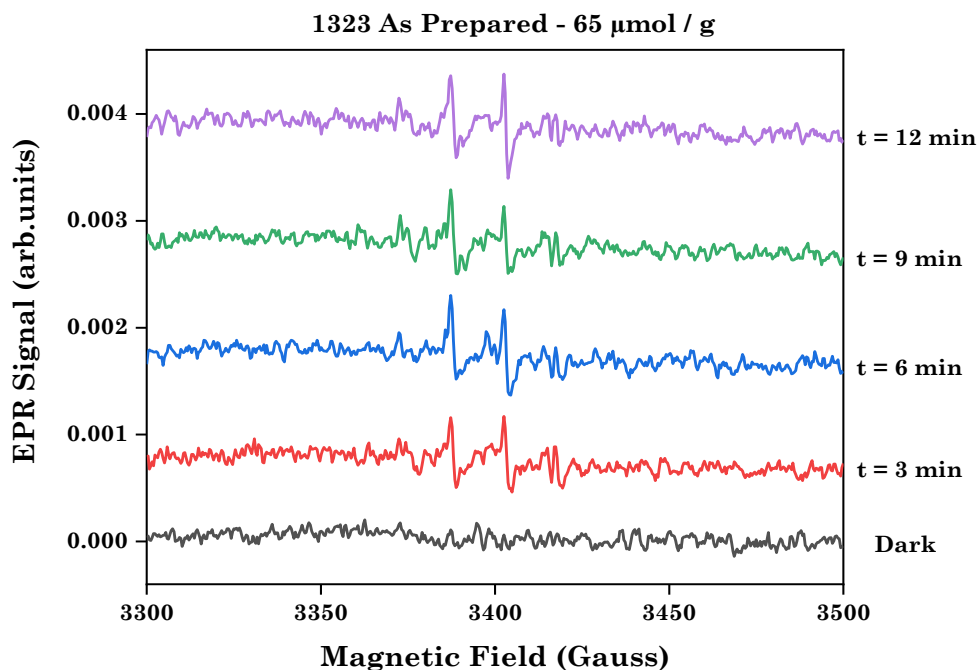


Figure 3.42. Radical generation monitoring using DMPO for pristine 1323 material.

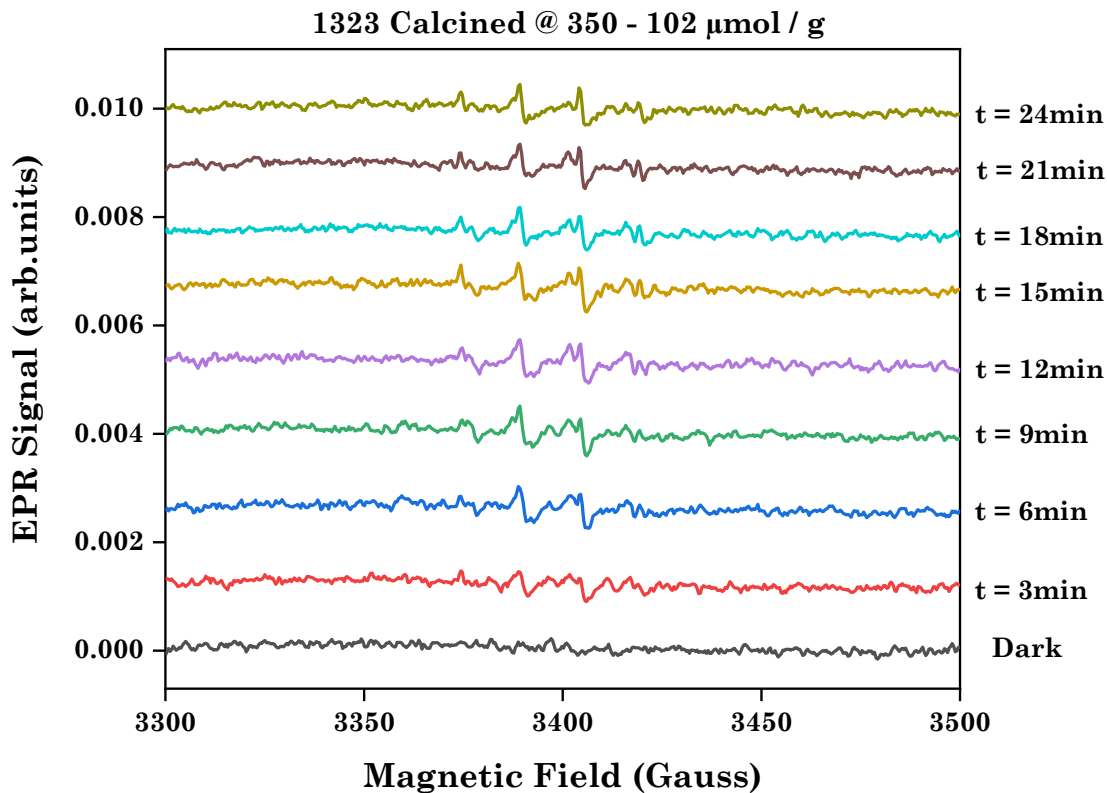


Figure 3.43. Radical generation monitoring using DMPO for the 350°C-calcined 1323 material.

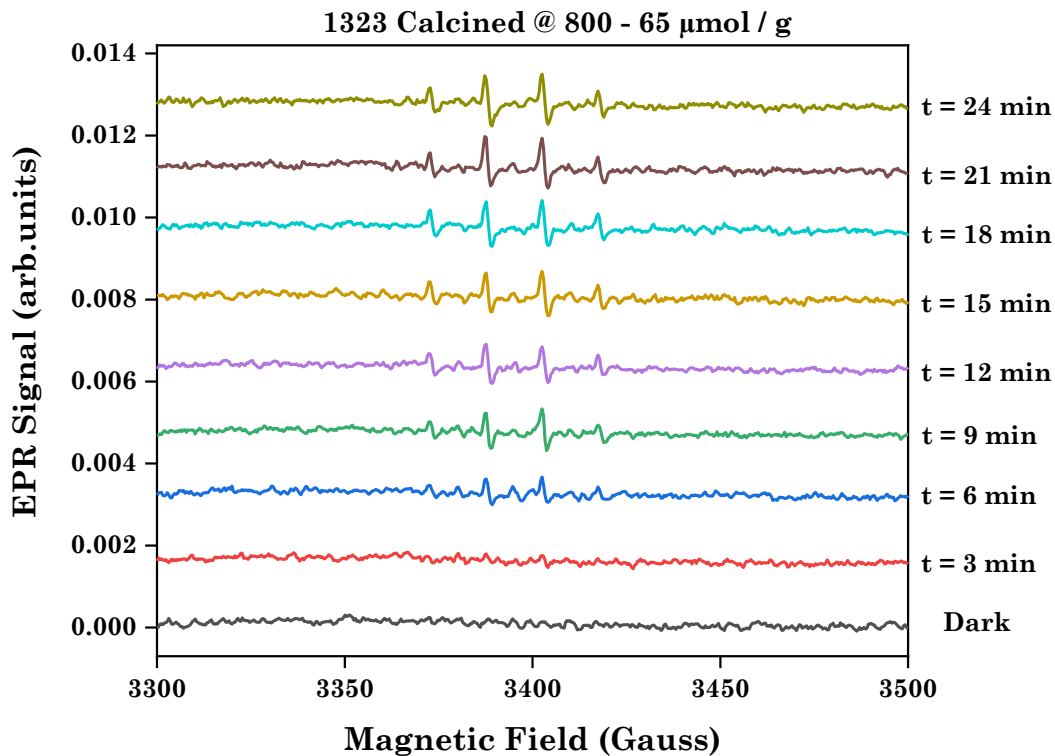


Figure 3.44. Radical generation monitoring using DMPO for the 800°C-calcined 1323 material.

3.6.2 – Photoinduced Radical Monitoring

The most anticipated material about its photocatalytic efficiency certainly is material 1479. Anticipated in terms of how the “patchy” shell and the nanoclusters of Magnéli phase TiO_{2-x} suboxides will influence the outcome. Astonishingly, pristine 1479 material shown in Fig. 3.45, performed superbly in radical generation with a maximum output of $161 \mu\text{mol g}^{-1} \text{h}^{-1}$ which is as much as our reference P25 material generates. Evidently, the nanoclusters facilitated the charge transfer to the surface, while the “patchy” carbon shell did not hinder the radical generation on the surface of the nanomaterial. In comparison with the TiO_2 1290 material, 1479 outperformed it with almost double the hydroxyl radical production. The 1479@350 material, shown in Fig. 3.46, seems to be affected by the carbon deposition during carbothermal treatment since the yield drops from $161 \mu\text{mol g}^{-1} \text{h}^{-1}$ to half of that at $77 \mu\text{mol g}^{-1} \text{h}^{-1}$. Similar behavior was observed in 1323 material in which the carbon mitigated radical generation. The same trend was observed for the 1479@800 material as shown in Fig. 3.47.

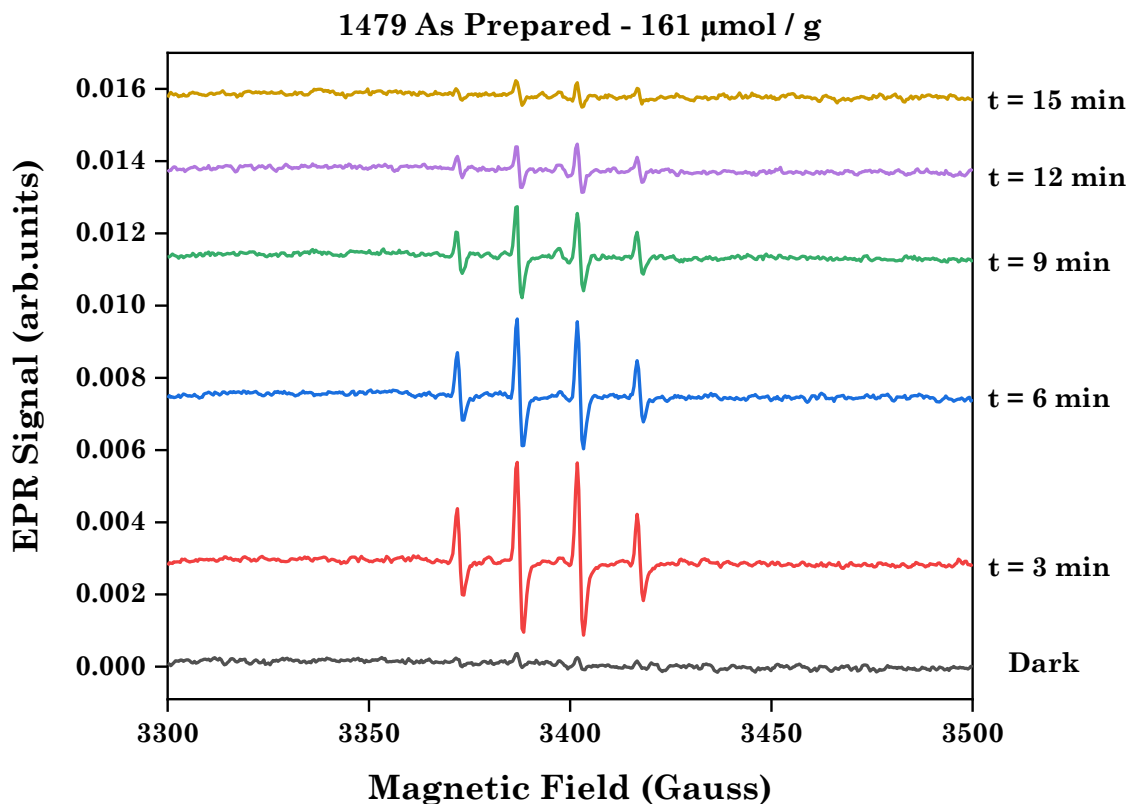


Figure 3.45. Radical generation monitoring using DMPO for pristine 1479 material.

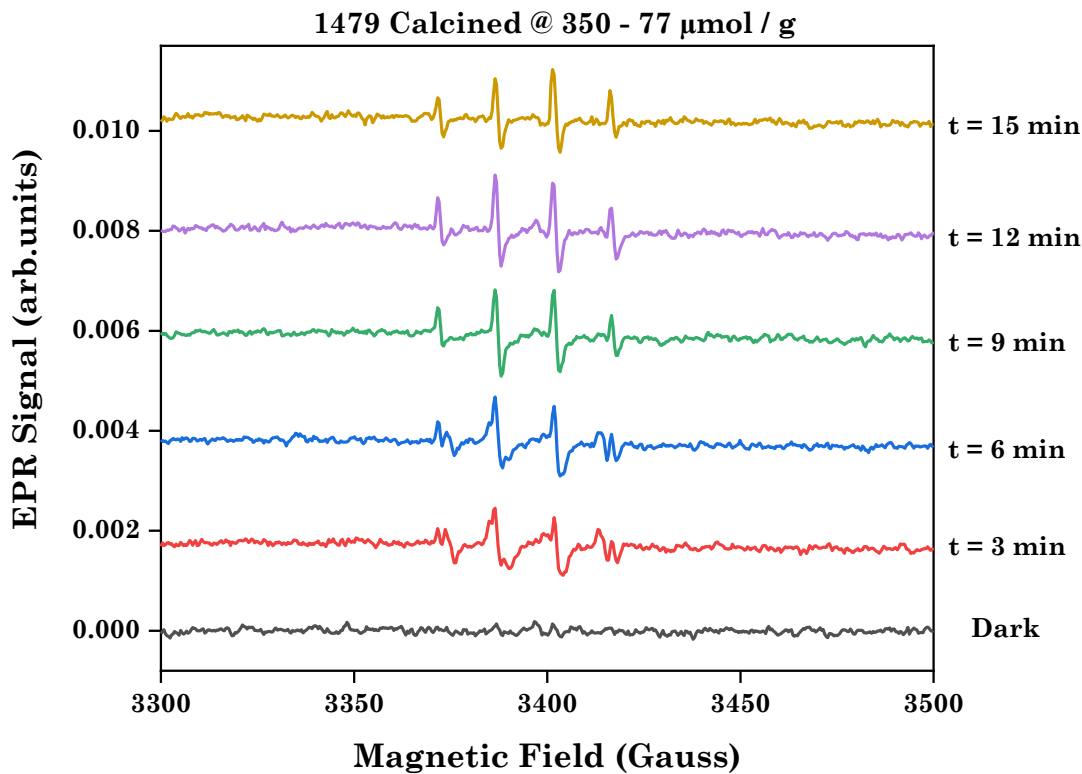


Figure 3.46. Radical generation monitoring using DMPO for the 350°C-calcined 1479 material.

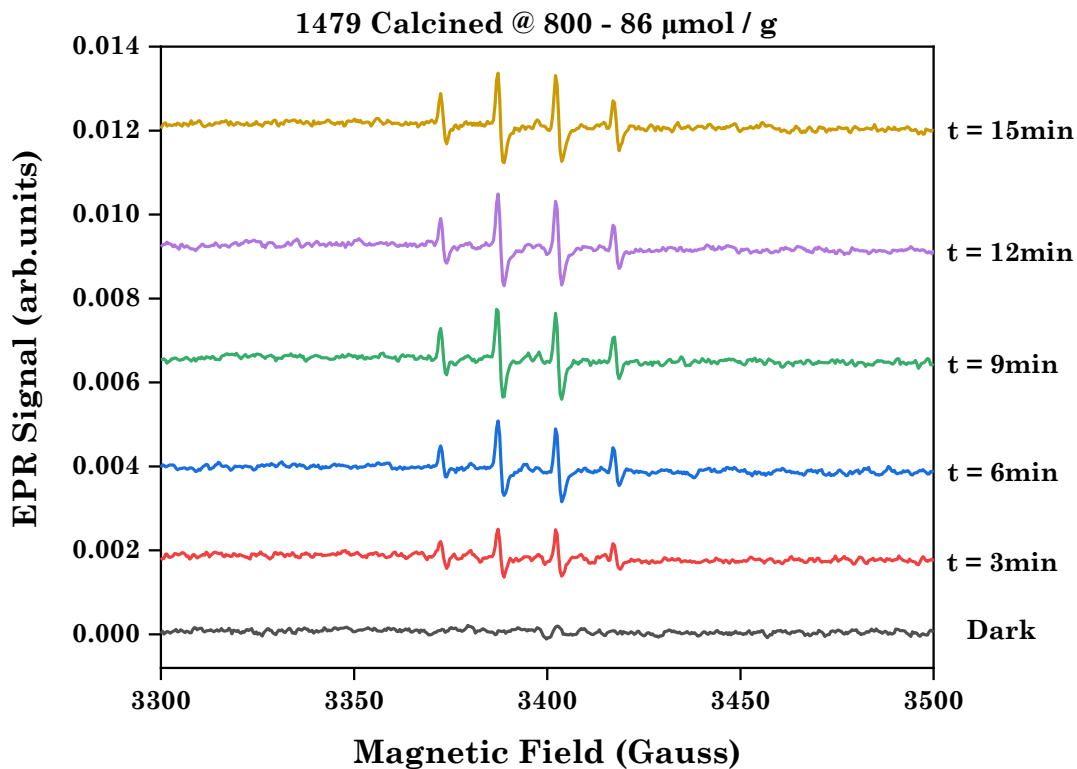


Figure 3.47. Radical generation monitoring using DMPO for the 800°C-calcined 1479 material.

3.6.2 – Photoinduced Radical Monitoring

The bar chart shown in Fig. 3.48 summarizes the maximum photoinduced OH⁻ radicals per sample.

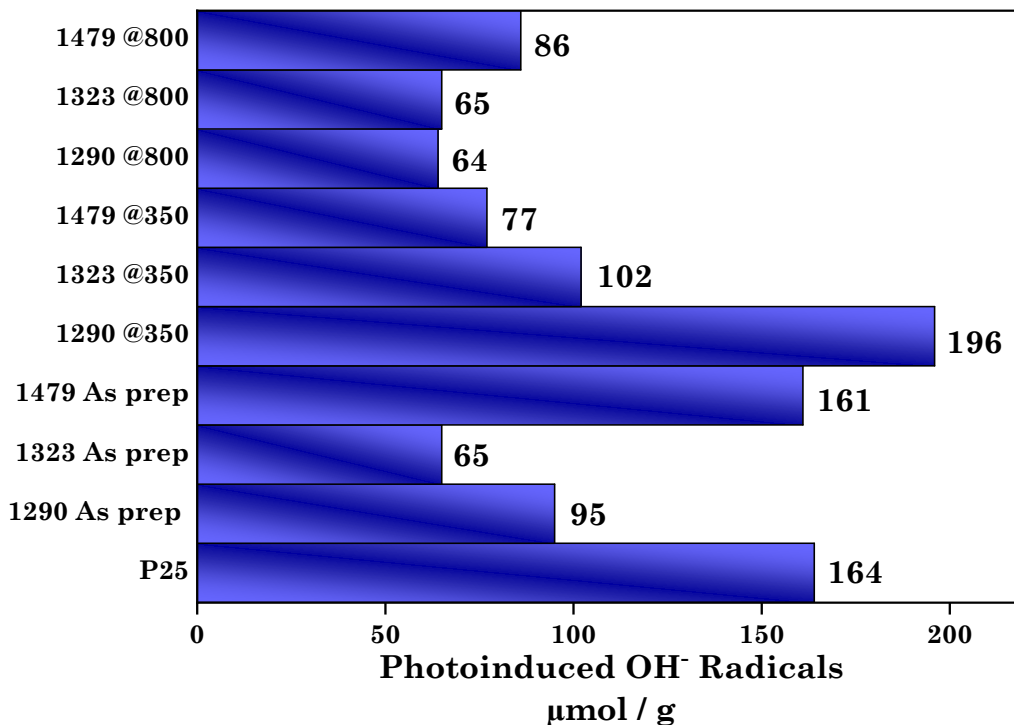


Figure 3.48. Maximum photoinduced OH⁻ radical generation per sample.

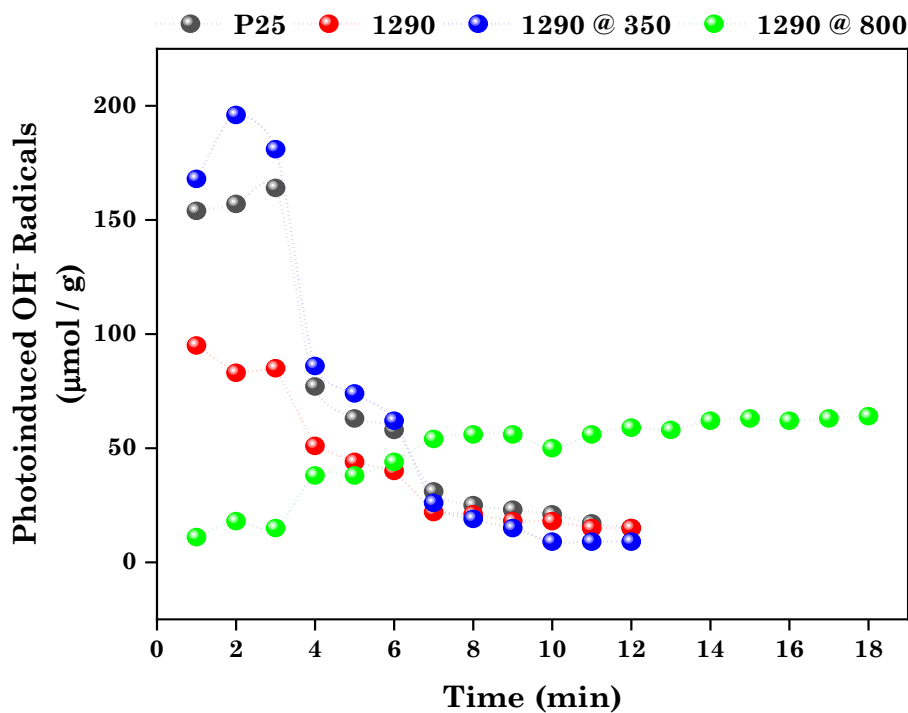


Figure 3.49. Kinetics of OH⁻ radical generation for reference P25, material 1290 and upon calcination.

3.6.2 – Photoinduced Radical Monitoring

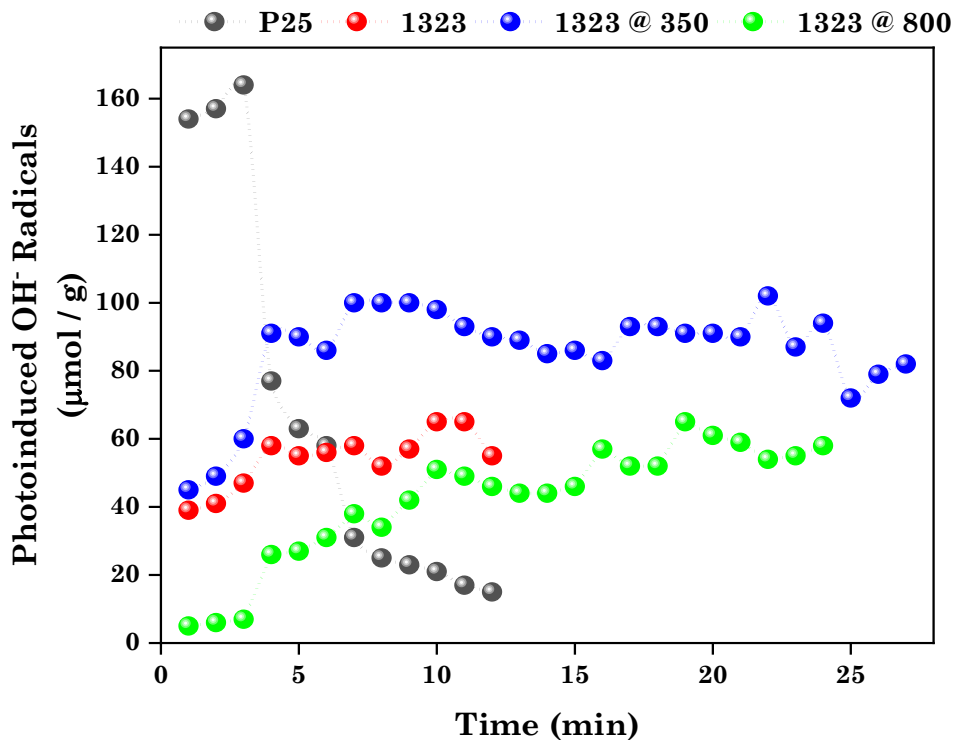


Figure 3.50. Kinetics of OH⁻ radical generation for reference P25, material 1323 and upon calcination.

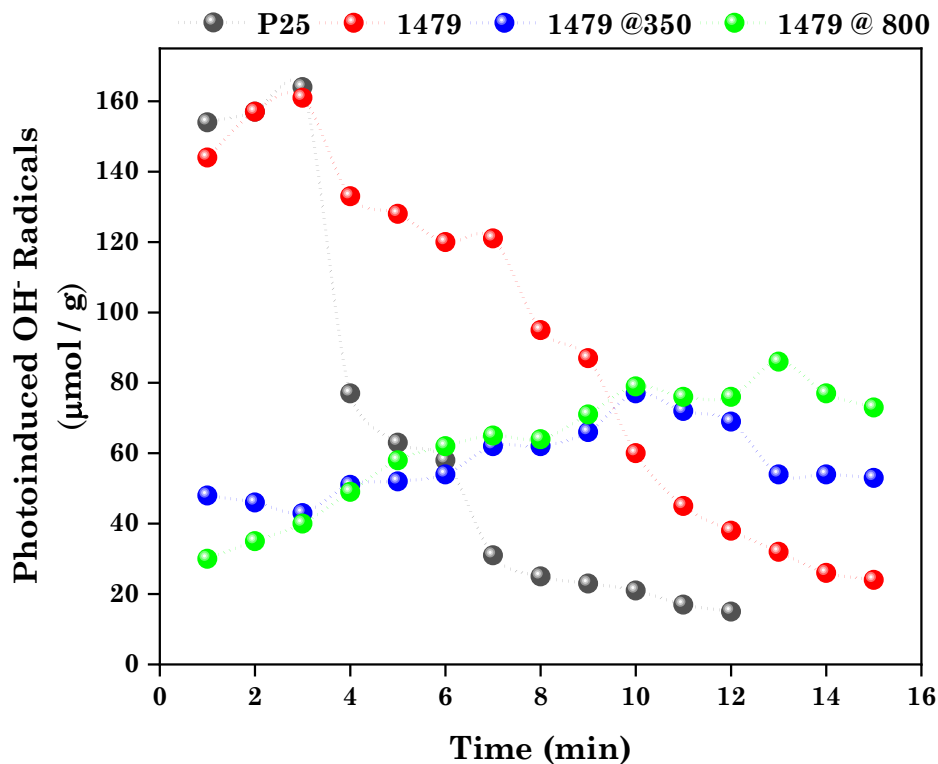


Figure 3.51. Kinetics of OH⁻ radical generation for reference P25, material 1479 and upon calcination.

3.6.2 – Photoinduced Radical Monitoring

The kinetics of the OH[•] radical generation is listed on Fig. 3.49, Fig. 3.50, and Fig. 3.51 for materials 1290, 1323 and 1479 pristine and upon calcination, respectively. It is worth mentioning that the carbon-coated pristine and calcined samples of 1323 and 1479 and the 1290@800 material all have a similar behavior as far as the way they produce the OH[•] radicals. More specifically, the kinetics of the aforementioned materials suggest that there is a constant production of OH[•] radicals in contrary to the P25 reference and the exception of 1479 pristine material. P25 and 1479, 1290 and 1290@350 showed a different behavior with a burst in hydroxyl radicals generation in first few minutes followed by a steep decline in efficiency. Therefore, these particles facilitate and support high charge transfer so that the DMPO spin trap is consumed much more rapidly than in the cases of the steady production materials.

Chapter 4

Conclusions

In the present MSc Thesis, we developed a method for the encapsulation of metal oxides in with carbon shell in a core-shell configuration. The method was optimized for the TiO₂ nanoparticles. The method was based on the insertion of an acetylene gas stream via a ring that upon pyrolysis produced the carbon shell. The produced nanomaterials showed high crystallinity and with rutile favored phases in the cases of the carbon-coated samples. High acetylene flows resulted in thick carbon shells whereas low acetylene flows to “patchy” shells. The acetylene had a dual role during the FSP process, as not only it served as the carbon source for the production of the carbon shell, but also performed *in situ* carbothermal reduction to the carbon-coated particles as a result of the high temperature zone created. Enthalpy feed density calculations validated the above claim as the enthalpy provided to the burner chamber changed drastically upon the addition of the acetylene gas. The initial suggestion was that the carbon-coating process resulted in highly reduced TiO_{2-x} suboxides known as Magnéli phases. The materials were then calcined in carbon-rich CH₄ atmospheres at mild and high temperatures to improve graphitization of the carbon shell.

XRD revealed the crystal structure of the produced nanoparticles, howbeit did not reveal any evidence about the presence of Magnéli phases in the bulk of the materials. The coloration of the particles ranged from white for the TiO₂ oxides, grey for the “patchy” coated TiO_{2-x}@C to almost black for the thick-coated TiO_{2-x}@C. DRS revealed that the thick-coated materials showed no absorbance whereas the “patchy” coated particles showed bandgap narrowing in the above 2 eV range.

Raman spectroscopy prove to be an invaluable tool in the study not only of the carbon-shell but also the surface of the materials. Calcination showed to improve graphitization for the thick-carbon materials whereas for the “patchy” coated led to defective-carbon deposition. Apart for the carbon study, the shift in the titanium rutile peaks suggested the possible presence of Magnéli phase clusters close to the surface.

EPR spectroscopy was the basis of our analysis, complementary to the aforementioned techniques, since is one of the best techniques to study paramagnetic species like Ti³⁺ centers

and oxygen vacancies. The thick carbon-coated materials came out to be non-photoactive, whereas the non-calcined and the mildly calcined “patchy” coated materials were photoactive, as we identified the presence of the Magnéli phase clusters. Preliminary photocatalytic evaluation was done by monitoring the radical generation in spin trapping experiments. This is where the pristine “patchy” coated material excelled, and this is where the Magnéli phase clusters came into effect by boosting the charge transfer for radical generation.

Concluding, this method for encapsulation of nanosemiconductors can be implemented in other reducible metal oxides like ZrO_2 , for surface functionalization of particles for photocatalytic applications.

References

- (1) Jeevanandam, J.; Barhoum, A.; Chan, Y. S.; Dufresne, A.; Danquah, M. K. Review on Nanoparticles and Nanostructured Materials: History, Sources, Toxicity and Regulations. *Beilstein J. Nanotechnol.* **2018**, *9* (1), 1050–1074. <https://doi.org/10.3762/bjnano.9.98>.
- (2) El-Sayed, M. A. Some Interesting Properties of Metals Confined in Time and Nanometer Space of Different Shapes. *Acc. Chem. Res.* **2001**, *34* (4), 257–264. <https://doi.org/10.1021/ar960016n>.
- (3) Ekimov, A. I.; Onushchenko, A. A.; Tsekhomskii, V. A. Exciton Light Absorption by CuCl Microcrystals in Glass Matrix. *Sov. J. Glas. Physics Chem.* **1980**, *6*, 511.
- (4) Soloviev, V. N.; Eichho, A. Molecular Limit of a Bulk Semiconductor: Size Dependence of the “Band Gap” in CdSe Cluster Molecules. *J. Am. Chem. Soc.* **2000**, *122* (11), 2673–2674. <https://doi.org/https://doi.org/10.1021/ja9940367>.
- (5) Brian O’Regan & Michael Grätzel. A Low-Cost, High-Efficiency Solar Cell Based on Dye-Sensitized Colloidal TiO₂ Films. *Nature* **1991**, *354*, 737–740. <https://doi.org/https://doi.org/10.1038/353737a0>.
- (6) Hoffmann, M. R.; Martin, S. T.; Choi, W.; Bahnemann, D. W. Environmental Applications of Semiconductor Photocatalysis. *Chem. Rev.* **1995**, *95* (1), 69–96. <https://doi.org/10.1021/cr00033a004>.
- (7) Linsebigler, A. L.; Lu, G.; Yates, J. T. Photocatalysis on TiO₂ Surfaces: Principles, Mechanisms, and Selected Results. *Chem. Rev.* **1995**, *95* (3), 735–758. <https://doi.org/10.1021/cr00035a013>.
- (8) Teleki, A.; Pratsinis, S. E.; Kalyanasundaram, K.; Gouma, P. I. Sensing of Organic Vapors by Flame-Made TiO₂ Nanoparticles. *Sensors Actuators, B Chem.* **2006**, *119*(2), 683–690. <https://doi.org/10.1016/j.snb.2006.01.027>.
- (9) Wang, R.; Hashimoto, K.; Fujishima, A.; Chikuni, M.; Kojima, E.; Kitamura, A.; Shimohigoshi, M.; Watanabe, T. Light-Induced Amphiphilic Surfaces. *Nature* **1997**, *388* (6641), 431–432. <https://doi.org/10.1038/41233>.
- (10) Lan, Y.; Lu, Y.; Ren, Z. Mini Review on Photocatalysis of Titanium Dioxide Nanoparticles and Their Solar Applications. *Nano Energy* **2013**, *2* (5), 1031–1045. <https://doi.org/10.1016/j.nanoen.2013.04.002>.
- (11) Fahmi, A.; Minot, C.; Silvi, B.; Causá, M. Theoretical Analysis of the Structures of Titanium Dioxide Crystals. *Phys. Rev. B* **1993**, *47* (18), 11717–11724. <https://doi.org/10.1103/PhysRevB.47.11717>.
- (12) Cromer, D. T.; Herrington, K. The Structures of Anatase and Rutile. *J. Am. Chem. Soc.* **1955**, *77*(18), 4708–4709. <https://doi.org/10.1021/ja01623a004>.
- (13) Downs, R. T.; Hall-Wallace, M. The American Mineralogist Crystal Structure Database. *Am. Mineral.* **2003**, *88*, 247–250.

- (14) Barnard, A. S.; Curtiss, L. A. Prediction of TiO₂ Nanoparticle Phase and Shape Transitions Controlled by Surface Chemistry. *Nano Lett.* **2005**, *5* (7), 1261–1266. <https://doi.org/10.1021/nl050355m>.
- (15) Batzill, M.; Morales, E. H.; Diebold, U. Influence of Nitrogen Doping on the Defect Formation and Surface Properties of TiO₂ Rutile and Anatase. *Phys. Rev. Lett.* **2006**, *96* (2), 1–4. <https://doi.org/10.1103/PhysRevLett.96.026103>.
- (16) Diebold, U. The Surface Science of Titanium Dioxide. *Surf. Sci. Rep.* **2003**, *48* (1), 53–229.
- (17) Krishnankutty-Nair, P. K. Growth of Rutile Crystallites during the Initial Stage of Anatase-to-Rutile Transformation in Pure Titania and in Titania-Alumina Nanocomposites. *Scr. Metall. Mater.* **1995**, *33* (5), 849. [https://doi.org/10.1016/0956-716x\(95\)98937-z](https://doi.org/10.1016/0956-716x(95)98937-z).
- (18) Kumar, K. N. P.; Fray, D. J.; Nair, J.; Mizukami, F.; Okubo, T. Enhanced Anatase-to-Rutile Phase Transformation without Exaggerated Particle Growth in Nanostructured Titania-Tin Oxide Composites. *Scr. Mater.* **2007**, *57* (8), 771–774. <https://doi.org/10.1016/j.scriptamat.2007.06.039>.
- (19) Landmann, M.; Rauls, E.; Schmidt, W. G. The Electronic Structure and Optical Response of Rutile, Anatase and Brookite TiO₂. *J. Phys. Condens. Matter* **2012**, *24* (19). <https://doi.org/10.1088/0953-8984/24/19/195503>.
- (20) Leung, D. Y. C.; Fu, X.; Wang, C.; Ni, M.; Leung, M. K. H.; Wang, X.; Fu, X. Hydrogen Production over Titania-Based Photocatalysts. *ChemSusChem* **2010**, *3* (6), 681–694. <https://doi.org/10.1002/cssc.201000014>.
- (21) Reyes-Coronado, D.; Rodríguez-Gattorno, G.; Espinosa-Pesqueira, M. E.; Cab, C.; De Coss, R.; Oskam, G. Phase-Pure TiO₂ Nanoparticles: Anatase, Brookite and Rutile. *Nanotechnology* **2008**, *19* (14). <https://doi.org/10.1088/0957-4484/19/14/145605>.
- (22) Naldoni, A.; Altomare, M.; Zoppellaro, G.; Liu, N.; Kment, Š.; Zbořil, R.; Schmuki, P. Photocatalysis with Reduced TiO₂: From Black TiO₂ to Cocatalyst-Free Hydrogen Production. *ACS Catal.* **2019**, *9* (1), 345–364. <https://doi.org/10.1021/acscatal.8b04068>.
- (23) Bhaviripudi, S.; Mile, E.; Steiner, S. A.; Zare, A. T.; Dresselhaus, M. S.; Belcher, A. M.; Kong, J. CVD Synthesis of Single-Walled Carbon Nanotubes from Gold Nanoparticle Catalysts. *J. Am. Chem. Soc.* **2007**, *129* (6), 1516–1517. <https://doi.org/10.1021/ja0673332>.
- (24) Li, Y.; Zhou, C.; Xie, X.; Shi, G.; Qu, L. Spontaneous, Catalyst-Free Formation of Nitrogen-Doped Graphitic Carbon Nanocages. *Carbon N. Y.* **2010**, *48* (14), 4190–4196. <https://doi.org/10.1016/j.carbon.2010.07.048>.
- (25) Zhang, Y. J.; Liu, X. Y.; Bai, W. Q.; Tang, H.; Shi, S. J.; Wang, X. L.; Gu, C. D.; Tu, J. P. Magnetron Sputtering Amorphous Carbon Coatings on Metallic Lithium: Towards Promising Anodes for Lithium Secondary Batteries. *J. Power Sources* **2014**, *266*, 43–50. <https://doi.org/10.1016/j.jpowsour.2014.04.147>.
- (26) Chaudhuri, R. G.; Paria, S. Core / Shell Nanoparticles : Classes , Properties , Synthesis

- Mechanisms , Characterization , and Applications. *Chem. Rev.* **2012**, *112*(4), 2373–2433. <https://doi.org/10.1021/cr100449n>.
- (27) Charlier, J. C.; Eklund, P. C.; Zhu, J.; Ferrari, A. C. Electron and Phonon Properties of Graphene: Their Relationship with Carbon Nanotubes. *Top. Appl. Phys.* **2008**, *111* (2008), 673–709. https://doi.org/10.1007/978-3-540-72865-8_21.
- (28) Allen, J. M.; Vincent, T. C.; Richard, K. B. Honeycomb Carbon : A Review of Graphene What Is Graphene ? *Chem. Rev.* **2010**, *110*, 132–145.
- (29) Chae, H. K.; Siberio-Pérez, D. Y.; Kim, J.; Go, Y. B.; Eddaoudi, M.; Matzger, A. J.; O’Keeffe, M.; Yaghi, O. M. A Route to High Surface Area, Porosity and Inclusion of Large Molecules in Crystals. *Nature* **2004**, *427* (6974), 523–527. <https://doi.org/10.1038/nature02311>.
- (30) Charlier, J. C.; Gonze, X.; Michenaud, J. P. First-Principles Study of the Stacking Effect on the Electronic Properties of Graphite(S). *Carbon N. Y.* **1994**, *32* (2), 289–299. [https://doi.org/10.1016/0008-6223\(94\)90192-9](https://doi.org/10.1016/0008-6223(94)90192-9).
- (31) Trickey, S. ; Müller-Plathe, F.; Diercksen, G. H. F.; Boettger, J. . Interplanar Binding and Lattice Relaxation in a Graphite Bilayer. *Phys. Rev. B* **1992**, *45* (8), 4460–4468. <https://doi.org/10.1103/PhysRevB.45.4460>.
- (32) Partoens, B.; Peeters, F. M. From Graphene to Graphite: Electronic Structure around the K Point. *Phys. Rev. B* **2006**, *74* (7), 1–11. <https://doi.org/10.1103/PhysRevB.74.075404>.
- (33) Wang, S.; Zhao, L.; Bai, L.; Yan, J.; Jiang, Q.; Lian, J. Enhancing Photocatalytic Activity of Disorder-Engineered C/TiO₂ and TiO₂ Nanoparticles. *J. Mater. Chem. A* **2014**, *2*(20), 7439–7445. <https://doi.org/10.1039/c4ta00354c>.
- (34) Zhang, J.; Vasei, M.; Sang, Y.; Liu, H.; Claverie, J. P. TiO₂@Carbon Photocatalysts: The Effect of Carbon Thickness on Catalysis. *ACS Appl. Mater. Interfaces* **2016**, *8* (3), 1903–1912. <https://doi.org/10.1021/acsami.5b10025>.
- (35) Liu, F.; Feng, N.; Yang, L.; Wang, Q.; Xu, J.; Deng, F. Enhanced Photocatalytic Performance of Carbon-Coated TiO₂- x with Surface-Active Carbon Species. *J. Phys. Chem. C* **2018**, *122* (20), 10948–10955. <https://doi.org/10.1021/acs.jpcc.8b02716>.
- (36) Inagaki, M.; Hirose, Y.; Matsunaga, T.; Tsumura, T.; Toyoda, M. Carbon Coating of Anatase-Type TiO₂ through Their Precipitation in PVA Aqueous Solution. *Carbon N. Y.* **2003**, *41* (13), 2619–2624. [https://doi.org/10.1016/S0008-6223\(03\)00340-3](https://doi.org/10.1016/S0008-6223(03)00340-3).
- (37) Pacchioni, G. Oxygen Vacancy: The Invisible Agent on Oxide Surfaces. *ChemPhysChem* **2003**, *4*(10), 1041–1047. <https://doi.org/10.1002/cphc.200300835>.
- (38) Cho, E.; Han, S.; Ahn, H.-S.; Lee, K.-R.; Kim, S. K.; Hwang, C. S. First-Principles Study of Point Defects in Rutile TiO₂-x.Pdf. *Phys. Rev. B* **2006**, *73* (19). <https://doi.org/10.1103/PhysRevB.73.193202>.
- (39) Walsh, F. C.; Wills, R. G. A. The Continuing Development of Magnéli Phase Titanium Sub-Oxides and Ebonex® Electrodes. *Electrochim. Acta* **2010**, *55* (22), 6342–6351. <https://doi.org/10.1016/j.electacta.2010.05.011>.
- (40) Wierzbicka, E.; Domaschke, M.; Denisov, N.; Fehn, D.; Hwang, I.; Kaufmann, M.;

- Kunstmann, B.; Schmidt, J.; Meyer, K.; Peukert, W.; Schmuki, P. Magnéli Phases Doped with Pt for Photocatalytic Hydrogen Evolution. *ACS Appl. Energy Mater.* **2019**, *2* (12), 8399–8404. <https://doi.org/10.1021/acsaem.9b02053>.
- (41) Ioroi, T.; Akita, T.; Asahi, M.; Yamazaki, S. I.; Siroma, Z.; Fujiwara, N.; Yasuda, K. Platinum-Titanium Alloy Catalysts on a Magnéli-Phase Titanium Oxide Support for Improved Durability in Polymer Electrolyte Fuel Cells. *J. Power Sources* **2013**, *223*, 183–189. <https://doi.org/10.1016/j.jpowsour.2012.09.063>.
- (42) Tao, X.; Wang, J.; Ying, Z.; Cai, Q.; Zheng, G.; Gan, Y.; Huang, H.; Xia, Y.; Liang, C.; Zhang, W.; Cui, Y. Strong Sulfur Binding with Conducting Magnéli-Phase TiO_{2n-1} Nanomaterials for Improving Lithium-Sulfur Batteries. *Nano Lett.* **2014**, *14* (9), 5288–5294. <https://doi.org/10.1021/nl502331f>.
- (43) Padilha, A. C. M.; Raebiger, H.; Rocha, A. R.; Dalpian, G. M. Charge Storage in Oxygen Deficient Phases of TiO_2 : Defect Physics without Defects. *Sci. Rep.* **2016**, *6* (March), 2–8. <https://doi.org/10.1038/srep28871>.
- (44) Jemec Kokalj, A.; Novak, S.; Talaber, I.; Kononenko, V.; Bizjak Mali, L.; Vodovnik, M.; Žegura, B.; Eleršek, T.; Kalčikova, G.; Žgajnar Gotvajn, A.; Kralj, S.; Makovec, D.; Caloudova, H.; Drobne, D. The First Comprehensive Safety Study of Magnéli Phase Titanium Suboxides Reveals No Acute Environmental Hazard. *Environ. Sci. Nano* **2019**, *6* (4), 1131–1139. <https://doi.org/10.1039/c8en01119b>.
- (45) Andersson, S.; Collén, B.; Kuylenstierna, U.; Magnéli, A.; Magnéli, A.; Pestmalis, H.; Åsbrink, S. Phase Analysis Studies on the Titanium-Oxygen System. *Acta Chemica Scandinavica*. 1957, pp 1641–1652. <https://doi.org/10.3891/acta.chem.scand.11-1641>.
- (46) Anderson, J. S.; Hyde, B. G. On the Possible Role of Dislocations in Generating Ordered and Disordered Shear Structures. *J. Phys. Chem. Solids* **1967**, *28* (8), 1393–1408. [https://doi.org/10.1016/0022-3697\(67\)90268-5](https://doi.org/10.1016/0022-3697(67)90268-5).
- (47) Åsbrink, S.; Magnéli, A. Crystal Structure Studies on Trititanium Pentoxide, Ti_3O_5 . *Acta Crystallogr.* **1959**, *12* (8), 575–581. <https://doi.org/10.1107/s0365110x59001694>.
- (48) Szot, K.; Rogala, M.; Speier, W.; Klusek, Z.; Besmehn, A.; Waser, R. TiO_2 -a Prototypical Memristive Material. *Nanotechnology* **2011**, *22* (25), 254001. <https://doi.org/10.1088/0957-4484/22/25/254001>.
- (49) Bartholomew, R. F.; Frankl, D. R. Electrical Properties of Some Titanium Oxides. *Phys. Rev.* **1969**, *187* (3), 828–833. <https://doi.org/10.1103/PhysRev.187.828>.
- (50) Han, W.-Q.; Zhang, Y. Magnéli Phases TiO_{2n-1} Nanowires_ Formation, Optical, and Transport Properties.Pdf. *Appl. Phys. Lett.* **2008**, *92* (20), 203117. <https://doi.org/10.1063/1.2937152>.
- (51) Niu, M.; Tan, H.; Cheng, D.; Sun, Z.; Cao, D. Bandgap Engineering of Magnéli Phase TiO_{2n-1} : Electron-Hole Self-Compensation. *J. Chem. Phys.* **2015**, *143* (5). <https://doi.org/10.1063/1.4928062>.
- (52) Padilha, A. C. M.; Osorio-Guillén, J. M.; Rocha, A. R.; Dalpian, G. M. TiO_{2n-1} Magnéli Phases Studied Using Density Functional Theory. *Phys. Rev. B - Condens. Matter Mater.*

- Phys.* **2014**, *90*(3), 1–7. <https://doi.org/10.1103/PhysRevB.90.035213>.
- (53) Arif, A. F.; Balgis, R.; Ogi, T.; Iskandar, F.; Kinoshita, A.; Nakamura, K.; Okuyama, K. Highly Conductive Nano-Sized Magnéli Phases Titanium Oxide (TiO_x). *Sci. Rep.* **2017**, *7*(1), 1–9. <https://doi.org/10.1038/s41598-017-03509-y>.
- (54) Liborio, L.; Harrison, N. Thermodynamics of Oxygen Defective Magnéli Phases in Rutile: A First-Principles Study. *Phys. Rev. B - Condens. Matter Mater. Phys.* **2008**, *77*(10), 1–10. <https://doi.org/10.1103/PhysRevB.77.104104>.
- (55) Toyoda, M.; Yano, T.; Tryba, B.; Mozia, S.; Tsumura, T.; Inagaki, M. Preparation of Carbon-Coated Magnéli Phases TiO_{2n-1} and Their Photocatalytic Activity under Visible Light.Pdf. *Appl. Catal. B Environ.* **2009**, *88*(1–2), 160–164. <https://doi.org/10.1016/j.apcatb.2008.09.009>.
- (56) Fujishima, A.; Honda, K. Electrochemical Photolysis of Water at a Semiconductor Electrode. *Nature* **1972**, *238*(5358), 37–38. <https://doi.org/10.1038/238038a0>.
- (57) Hurum, D. C.; Agrios, A. G.; Gray, K. A.; Rajh, T.; Thurnauer, M. C. Explaining the Enhanced Photocatalytic Activity of Degussa P25 Mixed-Phase TiO₂ Using EPR. *J. Phys. Chem. B* **2003**, *107*(19), 4545–4549. <https://doi.org/10.1021/jp0273934>.
- (58) Hashimoto, K.; Irie, H.; Fujishima, A. TiO₂ Photocatalysis: A Historical Overview and Future Prospects. *Japanese J. Appl. Physics, Part 1 Regul. Pap. Short Notes Rev. Pap.* **2005**, *44*(12), 8269–8285. <https://doi.org/10.1143/JJAP.44.8269>.
- (59) Subramanian, V.; Wolf, E. E.; Kamat, P. V. Catalysis with TiO₂/Gold Nanocomposites. Effect of Metal Particle Size on the Fermi Level Equilibration. *J. Am. Chem. Soc.* **2004**, *126*(15), 4943–4950. <https://doi.org/10.1021/ja0315199>.
- (60) Qian, R.; Zong, H.; Schneider, J.; Zhou, G.; Zhao, T.; Li, Y.; Yang, J.; Bahnemann, D. W.; Pan, J. H. Charge Carrier Trapping, Recombination and Transfer during TiO₂ Photocatalysis: An Overview. *Catal. Today* **2019**, *335*, 78–90. <https://doi.org/10.1016/j.cattod.2018.10.053>.
- (61) Bhattacharyya, A.; Kawi, S.; Ray, M. B. Photocatalytic Degradation of Orange II by TiO₂ Catalysts Supported on Adsorbents. *Catal. Today* **2004**, *98*(3), 431–439. <https://doi.org/10.1016/j.cattod.2004.08.010>.
- (62) Domaschke, M.; Zhou, X.; Wergen, L.; Romeis, S.; Miehlich, M. E.; Meyer, K.; Peukert, W.; Schmuki, P. Schmuki-Magnéli-Phases in Anatase Strongly Promote Cocatalyst-Free Photocatalytic Hydrogen Production.Pdf. *ACS Catal.* **2019**, *9*(4), 3627–3632. <https://doi.org/10.1021/acscatal.9b00578>.
- (63) Shanmugam, S.; Gabashvili, A.; Jacob, D. S.; Yu, J. C.; Gedanken, A. Synthesis and Characterization of TiO₂@C Core-Shell Composite Nanoparticles and Evaluation of Their Photocatalytic Activities.Pdf. *Chem. Mater.* **2006**, *18*(9), 2275–2282. <https://doi.org/10.1021/cm052790n>.
- (64) Nikam, A. V.; Prasad, B. L. V.; Kulkarni, A. A. Wet Chemical Synthesis of Metal Oxide Nanoparticles: A Review. *CrystEngComm* **2018**, *20*(35), 5091–5107. <https://doi.org/10.1039/C8CE00487K>.

- (65) Ulrich, G. D. Theory of Particle Formation and Growth in Oxide Synthesis Flames. *Combust. Sci. Technol.* **1971**, *4*, 47–57. <https://doi.org/10.1080/00102207108952471>.
- (66) Pratsinis, E. Flame Aerosol Synthesis of Ceramic Powders. *Fuel Energy Abstr.* **1998**, *39* (5), 384. [https://doi.org/10.1016/s0140-6701\(98\)94112-1](https://doi.org/10.1016/s0140-6701(98)94112-1).
- (67) Teoh, W. Y.; Amal, R.; Mädler, L. Flame Spray Pyrolysis: An Enabling Technology for Nanoparticles Design and Fabrication. *Nanoscale* **2010**, *2* (8), 1324–1347. <https://doi.org/10.1039/c0nr00017e>.
- (68) Mädler, L.; Kammler, H. K.; Mueller, R.; Pratsinis, S. E. Controlled Synthesis of Nanostructured Particles by Flame Spray Pyrolysis. *Journal of Aerosol Science*. 2002, pp 369–389. [https://doi.org/10.1016/S0021-8502\(01\)00159-8](https://doi.org/10.1016/S0021-8502(01)00159-8).
- (69) Pratsinis, S. E. Aerosol-based Technologies in Nanoscale Manufacturing_ from Functional Materials to Devices through Core Chemical Engineering.Pdf. *AIChE J.* **2010**, *56* (12), 3028–3035. <https://doi.org/10.1002/aic.12478>.
- (70) Koirala, R.; Pratsinis, S. E.; Baiker, A. Synthesis of Catalytic Materials in Flames: Opportunities and Challenges. *Chem. Soc. Rev.* **2016**, *45* (11), 3053–3068. <https://doi.org/10.1039/c5cs00011d>.
- (71) Teleki, A.; Heine, M. C.; Krumeich, F.; Akhtar, M. K.; Pratsinis, S. E. In Situ Coating of Flame-Made TiO₂ Particles with Nanothin SiO₂ Films. *Langmuir* **2008**, *24* (21), 12553–12558. <https://doi.org/10.1021/la801630z>.
- (72) Athanassiou, E. K.; Mensing, C.; Stark, W. J. Insulator Coated Metal Nanoparticles with a Core / Shell Geometry Exhibit a Temperature Sensitivity Similar to Advanced Spinel. *Sensors Actuators, A Phys.* **2007**, *138* (1), 120–129. <https://doi.org/10.1016/j.sna.2007.04.005>.
- (73) Bunaciu, A. A.; Udriștioiu, E. gabriela; Aboul-Enein, H. Y. X-Ray Diffraction: Instrumentation and Applications. *Crit. Rev. Anal. Chem.* **2015**, *45* (4), 289–299. <https://doi.org/10.1080/10408347.2014.949616>.
- (74) Zsigmondy, R. Kolloidchemie Ein Lehrbuch. In *Kolloidchemie Ein Lehrbuch*; Springer, Berlin, Heidelberg, 1912; pp 387–409. <https://doi.org/10.1007/978-3-662-33915-2>.
- (75) Raman, C. V.; Krishnan, K. S. A New Type of Secondary Radiation [11]. *Nature* **1928**, *121* (3048), 501–502. <https://doi.org/10.1038/121501c0>.
- (76) Smith, E.; Dent, G. *Modern Raman Spectroscopy - A Practical Approach*; 2005. <https://doi.org/10.1002/0470011831>.
- (77) Colomban, P.; Gouadec, G. Raman Scattering Theory and Elements of Raman Instrumentation. *Raman Spectrosc. Soft Matter Appl.* **2008**, 11–29. <https://doi.org/10.1002/9780470475997.ch2>.
- (78) Mirabella, F. M. *Modern Techniques in Applied Molecular Spectroscopy*; John Wiley & Sons, 1998.
- (79) Bock, S.; Kijatkin, C.; Berben, D.; Imlau, M. Absorption and Remission Characterization of Pure, Dielectric (Nano-)Powders Using Diffuse Reflectance Spectroscopy: An End-to-End Instruction. *Appl. Sci.* **2019**, *9* (22). <https://doi.org/10.3390/APP9224933>.

- (80) Tauc, J.; Grigorovici, R.; Vancu, A. Optical Properties and Electronic Structure of Amorphous Germanium. *Phys. Status Solidi* **1966**, *15*, 627. <https://doi.org/10.1002/pssb.19660150224>.
- (81) Makuła, P.; Pacia, M.; Macyk, W. How To Correctly Determine the Band Gap Energy of Modified Semiconductor Photocatalysts Based on UV-Vis Spectra. *J. Phys. Chem. Lett.* **2018**, *9*(23), 6814–6817. <https://doi.org/10.1021/acs.jpcclett.8b02892>.
- (82) Giamello, E.; Brustolon, M. *Electron Paramagnetic Resonance: A Practitioner's Toolkit*; John Wiley & Sons, 2009.
- (83) Zeeman, P. The Effect of Magnetisation on the Nature of Light Emitted by a Substance. *Nature*. 1897, p 347. <https://doi.org/10.1038/055347a0>.
- (84) Eaton, G. R.; Eaton, S. S.; Barr, D. P.; Weber, R. T. *Quantitative EPR*; Springer Wien New York, 2010. <https://doi.org/10.1007/978-3-211-92948-3>.
- (85) Duin, E. *Electron Paramagnetic Resonance Theory*. 2013.
- (86) Rowlands, C. C.; Murphy, D. M. Chemical Reactions of EPR. In *Encyclopedia of Spectroscopy and Spectrometry*; 2016; Vol. 1, pp 221–223.
- (87) Einstein, A. Über Einen Die Erzeugung Und Verwandlung Des Lichtes Betreffenden Heuristischen Gesichtspunkt. *Ann. Phys.* **1905**, *322* (6), 132–148. <https://doi.org/10.1002/andp.19053220607>.
- (88) Nordling, C.; Sokolowski, E.; Siegbahn, K. A. I. Precision Method for Obtaining Absolute Values of Atomic Binding Energies. *Phys. Rev.* **1957**, *105* (5), 1676.
- (89) Brunauer, S.; Emmett, P. H.; Teller, E. Adsorption of Gases in Multimolecular Layers. *J. Am. Chem. Soc.* **1938**, *60* (2), 309–319. <https://doi.org/10.1021/ja01269a023>.
- (90) Lowell, S.; Shields, J. E.; Thomas, M. A.; Thommes, M. *Characterization of Porous Solids and Powders: Surface Area, Pore Size and Density*, 1st ed.; Kluwer Academic Publishers, 2004.
- (91) Sing, K. S. W.; Everett, D. H.; Haul, R. A. W.; Moscou, L.; Pierotti, R. A.; Rouquerol, J.; Siemieniewska, T. Reporting Physisorption Data for Gas/Solid Systems with Special Reference to the Determination of Surface Area and Porosity. *Pure Appl. Chem.* **1985**, *57* (4), 603–619. <https://doi.org/10.1351/pac198557040603>.
- (92) Mueller, R.; Mädler, L.; Pratsinis, S. E. Nanoparticle Synthesis at High Production Rates by Flame Spray Pyrolysis. *Chemical Engineering Science*. 2003, pp 1969–1976. [https://doi.org/10.1016/S0009-2509\(03\)00022-8](https://doi.org/10.1016/S0009-2509(03)00022-8).
- (93) Ashgriz, N. *Handbook of Atomization and Sprays*; Springer US, 2011.
- (94) Jossen, R.; Pratsinis, S. E.; Stark, W. J.; Mädler, L. Criteria for Flame-Spray Synthesis of Hollow, Shell-like, or Inhomogeneous Oxides. *Journal of the American Ceramic Society*. 2005, pp 1388–1393. <https://doi.org/10.1111/j.1551-2916.2005.00249.x>.
- (95) Buesser, B.; Gröhn, A. J. Multiscale Aspects of Modeling Gas-Phase Nanoparticle Synthesis. *Chem. Eng. Technol.* **2012**, *35* (7), 1133–1143. <https://doi.org/10.1002/ceat.201100723>.
- (96) Athanassiou, E. K.; Grass, R. N.; Stark, W. J. Chemical Aerosol Engineering as a Novel

- Tool for Material Science: From Oxides to Salt and Metal Nanoparticles. *Aerosol Sci. Technol.* **2010**, *44* (2), 161–172. <https://doi.org/10.1080/02786820903449665>.
- (97) Grass, R. N.; Stark, W. J. Gas Phase Synthesis of Fcc-Cobalt Nanoparticles. *J. Mater. Chem.* **2006**, *16* (19), 1825–1830. <https://doi.org/10.1039/b601013j>.
- (98) Grass, R. N.; Stark, W. J.; Athanassiou, E. K. Reducing Flame Spray Pyrolysis Method for the Production of Metal, Non-Oxidic, Ceramic and Reduced Metal Oxide Powders and Nano-Powders, 2007.
- (99) Teleki, A.; Pratsinis, S. E.; Wegner, K.; Jossen, R.; Krumeich, F. Flame-Coating of Titania Particles with Silica. *J. Mater. Res.* **2005**, *20* (5), 1336–1347. <https://doi.org/10.1557/JMR.2005.0160>.
- (100) Teleki, A.; Buesser, B.; Heine, M. C.; Krumeich, F.; Akhtar, M. K.; Pratsinis, S. E. Role of Gas - Aerosol Mixing during in Situ Coating of Flame-Made Titania Particles. *Industrial and Engineering Chemistry Research*. 2009, pp 85–92. <https://doi.org/10.1021/ie800226d>.
- (101) Spyrogianni, A.; Herrmann, I. K.; Keevend, K.; Pratsinis, S. E.; Wegner, K. The Silanol Content and in Vitro Cytolytic Activity of Flame-Made Silica. *J. Colloid Interface Sci.* **2017**, *507*, 95–106. <https://doi.org/10.1016/j.jcis.2017.07.096>.
- (102) Chen, X.; Liu, L.; Liu, Z.; Marcus, M. A.; Wang, W. C.; Oyler, N. A.; Grass, M. E.; Mao, B.; Glans, P. A.; Yu, P. Y.; Guo, J.; Mao, S. S. Properties of Disorder-Engineered Black Titanium Dioxide Nanoparticles through Hydrogenation. *Sci. Rep.* **2013**, *3*, 1–7. <https://doi.org/10.1038/srep01510>.
- (103) Ookubo, A.; Kanezaki, E.; Ooi, K. ESR, XRD, and DRS Studies of Paramagnetic Ti³⁺ Ions in a Colloidal Solid of Titanium Oxide Prepared by Hydrolysis of TiCl₃. *Langmuir* **1990**, *6* (1), 206–209. <https://doi.org/10.1021/la00091a033>.
- (104) Balachandran, U.; Erer, N. G. Raman Spectra of Titanium Dioxide. *J. Solid State Chem.* **1982**, *42* (3), 276–282. [https://doi.org/10.1016/0022-4596\(82\)90006-8](https://doi.org/10.1016/0022-4596(82)90006-8).
- (105) Ferrari, A. C.; Robertson, J. Interpretation of Raman Spectra of Disordered and Amorphous Carbon. *Phys. Rev. B* **2000**, *61* (20), 14095. <https://doi.org/10.1103/PHYSREVB.61.14095>.
- (106) Schmid, J.; Grob, B.; Niessner, R.; Ivleva, N. P. Multiwavelength Raman Microspectroscopy for Rapid Prediction. *Anal. Chem. Lett.* **2011**, 1173–1179.
- (107) Commodo, M.; Joo, P. H.; De Falco, G.; Minutolo, P.; D'Anna, A.; Gülder, Ö. L. Raman Spectroscopy of Soot Sampled in High-Pressure Diffusion Flames. *Energy and Fuels* **2017**, *31* (9), 10158–10164. <https://doi.org/10.1021/acs.energyfuels.7b01674>.
- (108) Wang, F.; Shi, R.; Lei, Y.; Lei, Z.; Jiang, R.; Wang, D.; Liu, Z.; Sun, J. Formation Mechanisms of Interfaces between Different TinO_{2n-1}phases Prepared By carbothermal Reduction Reaction. *CrystEngComm* **2019**, *21* (3), 524–534. <https://doi.org/10.1039/C8CE01459K>.
- (109) Athanassiou, E. K.; Grass, R. N.; Stark, W. J. Large-Scale Production of Carbon-Coated Copper Nanoparticles for Sensor Applications. *Nanotechnology* **2006**, *17* (6), 1668–1673.

- <https://doi.org/10.1088/0957-4484/17/6/022>.
- (110) Polliotto, V.; Livraghi, S.; Giamello, E. Electron Magnetic Resonance as a Tool to Monitor Charge Separation and Reactivity in Photocatalytic Materials. *Res. Chem. Intermed.* **2018**, *44* (7), 3905–3921. <https://doi.org/10.1007/s11164-018-3467-0>.
- (111) Nakaoka, Y.; Nosaka, Y. ESR Investigation into the Effects of Heat Treatment and Crystal Structure on Radicals Produced over Irradiated TiO₂ Powder. *J. Photochem. Photobiol. A Chem.* **1997**, *110* (3), 299–305. [https://doi.org/10.1016/S1010-6030\(97\)00208-6](https://doi.org/10.1016/S1010-6030(97)00208-6).
- (112) Hurum, D. C.; Gray, K. A.; Rajh, T.; Thurnauer, M. C. Recombination Pathways in the Degussa P25 Formulation of TiO₂: Surface versus Lattice Mechanisms. *J. Phys. Chem. B* **2005**, *109* (2), 977–980. <https://doi.org/10.1021/jp045395d>.
- (113) Berger, T.; Sterrer, M.; Diwald, O.; Knözinger, E.; Panayotov, D.; Thompson, T. L.; Yates, J. T. Light-Induced Charge Separation in Anatase TiO₂ Particles. *J. Phys. Chem. B* **2005**, *109* (13), 6061–6068. <https://doi.org/10.1021/jp0404293>.
- (114) Houlihan, J. F.; Mulay, L. N. Characterization of and Electronic Structural Studies on the Oxides of Titanium: E. P. R. Linewidths. *Mater. Res. Bull.* **1971**, *6* (8), 737–742. [https://doi.org/10.1016/0025-5408\(71\)90107-3](https://doi.org/10.1016/0025-5408(71)90107-3).
- (115) Dvoranová, D.; Barbieriková, Z.; Brezová, V. Radical Intermediates in Photoinduced Reactions on TiO₂ (An EPR Spin Trapping Study). *Molecules* **2014**, *19* (11), 17279–17304. <https://doi.org/10.3390/molecules191117279>.